DISS. ETH NO. 23326

LIGHT UP THE TRAIL TO PLANETS

DUST IN PROTOPLANETARY DISKS
TRACED BY SCATTERED LIGHT

A thesis submitted to attain the degree of

DOCTOR OF SCIENCES of ETH ZURICH

(Dr. sc. ETH Zurich)

presented by

Antonio Garufi

MSc Astrophysics and Cosmology
Alma Mater Studiorum, Bologna (Italy)

born on February 6th, 1986

citizen of Italy

accepted on the recommendation of

Prof. Dr. Hans Martin Schmid, examiner
Prof. Dr. Michael R. Meyer, co-examiner
Dr. Leonardo Testi, co-examiner

Zurich, 2016

Abstract

Since the dawn of humanity, other planets beckon. Over 2000 planets orbiting stars other than our Sun have been discovered since the late twentieth century. The rich and complex architecture of these exoplanets fosters our desire to understand how planets form. This work is devoted to a study of the physical conditions of the birthplaces of planets.

Protoplanetary disks can be considered as a by-product of the star formation, which occurs from the collapse of a molecular cloud in the interstellar space. During the collapse, the increased rotation of the infalling core prevents some material at the equator from further collapsing. This process results in a disk of dust and gas which orbits the newly born star for approximately 10 Myr. Planets are believed to form in these disks via coagulation of dust grains. However, this process is not trivial as both numerical simulations and laboratory experiments reveal the existence of a *meter barrier*, over which solids cannot grow further because of both rapid migration toward the central star and fragmenting collisions. This motivates the search for special sights in protoplanetary disks where the barrier is overcome and planet formation is favored.

Direct imaging is the best investigation tool for most astronomical objects. However, protoplanetary disks are very small (a few hundreds of times the Earth-Sun distance at most). This requires observations with angular resolution much smaller than $1''$. At millimeter and radio wavelengths this is achievable only by interferometers and led to the construction of the ambitious Atacama Large Millimeter Array (ALMA), located on the Chajnantor plateau in Chile. Conversely, a very good angular resolution is a natural advantage of observations at optical and near-IR wavelengths. However, at these short wavelengths the stellar emission dominates over that of the disk. To alleviate this limit, many observational techniques have been implemented. Much of the current focus is on *Polarimetric Differential Imaging* (PDI), a technique exploiting the fact that the stellar light is mainly unpolarized, contrary to the scattered light from the disk. This type of observations traces μm-sized dust grains at the disk surface and is thus complementary to images at millimeter wavelengths, which probe mm-sized grains closer to the disk midplane. This thesis studies PDI images of protoplanetary disks and aims to contribute to the understanding of the distribution of small dust particles in protoplanetary disks. The comparison with larger particles and an improved view of the architecture of disks provide new insight into both the morphology and the evolution of these intriguing objects.

A fraction of protoplanetary disks shows a large central cavity, which can be ascribed to the interaction with (forming) planets. These objects are called *transition disks*, and their cavities are the subject of Chapter 2. We analyze the exquisite near-IR PDI data of a most known transition disk, around SAO 206462, obtained with the NACO instrument at the Very Large Telescope (VLT), at Cerro Paranal in Chile. These observations reveal a prominent double-spiral structure and a central cavity, which is significantly smaller than what was inferred at millimeter wavelengths. We explain this discrepancy with the different dynamics of μm- and mm-sized dust particles at the disk inner edge, in a scenario where the cavity is induced by a (yet unseen) giant planet. It is still unclear whether the observed spirals are intrinsic changes of the dust density present down to the disk midplane or only disk surface wiggles. ALMA images with an angular resolution comparable to our PDI data will enable to disentangle this and therefore to draw conclusions on the origin of these spirals.

PDI observations do not always reveal a bright disk in scattered light. However, also non-detections provide important information on the disk geometry. Understanding what geometrical or physical factors can prevent us from detecting scattered light from disks is the main scope of Chapter 3. We show VLT/NACO observations of three elusive disks and conclude that their *flatness* is the most probable reason for the absence of scattered light. This led us to obtain new VLT/NACO images of disks which are known to be flat. Also this second survey led to (mostly) non-detections leaving an aura of mystery around these objects. Nevertheless, these non-detections allowed us to put important upper limits on the disk brightness, so as to optimize the upcoming observations of flat disks with the new-generation instrument VLT/SPHERE (Spectro-Polarimetric High-contrast Exoplanet REsearch).

In Chapter 3 we also discuss the peculiar morphology of the faint disk around HD163296. The ring-like structure detected in PDI is, at first glance, incompatible with the millimeter observations, which reveal a bright continuous disk. We propose that the ring seen in scattered light is due to a local enhancement of the disk scale height. Speculatively, this may be connected to the physics at the CO *ice-line*, which is the disk region where the temperature drops below the freeze-out temperature of CO. Ice-lines are extensively studied because planet formation therein is potentially favored.

New opportunities to image elusive disk features are provided by instruments like VLT/SPHERE and GPI, which are assisted by new-generation adaptive optics systems to correct for the atmospheric aberrations. In Chapter 4 we analyzed the first SPHERE observations of HD100546, whose remarkable disk hosts two planet candidates. Any signposts of planet-disk interaction remain fairly elusive and this raises further questions

on the mechanisms of planet formation. Nevertheless, the data reveal new intriguing forms of disk structures and are a showcase of the SPHERE's capabilities.

ALMA, GPI, and VLT/SPHERE, in the near future, as well as the James Webb Space Telescope and the European Extremely Large Telescope, a bit further on, guarantee for all exoplanetary scientists exciting times ahead.

Sommario

Sin dall'alba dell'umanità altri pianeti ci chiamano. Oltre 2000 pianeti orbitanti attorno ad altre stelle sono stati scoperti sin dalla fine del ventesimo secolo. La ricca e complessa architettura di questi esopianeti alimenta il nostro desiderio di capire come si formano i pianeti. Questo lavoro è dedicato allo studio delle condizioni fisiche dei luoghi di nascita dei pianeti.

I *dischi protoplanetari* possono essere considerati come un prodotto secondario della formazione di una stella, che avviene attraverso il collasso di una nube molecolare nello spazio interstellare. Durante il collasso la crescente rotazione del nucleo in collasso impedisce al materiale all'equatore di collassare ulteriormente. Questo processo risulta in un disco di gas e polvere che orbita la neonata stella per circa 10 milioni di anni. Si ritiene che i pianeti si formino in questi dischi per coagulazione di grani di polvere. Tuttavia questo processo non è semplice considerato che sia simulazioni numeriche che esperimenti di laboratorio rivelano l'esistenza di una *barriera del metro*, oltre la quale i solidi non crescono ulteriormente a causa della loro rapida migrazione verso la stella o perché frammentati nelle collisioni. Questo motiva la ricerca di speciali luoghi in dischi protoplanetari dove questa barriera può essere superata e la formazione di pianeti è agevolata.

L'imaging diretto è il miglior metodo di investigazione per la maggior parte degli oggetti astronomici. Tuttavia i dischi protoplanetari sono molto piccoli (qualche centinaia di volte la distanza Terra-Sole al più). Ciò richiede osservazioni con risoluzione angolare molto minore di $1''$. A lunghezze d'onda radio o millimetriche questo è possibile solo per interferometri e ha condotto alla costruzione dell'ambizioso Atacama Large Millimeter Array (ALMA), situato sull'altopiano Chajanantor in Cile. D'altro lato un'ottima risoluzione angolare è un naturale vantaggio di osservazioni a lunghezze d'onda ottiche e vicino-infrarosse. Tuttavia a queste corte lunghezze d'onda l'emissione stellare domina su quella del disco. Numerose tecniche osservative sono state sviluppate per attenuare questo limite. Grossa attenzione è attualmente sull'*Imaging Polarimetrico Differenziale*

(PDI), una tecnica che sfrutta il fatto che la luce stellare è fondamentalmente non polarizzata, al contrario della luce riflessa dal disco. Questo tipo di osservazioni traccia i granelli di polvere delle dimensioni del μm e sono quindi complementari alle immagini a lunghezze d'onda millimetriche, che sono invece sensibili a grani delle dimensioni del mm vicino al piano del disco. Questa tesi studia immagini in PDI di dischi protoplanetari e si prefigge di contribuire alla comprensione della distribuzione dei piccoli granelli di polvere nei dischi protoplanetari.

Alcuni dischi protoplanetari mostrano una larga cavità che può essere attribuita all'interazione con pianeti (in formazione). Questi oggetti sono detti *dischi in transizione* e le loro cavità sono il soggetto di studio del Capitolo 2. Analizziamo gli splendidi dati infrarosso in PDI di un disco in transizione molto conosciuto, attorno a SAO 206462, ottenuti con lo strumento NACO del Very Large Telescope (VLT), situato sul Cerro Paranal in Cile. Queste osservazioni rivelano una evidente struttura a doppia spirale e una cavità centrale che è significativamente più piccola di quanto visto a lunghezze d'onda millimetriche. Attribuiamo questa discrepanza alla diversa dinamica di grani micrometrici e millimetrici al bordo interno del disco, in uno scenario dove la cavità è indotta da un pianeta gigante (ancora non visto). Non è ancora chiaro se le spirali osservate siano cambiamenti intrinseci alla densità della polvere presenti fin giù nel piano del disco o solo piccole increspature alla superficie del disco stesso. Immagini ALMA con risoluzione angolare paragonabile ai nostri dati PDI ci consentiranno di distinguere tra i due scenari e di conseguenza di trarre conclusioni sull'origine di queste spirali.

Non sempre le osservazioni in PDI rivelano un brillante disco in luce riflessa. Tuttavia anche l'assenza di segnale può fornire informazioni importanti sulla geometria del disco. Comprendere quali fattori geometrici e fisici possono impedire la rivelazione di luce riflessa è lo scopo principale del Capitolo 3. Mostriamo osservazioni VLT/NACO di tre dischi elusivi e concludiamo che la loro *piattezza* è la ragione più probabile per l'assenza di luce riflessa. Questo ci ha spinto a ottenere nuove immagini VLT/NACO di dischi ritenuti essere piatti. Anche questo secondo campione è risultato (per lo più) in assenza di segnale lasciando un velo di mistero attorno a questi oggetti. Ciononostante queste osservazioni ci hanno consentito di porre importanti limiti superiori alla brillanza dei dischi, così da poter ottimizzare nuove osservazioni di dischi piatti con lo strumento di nuova generazione VLT/SPHERE (Spectro-Polarimetric High-contrast Exoplanet REsearch).

Nel capitolo 3 discutiamo anche la peculiare morfologia del disco attorno a HD163296. La struttura ad anello rivelata in PDI è a prima vista incompatibile con osservazioni millimetriche, che tracciano un brillante e continuo disco. Proponiamo che la struttura ad anello visibile in luce riflessa sia dovuta ad un aumento locale dell'altezza del disco. Questo può essere speculativamente connesso alla fisica alla *linea del ghiacco* del CO, che è la regione del disco dove la temperatura scende sotto la temperatura di congelamento del CO. Le linee del ghiaccio sono studiate con interesse poiché la formazione di pianeti è localmente potenzialmente favorita.

Nuove opportunità di visualizzare elusive caratteristiche dei dischi sono fornite da strumenti come VLT/SPHERE e GPI, che sono assistiti da ottiche adattive di nuove generazione per la correzione di aberrazioni atmosferiche. Nel Capitolo 4 analizziamo le prime osservazioni SPHERE di HD100546, il cui caratteristico disco ospita due candidati planetari. Qualsiasi traccia di interazione disco-pianeta rimane piuttosto elusiva e ciò fa sorgere ulteriori domande sui meccanismi di formazione planetaria. Ciononostante questi dati rivelano nuove intriganti tipologie di struttura del disco e mostrano chiaramente le potenzialità di SPHERE.

ALMA, GPI e VLT/SPHERE nell'immediato futuro e il James Webb Space Telescope e lo European Extremely Large Telescope più avanti garantiranno un emozionante periodo per tutti gli scienziati esoplanetari.

Contents

List of Figures

List of Tables

Preface

Now more than ever, I feel that my last years have been a long long walk. The metaphor describing our social, artistic, or technological progress as a trail is very old. I have always particularly liked a quote by the argentinian film maker Fernando Birri, which was often cited by his good friend Eduardo Galeano. In the barbaric effort to translate from Spanish to English, this may sound as:

> *"Utopia is on the horizon.*
> *I move two steps closer, it moves two steps further.*
> *I move ten steps and the horizon runs ten steps further away.*
> *As much as I may walk, I'll never reach it.*
> *So what's the point of utopia?*
> *The point is this, to keep walking."*
>
> FERNANDO BIRRI

Without bringing up life itself, we can certainly say that the scientific research is well described by this quote, and especially the astronomical research. There are no finishing lines in astronomy, there is no need for the study of the Universe, if not for our desire to know more about it. The more researches learn, the more they will have to understand. The more we move forward, the more we must walk to reach the horizon. I brought this notion with me during the entire PhD.

This thesis is the tip of the iceberg representing my experience as a PhD student in the *Star and Planet Formation* group at ETH. When I joined the group in 2012, I had just obtained my M.Sc. degree from the University of Bologna. I had spent most of 2011 at the Kapteyn Institute in Groningen to write the master thesis. This effort was my first experience as a researcher, and had fostered my desire to start a PhD.

At the beginning of the PhD, the only certainty of my research plan was my wish to work on observations of protoplanetary disks, since the master thesis had strongly triggered my interest in these objects. I was lucky enough to join soon a project by a sub-group of colleagues working on a small survey of protoplanetary disks. I devoted my energy in the first year to learn the nature of those observations and to write a paper on one of those objects. This work was published in the fall of 2013, while the group finalized two other papers from the same successful survey.

During the first year, I could also work on a side project regarding the observations and models of the master thesis. This effort led to a publication in 2014, which is not fully presented in this thesis but it is sometimes mentioned in the Introduction. This project also allowed me to attend my first important conference in March 2012, the *"From atoms to pebbles: Herschel's view of star and planet formation"* in Grenoble, where I had a taste of the extent of our field.

In late 2013, I started to work on three other objects, which were left from the 2012 survey. This is the work I am most attached to. The path to the publication was fairly short (less than one year), but the results of this work led me to a branch of investigation which is still very active. A successful observing proposal was written in late 2014. These observations were taken in summer 2015 and will constitute my first project after the PhD.

2014 was also the year zero of the SPHERE instrument. As ETH is part of the SPHERE consortium, I could join the SPHERE Disk group and start planning the upcoming guaranteed observations. During the second half of the year, I spent much time reducing the first data and learning about the tools to analyze them. This was also a fruitful period to meet external colleagues and advertise my work. The IAU Symposium in Victoria, the *Planet formation & evolution* in Kiel, and the Gordon Research Conference in Mount Holyoke are the conferences, among many, that I enjoyed (and where I learned) the most.

Finally, in 2015 I had the chance to go observing with SPHERE. In May 2015 I went to Cerro Paranal and participate in one of the first guaranteed observing runs. I took the lead of one of the deriving projects, which constitutes the third main part of this thesis. The paper resulting from this project was published at the beginning of 2016. Moreover, at the end of 2015 I could return to Paranal to carry out a new SPHERE observing run, where we obtained superb observations that will be analyzed by the consortium in 2016.

Putting together all pieces in this thesis has been the last effort of my PhD. The three main chapters of this thesis (from Chapter 2 to 4) are based on the three first-author papers from 2013, 2014, and 2016 written with colleagues at ETH (the first two) and with the SPHERE Disk group (the third). An introduction to the field is presented in Chapter 1. Many inspiring reviews helped me write this introduction, and in particular those by Dullemond & Monnier (2010), Williams & Cieza (2011), Espaillat et al. (2014), Helled et al. (2014), Raymond et al. (2014), Testi et al. (2014), Andrews (2015), and Armitage (2015). In Chapter 5 I draw my (evolving) conclusions based on both the results of the individual papers and the experience gained within the local group at ETH and the Disk group of the SPHERE consortium.

27 January 2016,
Antonio Garufi

Cleopatra: If it be love indeed, tell me how much
Mark Antony: There's beggary in the love that can be reckon'd
Cleopatra: I'll set a bourn how far to be beloved
Mark Antony: Then must thou needs find out new heaven, new earth.

WILLIAM SHAKESPEARE, *"Antony and Cleopatra", 1607*

1

Introduction

William Shakespeare is only one of millions of poets, philosophers, and lovers who have thought of other planets as unattainable existences where our prospects and ideas can be overturned. We have always strived to find these alternative existences, and the quest drove us to explore equally the Near and the Far, our Soul and our Universe. This parallelism may have to do with the fact that our Universe, and all other worlds, stars and celestial bodies, albeit out of reach, are under our nose every day (oh, well above our nose every night). This is the peculiarity that distinguishes astronomy from all other sciences. The Universe can be seen, studied, admired, contemplated, but it cannot be reached. "*As for me, I am tormented with an everlasting itch for things remote. I love to sail forbidden seas...*" (HERMAN MELVILLE, *Moby-Dick*). Hundreds of generations have perceived, when looking at a night sky, that other earths, orbiting those billions of stars, must be there. One generation could even see these worlds, and study, admire, contemplate them. Yet nobody could reach these worlds, nobody could sail these forbidden seas.

The scientific study of other planets than the Earth begun in ancient times. All civilizations knew that five of the thousands of stars visible in the sky move in relation to all others. These *wandering stars* have always been the most known and studied celestial objects, together with our Sun and our Moon. However, Mercury, Venus, Mars, Jupiter, and Saturn remained the only known planets for millennia, until long after the invention of the telescope in the 17th century. The discovery of Uranus (1781) and Neptune (1846) and the increasing sway gained by the Heliocentrism were the most tangible steps toward our current notion of the Solar system. The Scientific Revolution also brought the idea that stars and planets are not eternal and that they must be born at a certain time. In 1755, Immanuel Kant published his Solar Nebular Hypothesis where he argued that stars and planets form from the gradual collapse of a slowly rotating gaseous nebula.

Despite the great astronomical progress of the 1900s, the Solar System remained the unique sample of known planets until the end of the century. In October 1995, Michel Mayor and Didier Queloz announced the first detection of an exoplanet orbiting a main-sequence star (51 Pegasi). Technological advances in high-resolution spectroscopy and high-precision photometry led to the rapid detection of many new exoplanets. In particular, the Kepler Space Telescope, launched by NASA in 2009, boosted the recovery of transiting exoplanets by observing small variations in the brightness phase curve of 145,000 stars. As the number of detections increased, it was clear that the exoplanetary architecture does not resemble that of the Solar System. Particularly surprising was the discovery of a large number of hot Jupiters (giant planets orbiting very close to the Star) and super-Earths (rocky planets up to 10 times more massive than the Earth). These discoveries brought our paradigm of planet formation (until 1995 exclusively based on the Solar System) into question. As of 16 January 2016, 2047 exoplanets have been confirmed (http://exoplanet.eu/).

1.1 Star and planet formation

The formation of planets is related to the formation of the hosting star. The first step in the creation of stars and planetary systems is the gravitational collapse of a molecular cloud. These clouds are parsec-scaled over-density of (mainly) molecular hydrogen that are commonly observed in the interstellar medium (ISM). When the gravitational forces start to dominate over the internal pressure, the collapse of the cloud begins. This requires the cloud mass to exceed the so-called Jeans mass, which is expressed through temperature T and density ρ as $M_\mathrm{J} \propto T^{3/2}\rho^{-1/2}$ (Shu et al., 1987). More compact structures fragment throughout the cloud collapse, until a dense core of roughly 0.1 pc of size becomes gravitationally unstable and rapidly collapse, so as to initiate the protostar stage (referred to as Class 0). During this phase, the initial rotation of the core increases because of the angular momentum conservation. The enhanced rotation prevents infall at the equator and, thus, the envelope flattens so as to make the protostar visible along the rotation axis and to eventually become a disk (Class I stage, $\sim 10^5$ years after the onset of the collapse). The collapsing material accretes on the newly born disk. Then, within the disk, angular momentum is transported via shear viscosity from the inner regions outward enabling mass accretion from the inner disk onto the central protostar.

The mass of the forming star is a crucial parameter influencing both the star and disk evolution. Low-mass stars, i.e. stars with $M < 1.5\,\mathrm{M}_\odot$, are called T Tauri stars (TTSs) and their pre-main-sequence (PMS) phase is quite long (roughly 10 - 100 million years). More massive stars ($1.5\,\mathrm{M}_\odot < M < 8\,\mathrm{M}_\odot$) are called Herbig Ae/Be (HAeBe) stars. For massive stars, the collapse is faster. This heats up the core faster and, thus, fusion can start earlier, resulting in a shorter PMS phase (roughly 1 - 10 million years).

As the accretion of the infalling material onto the disk progresses, the envelope embedding the disk is accreted or dispersed by the radiation pressure from the central star. Moreover, the accretion of the disk material onto the star decreases, and the stellar radiation remains the only heating source. In this phase, stars have become PMS stars

($\sim$ 1 million years) and the system is referred to as Class II. It is believed that planets form in protoplanetary disks during this phase. Multiple (potentially concurrent) scenarios for the planet formation have been proposed. However, a clear view of these processes is still lacking. This ignorance is currently driving several studies, both observational and numerical, on protoplanetary disks around PMS stars. The final stage of this evolutionary path is a newly formed planetary system with a low-mass optically thin disk, called debris disk, which is composed of secondary dust resulted from collisions of planetesimals (see Sect. 1.2.3). These systems (Class III) are thought to be born roughly 10 million years after the onset of the initial collapse. A sketch illustrating the entire star and planet formation process is shown in Fig. 1.1.

1.2 Protoplanetary disks

This thesis, and therefore the rest of the introduction, is dedicated to protoplanetary disks at the Class II stage, when planet formation is thought to occur. Protoplanetary disks are rapidly-evolving structures where strong dynamical forces govern the interaction of multiple constituents. Their appearance is dictated by a complex interplay between gravity, thermal pressure, stellar radiation, magnetic field, and gas viscosity. This section aims to summarize our current view of the morphology and evolution of these objects, while Section 1.3 is dedicated to their observations.

1.2.1 Disk properties

Protoplanetary disks are made of gas and dust. Their spatial distribution significantly changes throughout the disk evolution and so does their relative abundance (and thus their interaction). When disks are formed, their composition is similar to that of the ISM, where the dust-to-gas ratio is $\sim$ 0.01. This value is therefore assumed for young disks too. Molecular hydrogen (H_2) and carbon monoxide (CO) are the main gas constituents. Most of the gas mass resides in the outer regions of the disk, up to several hundreds of astronomical units (AU). The gas density decreases with the radial separation R from the star. Gas masses are not well constrained. Estimates spanning 10^{-3} – 10^{-1} $M_\odot$ have been claimed (e.g., Williams & Cieza, 2011), even though those are often obtained by dividing reliable measurements of the dust mass by the aforementioned factor 0.01.

Despite its low abundance, dust dominates the disk opacity. Dust grains reprocess the stellar light, by absorbing UV/optical photons from the star and re-emitting the energy in the IR. This process is very efficient (up to 50% of the stellar light) and provides most of the observed IR radiation, as the accretion luminosity within the disk is negligible in Class II objects. The size and shape of the dust grains is a fundamental property in the context of planet formation, and their evolution with time is not entirely understood (see Sect. 1.2.2). Dust in the ISM is mainly composed of silicate and carbonaceous mate-

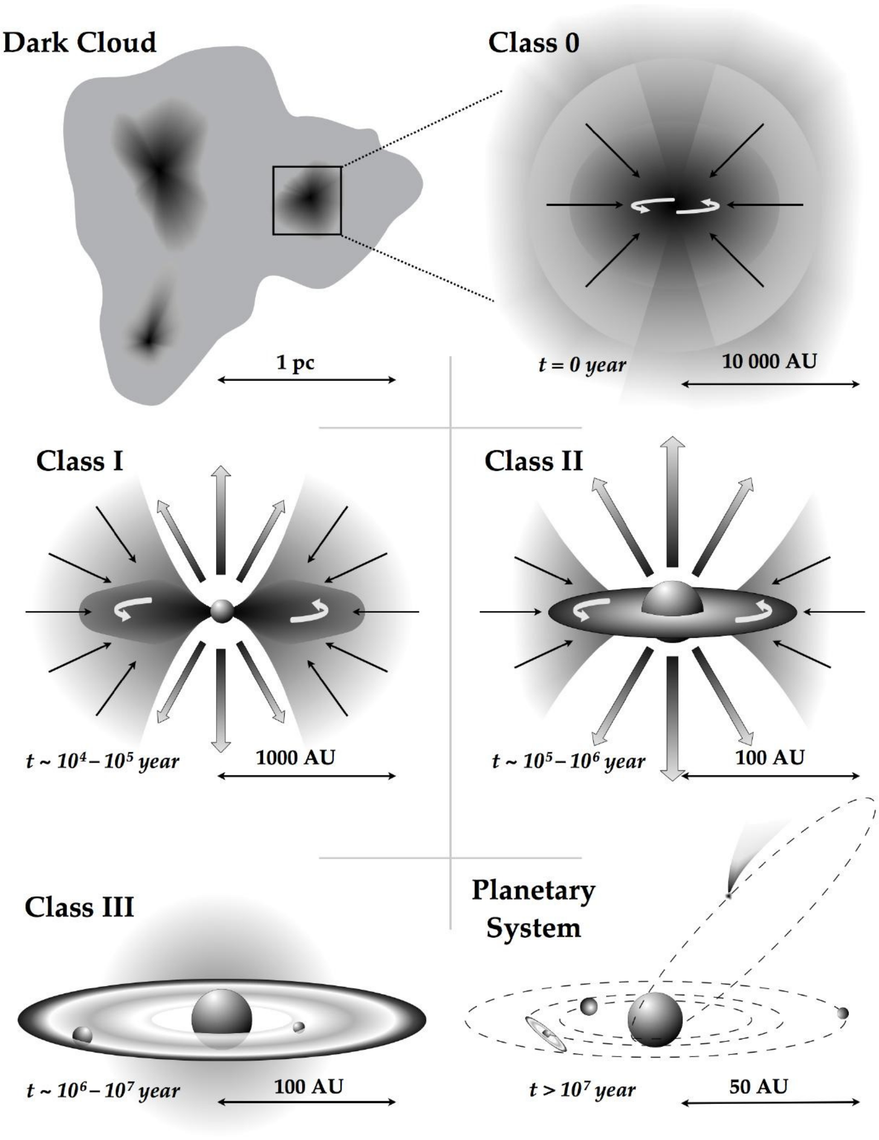

Fig. 1.1 — Sketch illustrating the stages leading from a dark cloud of the ISM to the formation of a planetary system. This figure is shown by kind courtesy of Wilfred Frieswijk.

rial, with typical grain size of $\sim 0.1\,\mu$m. The distribution of grain sizes a is typically parametrized as $n(a) \propto a^{-q}$ with q from 2.5 to 4.0 (e.g. Natta et al., 2007).

The peculiar physical structure of protoplanetary disks is dictated by their strong temperature and density gradient along both the radial and the vertical extents. The disk temperature is typically assumed to follow a power-law in the radial direction. Along the vertical direction, it dramatically varies from a few K at the disk mid-plane to thousands of K at the disk upper layer. At the mid-plane, because of the efficient self-shielding from the stellar radiation, molecules are frozen onto the dust grains. Further up, where temperatures are ~ 100 K, H_2 and CO dominates the gas abundance and an active molecular chemistry allows the creation of complex molecules (such as HCO+ and DCO+). Finally, in the upper layer the disk is directly exposed to high-energy photons and therefore molecules are photo-dissociated and atoms are ionized. Here the gas and dust temperatures severely depart from each other.

Since the disk is in hydrostatic equilibrium, the disk scale-height is strongly dependent on the temperature of the gas in the mid-plane. If we indicate with H the scale-height and with R the radius, disks for which the H/R ratio does not grow significantly with R are called flat disks. On the contrary, flared disks have a geometry for which this ratio increases with R. The amount of flaring can be expressed as $H(R) = H_0 \cdot (R/R_0)^{\beta}$ (e.g., Dullemond & Dominik, 2004) where H_0 and R_0 are the reference scale-height and radius and β the parameter quantifying the flaring ($\beta > 1$ for flared disks).

As the innermost part of the disk is directly illuminated, its gas temperature is high (more than 1000 K). Therefore, the scale-height of this region will be larger, creating an inner rim that can cast a shadow on the disk behind it (e.g., Dullemond et al., 2001). In this case the disk is self-shadowed. In a standard disk, the inner rim, often referred to as the wall, is located just outside the dust evaporation radius, i.e. the distance at which the dust grains sublimate because of the stellar radiation, occurring at T $\sim$ 1400 K (Muzerolle et al., 2003). This inner radius is thought to be at $\sim$ 0.04 - 0.2 AU for TTSs and $\sim$ 0.1 - 0.5 AU for HAeBe stars (e.g. Pinte et al., 2008). If and how much the disk is self-shadowed depends on both the dimension and optical depth of the rim itself (which in turn depends on the temperature of the gas) and the flaring angle of the outer disk.

1.2.2 Disk processes

Numerous physical processes drive the evolution of protoplanetary disks. Viscous accretion, dust grain growth, and dynamical interactions with forming planets are among the most important ones (and are the most pertinent to the subjects of this thesis). All these processes are tightly connected to the physical and chemical interaction between gas and dust. Therefore, even though this work is mostly dedicated to the dust, we must dedicate a few lines on the dynamics of the gaseous disk.

To accrete, the gaseous disk must lose angular momentum. Understanding how this occurs is a key-challenge for the current theories of disk evolution. In a Keplerian disk, particles at different radii rotate with a different velocity. This leads, in a viscous fluid, to collisions between molecules at different radii that, in turn, result in outward transport of angular momentum. However, the molecular viscosity of the gas is too small to lead to any appreciable disk evolution. Many sources of disk turbulence can potentially provide the viscosity required for the viscous transport to occur (see review by Armitage, 2015). Here we mention only the traditionally favored (though debated) idea, i.e. the magneto-rotational instability (MRI). According to this theory, weakly magnetized disks are subject to a powerful axisymmetric shearing instability (Balbus & Hawley, 1991). The magnetic

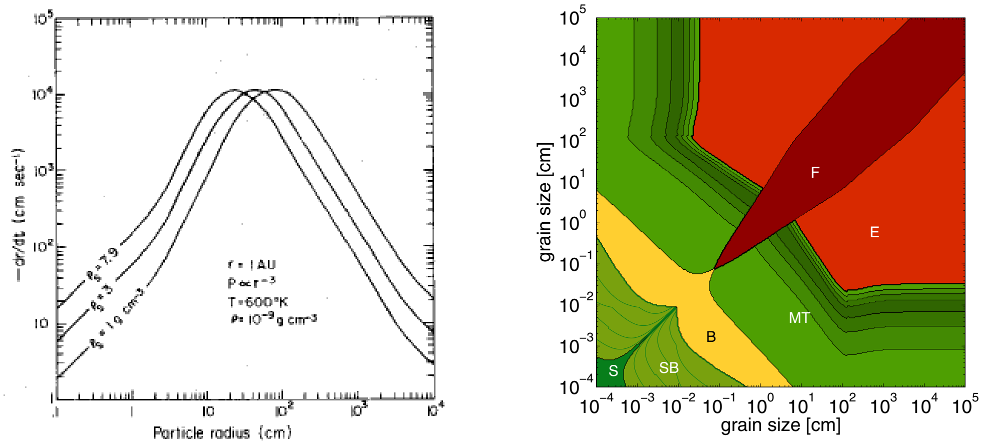

Fig. 1.2 — Diagrams illustrating the concept of the meter barrier. *Left panel:* Radial drift distribution for particles at 1 AU with different sizes (Weidenschilling, 1977). The three curves indicate different dust densities. *Right panel:* The outcome of collisions between particles with different sizes, as derived with numerical models by Windmark et al. (2012). Green regions indicate growth-positive collisions, yellow -neutral, and red -negative. S marks sticking, B bouncing, MT mass transfer, E erosion, and F fragmentation.

field causes two fluid elements on neighboring orbits to be coupled. Since the outer element rotates slower, it exerts a backward pull on the inner fluid element, thus removing angular momentum from it. That element will therefore get closer to the star, while the outer one will gain angular momentum and, thus, it will move to an orbit further out. The spring generated by the coupling of the two elements then stretches and the effect increases. Since this effect is not damping or self-regulating, it causes an instability within the disk. An important aspect of this scenario is that in the disk mid-plane the electron fraction can be so low that the MRI cannot proceed. In this region the accretion would be severely hindered and one would refer to it as a dead zone.

In general, the gas pressure in disks decreases with radius. This causes the azimuthal component of the gas velocity to be slightly sub-Keplerian. On the other hand, dust particles move at the Keplerian velocity and therefore experience a head-wind that acts to slow them down causing an inward spiraling. The amount of this dust radial drift depends on the particle size. Smaller grains are well coupled to the gas in its motion and thus do not perceive the gas wind. For very large grains, the effect also becomes small because of their increased mass/surface ratio. More quantitatively, one can calculate that the maximum radial drift is obtained for particles with size of 10 cm − 1 m, and can be as large as $\sim 10^4$ cm s^{-1} (Weidenschilling, 1977, see Fig. 1.2a). These velocities would result in all particles in the disk to be accreted onto the star in only ~ 100 years. This is the first of the two aspects concurring to raise the so-called meter barrier.

Radial drift is one of the many motions experienced by dust grains in protoplanetary disks (see Fig. 1.3 and the review on dust processes by Testi et al., 2014). Dust grain growth is the central process in the study of the planet formation. Sub-μm-sized grains inherited from the ISM must grow to the frequently observed cm-sized grains (see Sect. 1.3.2) and eventually turn into planetesimals (see Sect. 1.2.3). Frequent collisions between grains are the natural result of the very different velocities experienced by grains. These are provided by both the aforementioned radial drift and the radial/vertical dust mixing caused by the intrinsic gas turbulence. The outcome of these collisions primarily depends on the relative velocity and size of the grains involved. Sophisticated treatments, both numerical and from laboratory experiments, study the impact of many other factors, such as the dust composition, presence of icy molecules, shape of the particles, and impact angles. For the scope of this introduction, it is sufficient to present the result of Fig. 1.2b (from Windmark et al., 2012). From the figure, it is clear how the impact of meter-sized particles or bigger does not enable any further growth but rather acts to fragment the solids. This is the second effect contributing to the meter barrier.

All this said, it is clear that in the *nominal* conditions of an axisymmetric continuous disk, planet formation is challenging. Thus, scientists are intensely searching for particular disk regions where dust particles can be *trapped*. Dust trapping provides a solution to the meter barrier problem, as it prevents dust particles both to rapidly accrete onto the star and to reach velocities incompatible with further sticking. A local pressure bump is a possible origin of a dust trapping, as the positive pressure gradient at its inner edge could reverse the drift direction (Whipple, 1972). Anti-cyclonic vortices have been proposed as responsible for dust trapping (Klahr & Henning, 1997), and can be generated in the disk because of e.g., Rossby-wave instability (Lovelace et al., 1999). Alternatively, pressure bumps could be generated at the outer edge of planet-induced disk gaps (see Sect. 1.2.4) or at the outer edge of the aforementioned dead zones.

Another possibility is that dust traps are connected to the so-called disk ice-lines. The ice-line of a certain gas species is the location in the disk where the temperature drops below the freeze-out temperature of that species. This line separates the ice-free region from that where molecules are mostly frozen onto the dust grains. Therefore, at the ice-line grain structures dramatically change in a small range of radii. The location of the ice-lines (and in particular of the water snow-line) affects both the efficiency of the planet formation and the composition of the planetary atmospheres. For example, it has been invoked to explain why our Solar System has only terrestrial planets inward of it and only giant gaseous planets outward. More importantly for our scope, dust particles mantled with ice are more prone to stick together. Therefore, outside of the ice-line the threshold velocity for grain fragmentation is higher and this results in a slightly larger family of dust grains than inside the snow-line. As shown above, drifting velocities of larger particles are smaller and, thus, a pile-up of dust grains may occur at the ice-line.

1.2.3 Planetesimals and planets

The observation of hundreds of extrasolar planets and the increased computational power achieved in the last years enabled us to drastically improve our understanding of the planet formation. Even though the various planet formation theories are not discussed in depth

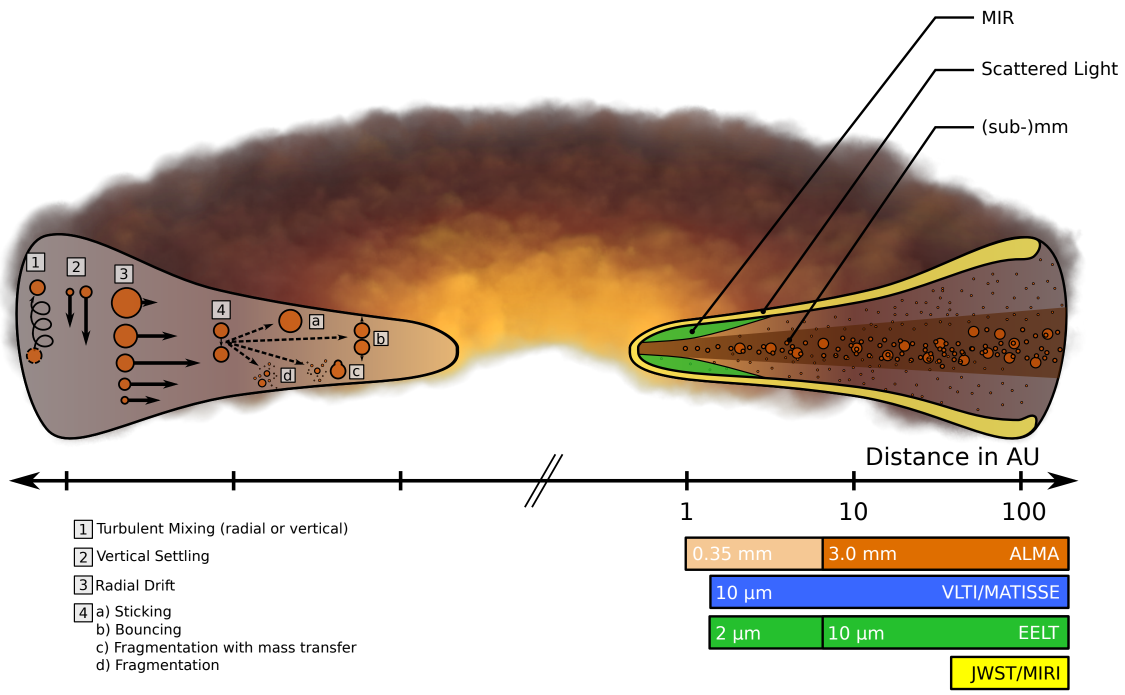

Fig. 1.3 — Illustration of the disk structure (from Testi et al., 2014). Dust grain processes are depicted on the left half, with lengths of the arrows indicating the typical velocities of grains. Upcoming or newly operational instruments to probe different disk regions are highlighted in the right half.

in this thesis, an illustration of their basic principles is necessary. Typically, models focus on the formation of either terrestrial planets (up to 10 Earth masses) or giant planets.

It is widely thought that terrestrial planets form by agglomeration of smaller bodies called planetesimals. These km-sized, either rocky or icy, bodies are similar to our asteroids and Kuiper belt objects and are thought to be the last stage of intense growth experienced by dust grains inside the dust traps. Simple coagulation is no longer an efficient growth process for planetesimals. Their accretion is instead regulated by their gravitational interaction with a swarm of other bodies. The commonly accepted paradigm is that a planetesimal with a slightly larger mass than the neighbors will become the dominant body and thus undergo a runaway accretion, so as to grow up to 1,000 km in size (being now referred to as a planetary embryo). A slow-down of runaway growth leads to the creation of similar-sized planetary embryos that interact with each other in oligarchic growth. An alternative model called pebble accretion has been proposed by Lambrechts & Johansen (2012), who argued that a large planetesimal can grow up to several Earth masses through the rapid collapse of a cloud of pebbles of a few decimeters in size.

The two main giant planet formation models are the *core accretion* (Lissauer & Stewart, 1993; Safronov & Zvjagina, 1969) and the *disk instability* (Cameron, 1962; Kuiper, 1951). The first steps in the formation of a giant planet through core accretion is similar to that for terrestrial planets. The main idea of this theory is that the planetary embryo accreted by the planetesimals can reach a mass as large as a fraction of terrestrial masses. These masses are so high that the escape velocity exceeds the speed of the local disk mass, enabling the capture of this gas. When the mass of the gas approaches that of the original embryo the process becomes extremely rapid. Gas accretion is eventually stopped by the lack of surrounding material (for either disk dissipation or planet-induced gap). On the other hand, the formation of giant planets in the disk instability model is connected to the disk fragmentation. If the effects of the disk instability dominate over the disk thermal pressure, disk perturbations grow and lead to density enhancements. These clumps may eventually evolve to become gravitationally bound planets. The core accretion and disk instability models are not necessarily competing processes. Disk instability may occur at the first stages of evolution (0.1 Myr), while core accretion is most likely to happen at later stages (few Myr).

1.2.4 Disk evolution

All processes discussed in Sect. 1.2.2 have an impact on the global disk geometry. This means that the observation of disks at different evolutionary stages provides insight into modalities and timeframes of these processes. Here we describe two particular aspects of the disk evolution, connected to the disk radial and vertical extents.

Globally speaking, the disk vertical scale height is thought to decrease with time. At the first stages of the star formation, this is due to the envelope flattening during the cloud contraction (see Sect. 1.1). During the Class II stage, disk flattening is the result of the dust settling toward the mid-plane (e.g., Weidenschilling, 1980). This effect is particularly dramatic for large particles, whose intrinsic vertical oscillation due to orbital motion is damped by the gas. Dust settling is a key-process for planet formation, as it favors the collisions of large grains at the mid-plane. Collisions of large particles provide replenishment of smaller grains, which are less subject to settling. Thus, the net effect is an increasingly stratified disk structure with larger grains concentrated to the center. This process also leaves the gas in the upper layer exposed to direct stellar radiation, so as to favor photo-evaporation (see below).

The radial structure of the disk is thought to evolve outward, with the inner regions experiencing much more rapid changes. A number of processes concur to determine this evolution, with the photo-evaporation (e.g., Hollenbach, 1994) and the interaction with orbiting companions (e.g., Rice et al., 2003) being the most effective ones. The former effect is caused by high-energy photons released by the stellar chromosphere (UV and X rays). These photons can heat the hydrogen up to 10,000 K, making the thermal velocity of the gas higher than the escape velocity and thus triggering a material loss in the form of a wind. This process is inefficient until the viscous accretion described in Sect. 1.2.2 is high ($\sim 10^{-10}\,M_{\odot}$/yr, Alexander & Armitage, 2007), as the accretion resupplies the disk with outer material. Eventually, the accretion is no longer able to sustain the replenishment and a hole is created at a few AU from the star. This hole leaves the gas even more

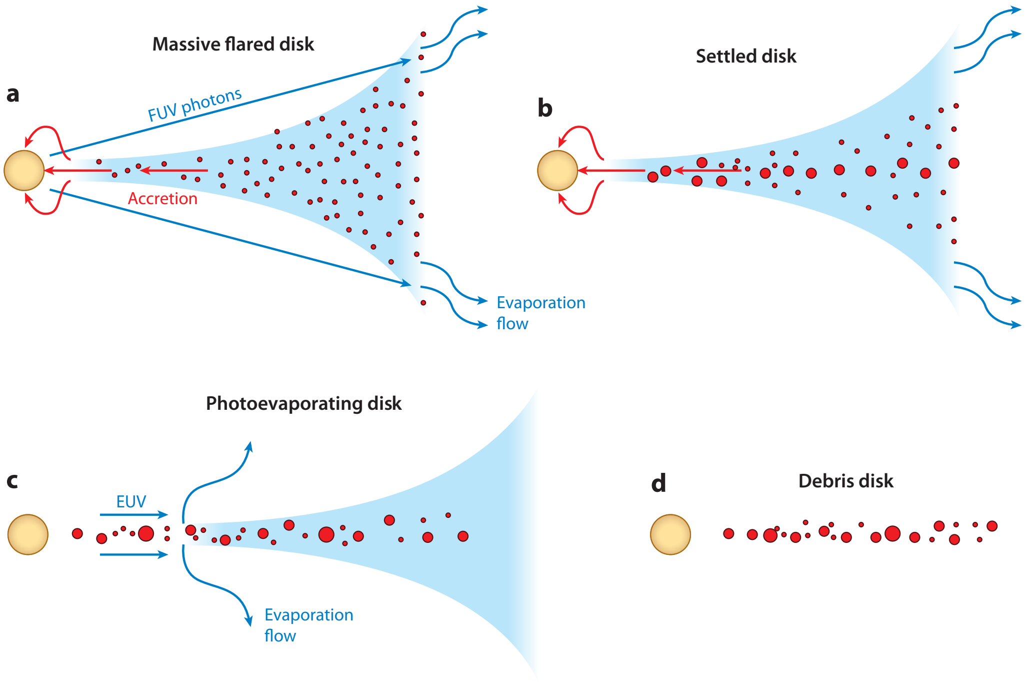

Fig. 1.4 — Sketch of the disk evolution (Williams & Cieza, 2011). Gas is shown in blue and dust in red.

exposed to high-energy photons and therefore the process is boosted.

The morphology of the disk is also significantly affected by the presence of orbiting companions. In fact, forming planets embedded in the disk can become massive enough (roughly 1 Jovian mass) to exert a repelling force on particles orbiting at the same distance from the star. This generates a disk gap with width and depth dependent on the planet and disk properties. However, some material may still accrete the planet in form of streams. For very massive planets, this accretion may effectively diminish the amount of material inward of the planet, so as to create a large cavity at the disk center.

Regardless of the process responsible for the disk sculpting, we refer to objects with a central cavity as *transition disks*, as these are thought to be in transition between a primordial gas-rich disk and a debris disk (see Sect. 1.1). A sketch of the evolutionary processes described in this section is shown in Fig. 1.4. The disk lifetime is another fundamental parameter for the theory of the planet formation, as it sets an upper limit to the time available for planets to form. This value is not well constrained and can significantly vary with the environment conditions (e.g., stellar mass, presence of stellar companions, location in the galaxy). Typical values span a range from 1 Myr to 20 Myr.

1.3 Observations of protoplanetary disks

Most of our knowledge about the universe has been gained through the electromagnetic radiation. This is particularly true for protoplanetary disks, despite the fact that only a minor fraction of their brightness is intrinsic. In fact, nearly all the radiation that we detect from optical to radio wavelengths is the result of the interaction of the stellar light with the disk. This is why the observational study of protoplanetary disks, in particular at short wavelengths, cannot ignore the properties of the central star.

In the basic structural framework, the stellar light is intercepted by the higher disk regions and then re-radiated to space or deep into the disk. Since dust dominates the opacity balance, most of this re-radiated emission is in form of spectral continuum. The two contributions to this continuum are from thermal (re-processed) and scattered (reflected) radiation, where the former is the dominating source.

The thermal emission from the disk spans a range of almost five orders of magnitude in wavelength. These wavelengths reflect the temperature of the disk region where the radiation is released, with the disk surface in the inner few AU contributing to the 1-5 μm interval (near-IR), the surface at larger radii to the 5-25 μm (mid-IR), and the outermost and deeper regions to the 25-350 μm (far-IR) as well as longer wavelengths (millimeter and radio regime). The disk emission is typically optically thick up to the far-IR, whereas it becomes optically thin at longer wavelengths.

In this section, we describe a (inevitably non-exhaustive) number of observational techniques applied to the study of the dusty disks. We focus on their spectral energy distribution, on their thermal emission at long wavelengths, and on the scattered light in the visible and near-IR regime.

1.3.1 Spectral energy distribution

The tool that we use to evaluate the amount of energy released as a function of wavelength is the Spectral Energy Distribution (SED), where the product λF_λ (with F_λ flux at wavelength λ) is plotted against λ. An example of SED of a protoplanetary disk is shown in Fig. 1.5 (from Garufi et al., 2014a). The main contributor to the SED is the direct stellar radiation, which appears as a black body emission peaking in the visible/near-IR (depending on the stellar surface temperature). A prominent IR excess, extending up to cm wavelengths, is the result of the re-processing of the stellar light by the disk. The turnover from the optically thick to thin regime can be seen from the figure at roughly 300 μm. On top of this continuum, one typically finds broad mid-IR features, tracing the mineralogy of the surface dust, as well as near-IR/far-IR emission lines, probing warm/cold gas in the disk (primarily CO, CH^+, and O). Furthermore, SEDs may show optical emission lines and UV/optical excess produced in the accretion flows or in the accretion shocks at the stellar photosphere.

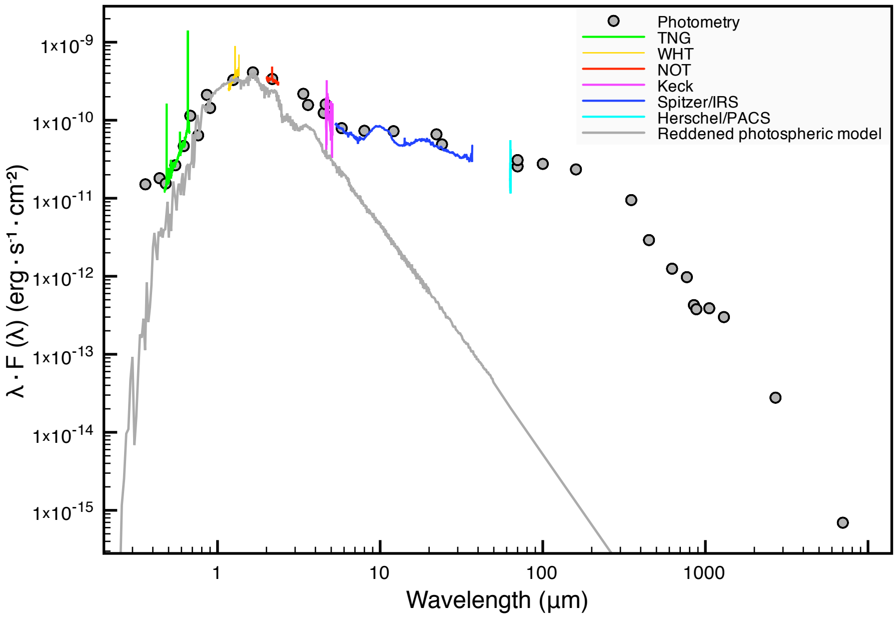

Fig. 1.5 — Illustrative SED of a protoplanetary disk (around the low-mass star FT Tau, from Garufi et al., 2014a). The grey line is the model of the stellar emission. The different colored lines are spectra from ground/ and space/based telescopes. The errors on the photometric measurements are not visible at this scale. Both a UV/ and a IR/excess are clearly visible.

All processes described in Sect. 1.2.4 causes the SED to change with time. The most dramatic changes are related to the dust settling and disk dissipation. The IR excess is thought to decrease with time as the disk switches from a strongly flaring geometry to a flat one. This is because of the decreasing disk surface exposed to the stellar light. In particular, Meeus et al. (2001) proposed an observational distinction between Herbig Ae/Be stars with mid-/far-IR excess scaling with wavelength as a power-law continuum (Group II) and those where an additional cold component is necessary to reproduce the observed trends (Group I). This distinction has been interpreted in the framework of dust grain growth and settling, with Group I objects being the ancestors of Group II.

Also the inside-out depletion of material shows an imprints in the SED of disks. A small sample of disks (the transition disks discussed in Sect. 1.2.4) shows a peculiar dip in the IR excess (see Fig. 1.6), indicating the depletion of warm dust near the central star (Strom et al., 1989). Interestingly, a sub-group of transition disks shows a small near-IR excess, which indicates the presence of some material very close to the star. This morphology has been proposed to be the last stage of accretion of material inside the newly created gap, and the class of objects has been named as pre-transition disks.

SEDs alone do not allow unequivocal inference of the disk structure because of the structural degeneracies of the many parameters involved. To break these degeneracies, resolved data are necessary. The next two sections are thus dedicated to disk imaging.

1.3.2 Thermal millimeter images

Being the nearest protoplanetary disks at $\gtrsim$ 100 parsec from us, their observations require a spatial resolution of at least the order of the arcsecond. The resolution θ of an observation is primarily set by the wavelength λ and the mirror diameter D, according to $\theta \approx 1.22\ \lambda/D$. This makes the resolution appropriate for the disk imaging unachievable by single dish telescopes for most of the electromagnetic spectrum. Thus, interferometric observations are necessary. At mid-IR wavelengths, interferometric imaging provides a unique tool to resolve the thermal emission from the few inner AU. However, most of the disk radial extent remains unaccessible at these wavelengths and requires (sub-)mm and radio imaging.

Most of the disk emission at wavelengths longer than the far-UV is optically thin. This means that (sub-)mm observations trace the product of temperature, opacity, and column density of the disk. The standard approach to this degeneracy is to assume the opacity constant through the disk, and fit for temperature and column density (typically scaling with radius as a power-law) with some considerations on the disk geometry (i.e. cut-off radius and inclination). The disk opacity is primarily dictated by the dust grain size a, since the particle cross-section dramatically affects the interaction with the incident radiation. The opacity spectrum scales as λ^{-2} in the Rayleigh regime (i.e. when $a << \lambda$), is roughly constant for $a >> \lambda$, while is enhanced when $a \sim \lambda$. This means that (sub-)mm observations mostly trace mm-sized particles, which contribute to most of the dust mass.

Recently, many interferometric images have shown disk structures strongly deviating from an axisymmetric profile. In particular, few tens of transition disks have been imaged as ring-like structures, with significant contrasts between two opposite disk sides. An example of such horseshoe structures is shown in the inset images of Fig. 1.6. These large-scale asymmetries capture the attention of the community, as they are potential sights for the dust accumulation described in Sect. 1.2.2, even though it is not clear whether they can be non-transient vortices.

Our knowledge of the disk structure will greatly benefit from the newly operational ALMA (Atacama Large Millimeter Array), a large interferometer located on the Chajnantor plateau in Chile and composed of 73 antennas movable over distances as large as 16 km. The angular resolutions ($< 0.01''$) provided by ALMA are revolutionizing the field of (sub-)mm disk imaging since, with interferometers like SMA, CARMA, and ATCA, resolutions of $0.2''$ at best could be achieved so far.

1.3.3 Scattered light images

Light scattering is the other phenomenon of light-matter interaction, consisting in the deviation of a photon from its direction of propagation with the energy of the photon remaining unchanged. Scattered light, though marginal in the radiation budget, is a fun-

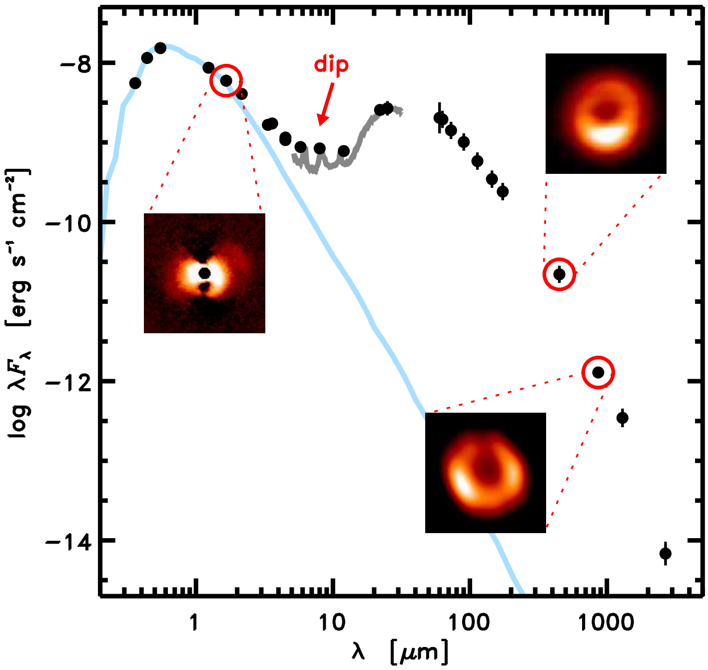

Fig. 1.6 — Illustrative SED of a transition disk (around the solar-type star SR21, from Andrews, 2015). The three inset images show the 1.6 μm scattered light (Follette et al., 2013), as well as the 450 μm (Pérez et al., 2014) and 870 μm (Brown et al., 2009) thermal emission from the source.

damental tool to investigate the morphology of protoplanetary disks, and is the main focus of this thesis.

The study of scattering by cosmic dust is challenged by the complexity of the dust optical properties. The computation of the optical properties would require to solve the Maxwell equations for the interaction of incident light with particles. As this is a very complex exercise, the shape of the dust particles is often simplified. Scattering from spherical particles can be explained by the Mie theory (Mie, 1908). However, most cosmic grains are not homogeneous spheres and the optical properties computed in Mie theory often dramatically deviate from realistically shaped particles. Thus, computationally demanding algorithm are typically employed. These approaches study the dependence of the optical properties on four grain characteristics: composition, size, shape and structure (see e.g., Min, 2009).

Observations of protoplanetary disks at optical/near-IR wavelengths mostly reveal stellar light that is scattered by the disk. In fact, the thermal emission at those wavelengths is limited to the few inner AU or even only to the star itself. For a particle with a given size a, the distribution of scatters peaks at wavelength $\lambda \sim 2\pi a$. This means that, analogously to the fact that millimeter observations trace mm-sized particles, optical/near-IR observations are mainly sensitive to μm-sized particles. The dust opacity at such short wavelengths is so high that these observations only trace a thin surface layer of the disk.

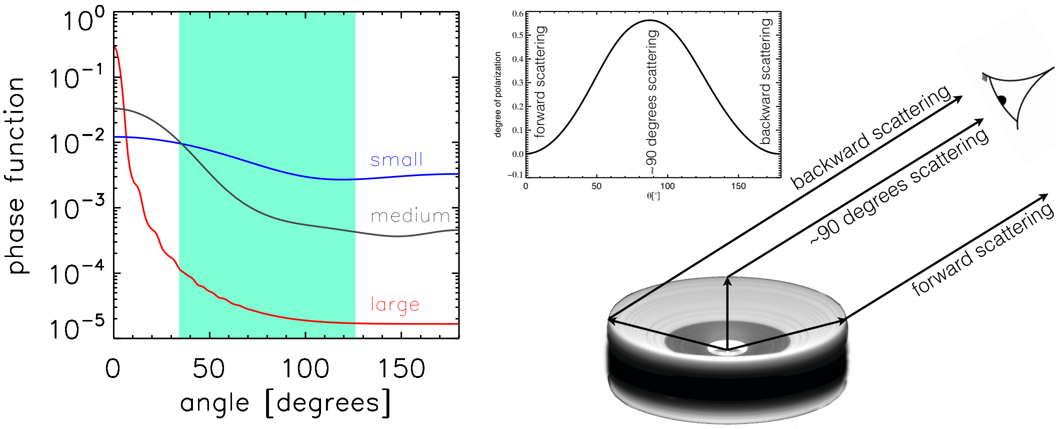

Fig. 1.7 — Scattering phase function and polarization phase curve. The left plot shows the distribution of scattering angles for small (0.08 μm), medium (0.25 μm), and large (2.5 μm) dust grains at 0.6 μm wavelength (from Mulders et al., 2013a). The green area marks the interval of observed angles from a $\sim 45°$ inclined disk. The right sketch illustrates the scattering angles observed from different sides of an inclined disk. The central inset shows how the degree of polarization typically varies with the scattering angle (from Min, 2015). Observations in polarized light measure the combination of these two curves.

The amount of scattered light that we receive depends on multiple factors. The primary parameter describing the efficiency of scatters is the single scattering albedo. This number expresses the fraction of incident light that is scattered by the grain in all directions. However, the distribution of scattering angles (the scattering phase function) is typically not isotropic. This is particularly true for large particles, which tend to scatter photons more heavily toward the forward direction (see left panel of Fig. 1.7). This effect is very important for observations of face-on and moderately inclined disks, since photons scattered by a few tens of degree do not reach the observers. In other words, we may not observe most of the light scattered by large grains if the disk is not seen (almost) edge-on.

The natural advantage of the observations in the visible and near-IR is the exquisite angular resolution that ground telescopes with few-meter mirrors achieve. Facilities supported by adaptive optics (AO) to correct for atmospheric distortions (like the 8-m Very Large Telescope at Cerro Paranal, Chile) provides diffraction-limited imaging with resolution as good as $\sim 0.02''$ in the visible. Given the distance of the most nearby protoplanetary disks, this resolution allows us to resolve structures of a few AU scale. However, observations of protoplanetary disks have to face a major challenge, which is the very high contrast between the brightness of the disk and that of the central star (a few orders of magnitude). To mitigate this issues, several differential imaging techniques have been developed. Here we mostly focus on Polarimetric Differential Imaging (PDI), since most of the observations of this thesis have been obtained with this technique.

PDI exploits the different characteristics of stellar and scattered light, with the former being essentially unpolarized and the latter being significantly polarized because of the partial alignment of non-spherical grains. Thus, the combination of simultaneous observations taken with different (orthogonal) polarization states cancels out the stellar contribution but leaves the scattered light from the disk (mostly) unchanged. Observations obtained in PDI are typically described by the Stokes formalism (e.g. Tinbergen, 2005), which uses the four Stokes vectors I (intensity), Q, U (two components of linear polarization), and V (circular polarization, negligible in protoplanetary disks). The scattered light obtained in PDI is only a fraction of the total scattered light from the disk. In fact, the amount of polarization of scattered photons (the polarization phase curve) depends on the scattering angle. As shown in Fig. 1.7, this curve typically peaks at $\sim 90°$. However, the exact shape of the polarization degree, analogously to the phase function, is not known. This means that scattered light images of even only slightly inclined disks are unpredictably affected by the product of phase function and polarization phase curve.

During the last decade, a number of polarimeters mounted on 8-m telescopes have provided several exquisite PDI images of protoplanetary disks. Subaru/HiCiao and VLT/NACO have been until 2014 the superior instruments. The new-generation VLT/SPHERE and GPI recently started operations and thus opened, in conjunction with ALMA, a new era for the high-resolution imaging of protoplanetary disks.

1.4 This thesis

This thesis is an observational study of protoplanetary disks, spanning over a timescale of four years. During this period, several questions concerning these intriguing objects were raised. All questions aim to contribute, in small ways, to the key-question "How do planets form?" and can be classified into three main lines of research, sorted from the most specific to the most global framework:

1. *The interpretation of scattered light images.* We need to address, among many other points, (*i*) what disk regions and dust grains are traced by these observations, (*ii*) what are the degeneracies and the biases in our images, (*iii*) how these biases change with the disk properties, and (*iv*) what is the instrumental contribution and the impact of the data reduction processing.

2. *The morphology of protoplanetary disks.* Scattered light images are food for thoughts for e.g., (*i*) the distribution of small dust grains in planet-forming disks, (*ii*) how this differs from the other disk constituents, and (*iii*) what physical processes are responsible for any peculiar distribution or differentiation of the dust.

3. *The evolution of protoplanetary disks.* An increasing number of disks observed in scattered light raises questions on (*i*) what analogies/differences exist among multiple objects, (*ii*) whether any evolutionary paths can be inferred from disks with different morphologies, and (*iii*) what disk processes can be studied from the diversity of disk morphologies.

In all three main chapters of the thesis, we analyze new scattered light images of protoplanetary disks and discuss the results in the framework of these lines of research. In Chapter 2 we illustrate near-IR VLT/NACO observations of the fascinating disk around SAO 206462. This work provides the first evidence from direct imaging of stratified inner edge in transition disks. We estimate the mass and the location of a (yet unseen) giant planet potentially responsible for the differentiation of the disk components (gas, small and large dust grains) at the outer edge of the disk cavity. We discuss other possible scenarios for the formation of the cavity and for the prominent double spiral-arm structure visible from the images.

In Chapter 3 we analyze the marginal- and non-detections of three disks from VLT/NACO images obtained in 2012. The disk around HD163296 is seen in scattered light with a gapped distribution maximized along the disk major axis. The notion that this object is not a transition disk led to a number of hypotheses to explain the disk geometry. This investigation proceeded with new VLT/NACO observations of the source in 2015 to validate or reject the proposed scenarios. The chapter also highlights the importance of non-detections, as these contain pivotal information on the disk geometry in the framework of the Group I vs II classification. This discussion also challenges our view of the global disk evolution.

Finally, in Chapter 4 we show the first VLT/SPHERE images of HD100546, in both visible and near-IR. These data are a showcase of the capability of the new generation high-contrast imager SPHERE but also raise key-questions on the disk interactions with (forming) planets, as this disk is thought to host two protoplanets. This work also starts a discussion on the new (potentially recurrent) form of disk features that new generation instruments reveal.

The thesis ends with concluding remarks and outlook in Chapter 5, where we outline our current view of the questions raised above and discuss the future observational approach to the study of protoplanetary disks.

Maybe the time is not quite yet. But those other worlds, promising untold opportunities, beckon. Silently, they orbit the Sun, waiting.

CARL SAGAN, *"Pale Blue Dot", 1994*

2

Small vs large dust grains in transition disks: do different cavity sizes indicate a planet?

SAO 206462 in polarized light with VLT/NACO

Based on a paper published in
Astronomy & Astrophysics, 560, A105 (2013)

A. Garufi[1], S.P. Quanz[1], H. Avenhaus[1], E. Buenzli[2,3], C. Dominik[4], F. Meru[1], M.R. Meyer[1], P. Pinilla[5,6], H.M. Schmid[1], S. Wolf[7]

Received 2 August 2013 / Accepted 13 November 2013

---

[1] Institute for Astronomy, ETH Zurich, Wolfgang-Pauli-Strasse 27, CH-8093 Zurich, Switzerland

[2] Department of Astronomy and Steward Observatory, University of Arizona, Tucson, AZ 85721, USA

[3] Max-Planck Institute for Astronomy, Königstuhl 17, D-69117, Heidelberg, Germany

[4] Sterrenkundig Instituut Anton Pannekoek, Science Park 904, 1098 XH Amsterdam, The Netherlands

[5] Universität Heidelberg, Zentrum für Astronomie, Institut für Theoretische Astrophysik, Albert-Ueberle-Str. 2, 69120 Heidelberg, Germany

[6] Leiden Observatory, Leiden University, PO Box 9513, 2300 RA Leiden, the Netherlands

[7] University of Kiel, Institute of Theoretical Physics and Astrophysics, Leibnizstrasse 15, 24098 Kiel, Germany

Abstract

We obtained VLT/NACO near-IR high-resolution polarimetric differential imaging observations of SAO 206462 (HD135344B). A face-on disk is detected in *H* and K_s bands between 0.1″ and 0.9″. No significant differences are seen between the *H* and K_s images. In addition to the spiral arms, these new data allow us to resolve for the first time an inner disk cavity for small dust grains. The cavity size (≃ 28 AU) is much smaller than what is inferred for large dust grains from (sub-)mm observations (39 to 50 AU). This discrepancy cannot be ascribed to any resolution effect. The interaction between the disk and potential orbiting companion(s) can explain both the spiral arm structure and the discrepant cavity sizes for small and large dust grains. One planet may be carving out the gas (and, thus, the small grains) at 28 AU, and generating a pressure bump at larger radii (39 AU), which holds back the large grains. We analytically estimate that, in this scenario, a single giant planet (with a mass between 5 and 15 M_J) at 17 to 20 AU from the star is consistent with the observed cavity sizes.

2.1 Introduction

As discussed in Sect. 1.2.4, the study of different dust components in and around the central cavity of transition disks provides insights into the mechanisms of planet formation. Direct detections of these cavities have been provided, among others, by the Submillimeter Array (SMA) interferometer (e.g. Andrews et al., 2011, 2009) at sub-millimeter wavelengths, and by VLT/NACO (e.g. Quanz et al., 2013a, 2011) and Subaru/HiCiao (e.g. Hashimoto et al., 2012; Mayama et al., 2012) in near-IR polarized light. Sub-millimeter and near-IR data probe different dust grain sizes (and, thus, different disk layers). Intriguingly, in some cases they are suggesting unexpected differences in the small and large dust grain distribution. Dong et al. (2012) highlighted that the polarized near-IR images from Subaru/HiCiao do not always show the inner cavities observed at millimeter wavelengths with SMA as close as the inner working angle (0.1″ − 0.2″). Their model suggests a decoupled spatial distribution of the big and small dust particles inside the cavity.

In this chapter, we analyze PDI observations of the transition disk around SAO 206462 (HD135344B) obtained with VLT/NACO and presented by Garufi et al. (2013). SAO 206462 is an extensively studied, rapidly-rotating (Müller et al., 2011) F4Ve star (Dunkin et al., 1997) hosting a transition disk. It is located in the Sco OB2-3 star-forming region (d = 140 ± 42 pc, van Boekel et al., 2005). The angular separation from HD 135344A is 21″ (Mason et al., 2001), which translates into a physical separation > 2900 AU. The proper motions of the two stars are comparable (Høg et al., 2000). Thus, in a scenario where the stars have highly eccentric orbits, a gravitational interaction between them cannot be ruled out. Spatially resolved imaging in the near-IR (Vicente et al., 2011) ruled out the presence of stars more massive than 0.22 $M_\odot$ at 0.1″, and of any brown dwarf at separations larger than 0.27″. Table 2.1 shows the stellar parameters of SAO 206462.

The properties of the disk around SAO 206462 have been constrained via imaging (e.g. Grady et al., 2009; Muto et al., 2012), spectroscopy (e.g. Brown et al., 2007; Dent et al., 2005), and interferometry (e.g. Andrews et al., 2011; Fedele et al., 2008). A large inner dust cavity ($R < 40 - 50$ AU) has been predicted by SED fitting (Brown et al., 2007) and successively imaged at sub- and millimeter wavelengths (Brown et al., 2009; Lyo et al., 2011). Grady et al. (2009) and Muto et al. (2012) both resolved the disk in scattered light but no evidence of the inner hole was found down to $\sim$ 42 AU and $\sim$ 28 AU respectively. In particular, the Subaru/HiCiao observations by Muto et al. (2012) revealed two small-scale spiral structures, with the brightest portion of the spirals roughly coinciding with the thermal emission peak at 12 μm (Mariñas et al., 2011). An enhanced emission to SE side and a deficit to north are observed in all sub- and millimeter images and in the 1.1 μm HST/NICMOS data (Grady et al., 2009). The presence of gas in the inner cavity has been inferred by Pontoppidan et al. (2008) by means of CO rovibrational lines, and van der Plas et al. (2008) by means of [OI] 6300 Å line. The presence of a narrow (sub-AU scale) inner dust disk has been inferred by SED modeling (Brown et al., 2007; Grady et al., 2009) and interferometric N-band observations (Fedele et al., 2008). A variable mass accretion rate of a few 10^{-8} $M_\odot$/yr has been derived by Sitko et al. (2012) from emission lines. The disk inclination is consistently estimated to be $11 - 14^\circ$ by Dent et al. (2005), Pontoppidan et al. (2008), Andrews et al. (2011), and Lyo et al. (2011). Periodic variations of the photospheric emission indicates a stellar inclination of $\sim 11^\circ$ (Müller et al., 2011), suggesting aligned star−disk angular momentum. However, Fedele et al. (2008) estimated the inclination of the inner dust disk to be $\sim 60^\circ$. Ellipse fitting of mid-IR imaging suggests a larger inclination also for the outer disk ($i = 40 - 50^\circ$, Doucet et al., 2006; Mariñas et al., 2011).

The chapter is organized as follows. Firstly, in Sect. 2.2 and Sect. 2.3 we describe the observations and the NACO data reduction. Secondly, in Sect. 2.4 we present the results from the PDI images of SAO 206462 and, finally, in Sect. 2.5 we discuss a possible scenario for the origin of the structures in the dusty disk of the source.

2.2 Observations

The observations were performed on 2012 July 24 with the high-resolution near-IR instrument NAOS/CONICA (NACO, Lenzen et al., 2003; Rousset et al., 2003), mounted on UT4 at the Very Large Telescope (VLT). We used the SL27 camera (pixel scale = 27 mas pixel^{-1}) in *HighDynamic* mode and readout in *Double RdRstRd* mode. SAO 206462 was observed in the context of a small survey of Herbig Ae/Be disks performed with VLT/NACO in PDI mode on three consecutive nights. The sample contains, among others, HD169142 (Quanz et al., 2013b) and HD142527 (Avenhaus et al., 2014b). We obtained images of SAO 206462 in H, NB 1.64, K_s, and NB 2.17 filters. The use of narrow band filters is due to the complementary need for exposures with the central star unsaturated, which is unachievable with broad band filters. The total integration times

Tab. 2.1 — Basic properties of SAO 206462.

Parameter	Value
Right ascension (J2000)	$15^{\mathrm{h}}\ 15^{\mathrm{m}}\ 48^{\mathrm{s}}.44$ [a]
Declination (J2000)	-37° 09′ 16″.03 [a]
J [mag]	7.279 ± 0.026 [b]
H [mag]	6.587 ± 0.031 [b]
K_{s} [mag]	5.843 ± 0.020 [b]
Visual extinction A_V [mag]	0.3 [c]
Spectral type	F4Ve [d]
Luminosity	$7.8\ \mathrm{L}_{\odot}$ [c]
Mass	$1.7\ \mathrm{M}_{\odot}$ [e]
Radius	$1.4\ \mathrm{R}_{\odot}$ [e]
Temperature	6810 K [e]
Mass accretion rate	$(0.6 - 4.2) \cdot 10^{-8}\ \mathrm{M}_{\odot}/\mathrm{yr}$ [f]
Distance	140 ± 42 pc [g]
Age	8^{+8}_{-4} Myr [g]

[a] Hog et al. (1998); [b] Cutri et al. (2003); [c] Andrews et al. (2011); [d] Dunkin et al. (1997); [e] Müller et al. (2011); [f] Sitko et al. (2012); [g] van Boekel et al. (2005).

were 3240 and ~ 3232.9 s in H and K_{s} filters respectively and 270 s in each narrow band filter. No photometric standard was observed. Instead, we use the central star itself for photometric calibration. Observing conditions were photometric, with an excellent seeing (varying from 0.58″ to 1.01″), a good coherence time (from 28 to 46 ms), and an average airmass of 1.1. The angular resolution of the final images in H and K_{s} band ($\simeq$ 0.09″) is determined from the FWHM of the stellar unsaturated profile in the respective narrow band filter. Observing settings and conditions are summarized in Table 2.2.

2.3 NACO data reduction and Stokes parameters

The reduction of the NACO data analyzed here and in Chapter 3 was carried out with a self-written IDL routine. The procedure follows by large extent the method described by Avenhaus et al. (2014b). This section highlights the main steps of this technique and describe the nature of the final products of this data reduction.

The first cosmetic reduction was applied to the telescope exposures by correcting for dark current and flat field. We also performed a row-by-row subtraction of each exposure because of a non-static read-out noise pattern along the rows. Bad pixels were then substituted by the mean of the surrounding pixels.

Tab. 2.2 — Summary of observations. Columns are: filter name, detector integration time (DIT), number of integrations (NDIT) multiplied by integrations per dither position (NINT), number of dither positions, and average airmass, optical seeing, and coherence time. Note that DIT × NDIT × NINT × Dither Position gives the total integration time per position angle of the HWP.

Filter	DIT (s)	NDIT × NINT	Dither pos.	<Airmass>	<Seeing>	$<\tau_0>$ (ms)
NB 1.64	0.5	15×3	3	1.04	0.78″	35
H	0.5	90×6	3	1.03	0.78″	37
NB 2.17	0.5	15×3	3	1.08	0.75″	38
K_s	0.3454	130×6	3	1.12	0.70″	39

As mentioned in Sect. 1.3.3, the basic principle of the PDI observing mode is the simultaneous imaging of the linear polarization of the source along two orthogonal directions. With NACO, this is provided by a Wollaston prism which splits the incoming light into the so-called ordinary and extraordinary beams, offset by 3.5″ along the vertical direction of the detector. A polarimetric mask prevents the overlap of the two beams by alternating open and opaque stripes. The telescope frames thus contain both the ordinary and extraordinary beams, that must be extracted to allow their later combination. This extraction was done by firstly determining the center at sub-pixel accuracy through a two-dimensional gaussian to the point spread function (PSF) halo. For this procedure, values above the linearity regime of the sensor ($\sim 10,000$ counts) were dismissed. After that, both beams were extracted and all images upscaled by a factor 3 and aligned on top of each other.

With NACO, a rotatable half-wave plate (HWP) allows to control the orientation of the polarization. We thus obtain observations with 0°, 45°, 90°, and 135° inclined polarization states. This approach enables a thorough correction of pixel-to-pixel efficiency variations by means of the double ratio calculation (Tinbergen, 2005) of the Stokes polarimetry parameters. If we define $I_{\rm ord}$ and $I_{\rm ext}$ the ordinary and extraordinary beams extracted from the observations with the four polarization directions, the Q Stokes parameter is obtained from:

$$Q = \left(\sqrt{\frac{I_{\rm ord}^{0^\circ}/I_{\rm ext}^{0^\circ}}{I_{\rm ord}^{90^\circ}/I_{\rm ext}^{90^\circ}}} - 1\right) \Bigg/ \left(\sqrt{\frac{I_{\rm ord}^{0^\circ}/I_{\rm ext}^{0^\circ}}{I_{\rm ord}^{90^\circ}/I_{\rm ext}^{90^\circ}}} + 1\right) \times \left(\frac{I_{\rm ord}^{0^\circ} + I_{\rm ext}^{0^\circ} + I_{\rm ord}^{90^\circ} + I_{\rm ext}^{90^\circ}}{2}\right) \tag{2.1}$$

and the U parameter similarly from:

$$U = \left(\sqrt{\frac{I_{\rm ord}^{45^\circ}/I_{\rm ext}^{45^\circ}}{I_{\rm ord}^{135^\circ}/I_{\rm ext}^{135^\circ}}} - 1\right) \Bigg/ \left(\sqrt{\frac{I_{\rm ord}^{45^\circ}/I_{\rm ext}^{45^\circ}}{I_{\rm ord}^{135^\circ}/I_{\rm ext}^{135^\circ}}} + 1\right) \times \left(\frac{I_{\rm ord}^{45^\circ} + I_{\rm ext}^{45^\circ} + I_{\rm ord}^{135^\circ} + I_{\rm ext}^{135^\circ}}{2}\right) \tag{2.2}$$

Before obtaining from the Q and U parameters the science image, we had to correct

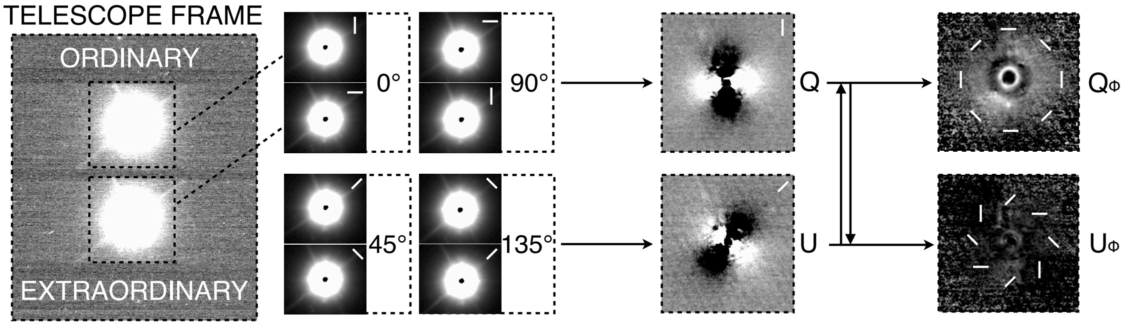

Fig. 2.1 — Sketch illustrating the procedure to obtain the Q_ϕ and U_ϕ parameters from a raw NACO frame. The polarization vector in each intermediate image is shown by the white bars.

for the significant instrumental polarization and crosstalk effects suffered by NACO (see Quanz et al., 2011; Witzel et al., 2010). To correct for the former, we assumed the stellar PSF to be largely unpolarized and thus we imposed the count ratio in ordinary / extraordinary beams to be unity. The crosstalk effect was corrected by artificially increasing the typically damped U parameter such that the number of pixels contained in an annulus around the star where $|Q| > |U|$ equals those where $|U| > |Q|$.

The traditional combination of the Q and U parameters is performed via $P = \sqrt{Q^2 + U^2}$. Nonetheless, we note that for centro-symmetric polarimetric patterns a more fruitful science image can be obtained with the tangential Stokes parameter Q_ϕ as from:

$$Q_\phi = +Q\cos(2\phi) + U\sin(2\phi) \tag{2.3}$$

where ϕ is the polar angle of a given position of the detector with respect to the position of the central star. For this computation, ϕ was corrected by an empirical -3.7° to account for a misalignment of the HWP rotation within the NACO instrument. Along with Q_ϕ, we calculated the Stokes U_ϕ defined as:

$$U_\phi = -Q\sin(2\phi) + U\cos(2\phi) \tag{2.4}$$

By construction, Q_ϕ and U_ϕ describe the polarization in the tangential direction and $\pm 45^\circ$ with respect to that, respectively. Q_ϕ is to be preferred to the traditional P because its computation does not imply the square of the Q and U parameters (and thus their noise). On the contrary, for purely tangential scattering the U_ϕ parameters might contain only noise. In fact, in this work we calculate the noise of the science image from the U_ϕ image. However, in mildly inclined systems deviations from centro-symmetric symmetry may occur dissuading from using this parameter as an estimate of the noise (see Sect. 4.3.2). A sketch summarizing this procedure is shown in Fig. 2.1.

The final step performed on the Q_ϕ and U_ϕ images thus obtained is the photometric calibration, which was carried out similarly to the approach described by Quanz et al. (2011). We estimate the total count rates of the source in H and K_s bands (for which the images show a saturated stellar profile) by means of the average of all images in *NB* 1.64 and *NB* 2.17 filters respectively, taking the different exposure time of the observations and transmission curve of the filters into account. Then, we convert the count rate in each pixel to surface brightness using the 2MASS magnitudes in H and K_s bands (see Table 2.1). This approach intrinsically assumes that the source has the same magnitude in H and K_s bands as in their respective narrow bands. However, the presence of a strong Brγ line from the star (Sitko et al., 2012) may introduce a bias in the calibration of the K_s band. Furthermore, the substantial near-IR variability of the source (30% in the K band, Sitko et al., 2012) is not taken into account. We estimate that this technique provides an absolute flux calibration only good to 50%.

2.4 Results

Figure 2.2 shows the final Q_ϕ and U_ϕ images in the H and K_s band. Strong signal is clearly detected in both Q_ϕ images but not in the U_ϕ images. According to the construction of these parameters (see Sect. 2.3), this is indicative of light which is scattered in a tangentially-symmetric way. The images in the K_s band are higher-quality because of a better AO correction. Both U_ϕ images reveal partially uncorrected diffraction spikes and read-out noise pattern. These artifacts are also present in the Q_ϕ images.

The Q_ϕ images reveal signal from $\sim 0.1''$ to $\sim 0.9''$ ($\sim 14 - 130$ AU) in both H and K_s band. They show three main peculiarities: (*i*) an inner region (inside $0.15'' - 0.18''$) with scattered light depleted down to a few percent of a theoretical continuous distribution (the *cavity*); (*ii*) a bright quasi-circular rim at $\sim 0.2''$ (the *ring*); (*iii*) two elongated non-axisymmetric spiral arms extending from the ring to $\sim 0.5''$ and covering an azimuthal angle of $\sim 180°$ each (*S1* being that in the W and *S2* that in the E, following Muto et al. 2012). The total intensity of polarized light integrated between $0.1''$ and $0.9''$ is 11.7 mJy ± 50% in H band and 4.3 mJy ± 50% in K_s band.

In the following, we analyze the polarized brightness distribution of the images, starting from the disk outside the ring and then moving to the inner $0.2''$, namely the region that our images resolved in scattered light for the first time.

2.4.1 The brightness distribution: $r > 0.2''$

The radial polarized brightness is complex and azimuth-dependent because of the presence of spiral arms. Top and middle panels of Fig. 2.3 shows the radial profile obtained with 3-pixel wide cuts along the major axis (PA=56°, Lyo et al., 2011) and the minor axis (see orange and pink stripes in Fig. 2.2). The relative errors are obtained from the noise estimated from the U_ϕ images but do not consider any systematic uncertainty from the absolute flux calibration. No significant difference in the brightness profile is found

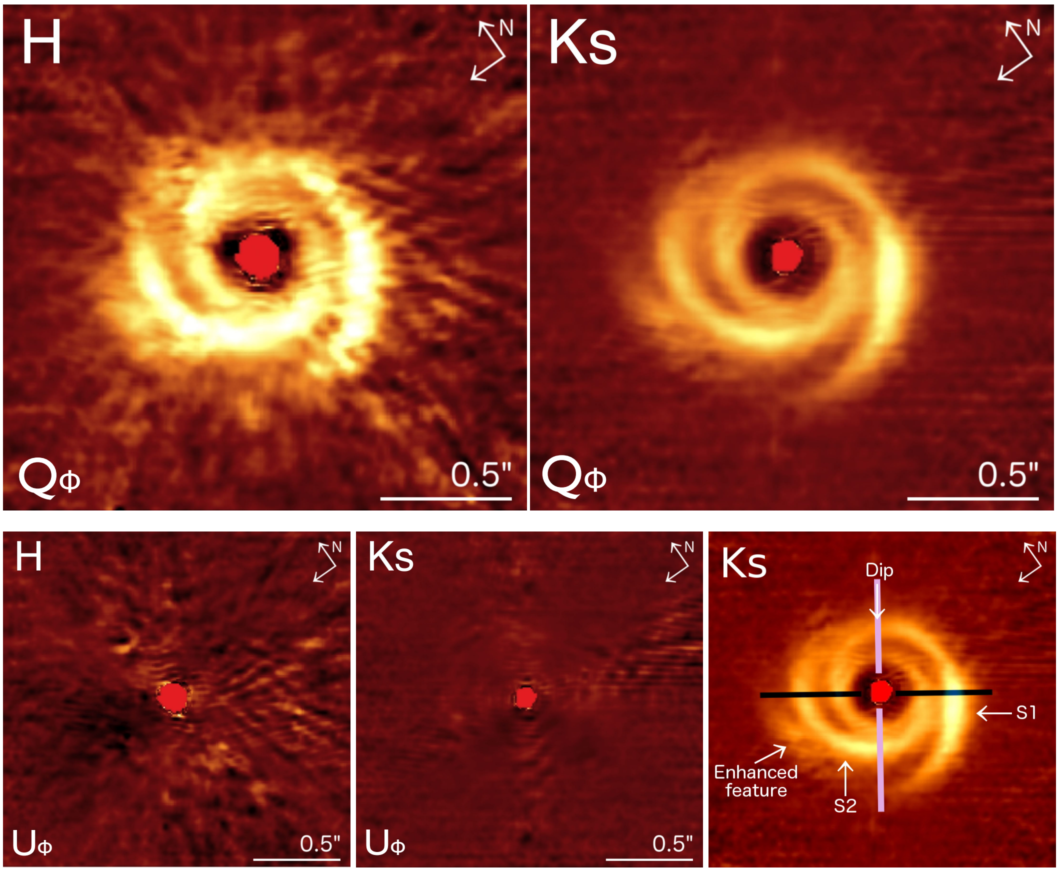

Fig. 2.2 — VLT/NACO imagery of SAO 206462. Top row: Q_ϕ images in the H and K_S band. Bottom row: U_ϕ images in the H and K_S band, as well as the labeled version of the Q_ϕ image, with blue and pink stripes indicating the position of the major and minor axis, respectively. Images are scaled with r^2 to compensate for stellar light dilution. The color scale is linear and arbitrary. The central masked-out region indicates non-linear pixels.

between the H and the K_s band (apart from the polarized flux being a factor $2.5-3$ higher in the former than that in the latter).

We averaged the radial profiles over all angular directions neglecting any geometrical effect due to the disk inclination. Since the disk is known to be almost face-on (11°, Andrews et al., 2011), we assume that this approach does not introduce large systematic errors. The azimuthally-averaged profile of both bands is fitted by a power-law with $\beta = -2.9 \pm 0.1$. However, we find that a spatially separate fit with a broken power-law provides a better match. A slope of -1.9 ± 0.1 is found for the range $0.2'' - 0.4''$ ($\sim 28-56$ AU) and a slope of -5.7 ± 0.1 (H band) and -6.3 ± 0.1 (K_s band) for the range $0.4'' - 0.8''$ ($\sim 56-114$ AU) (see bottom left panel of Fig. 2.3). Nonetheless, we stress that these estimates should be trusted with caution because PSF smearing can significantly affect PDI observations by dampening the observed flux by up to one of order of magnitude in the inner $0.5''$ (Avenhaus et al., 2014a).

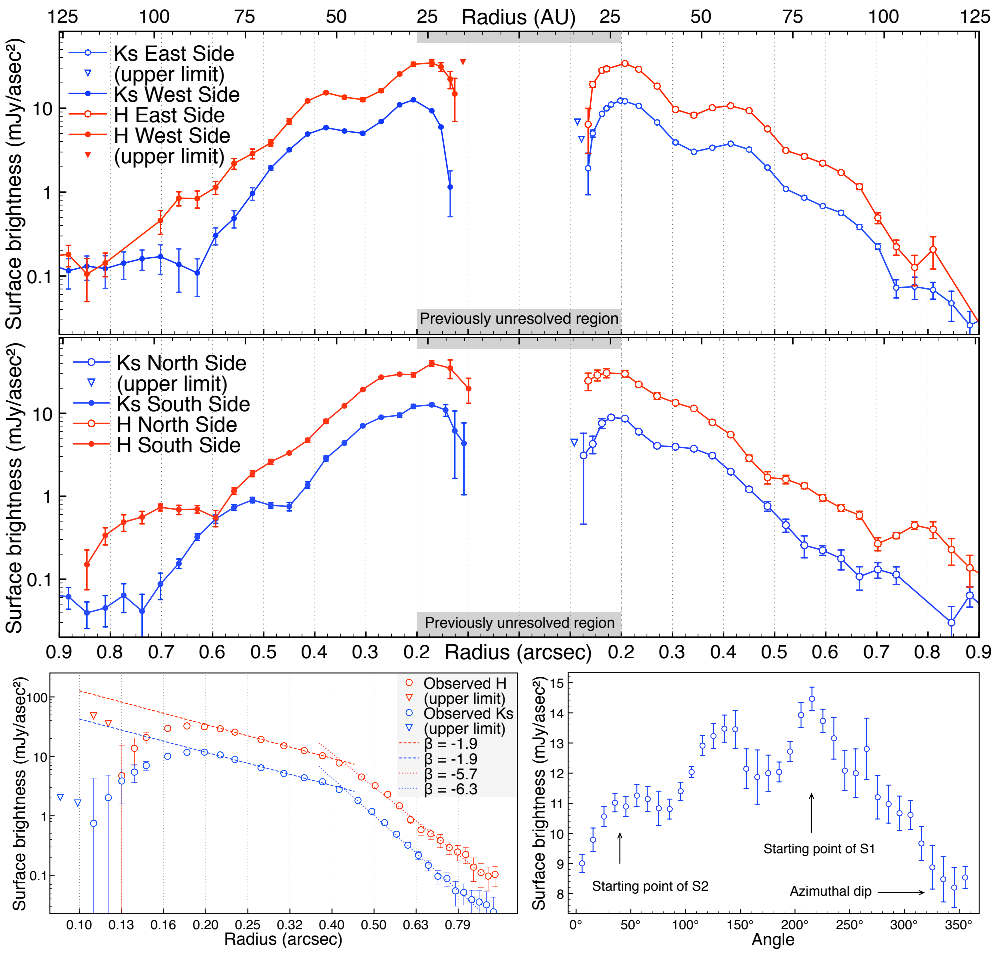

Fig. 2.3 — Brightness profile of SAO 206462. Top panel: radial profile along the major axis to NE (right half) and to SW (left half) in the *H* (red) and in the K_s band (blue). Middle panel: radial profile along the minor axis to NW (right half) and to SE (left half), namely the far and near disk side, respectively. The grey box indicates the region that our data resolved for the first time. In all profiles (except the *H* band NW minor axis), the depletion inside this region is evident. Bottom left panel: azimuthally-averaged radial profiles and power-law best fits for $0.2'' < r < 0.4''$ (dashed lines) and for $0.4'' < r < 0.8''$ (dotted lines). Bottom right panel: azimuthal profile along the ring in the K_s band, averaged over the $0.17'' - 0.21''$ radii. Two main bumps are visible. One is associated to the starting point of S1. Errors are 3σ noise calculated from the U_ϕ images and do not include systematic uncertainties in the photometric calibration.

The two spirals are starting from axisymmetric locations on the rim. The contrast of the spiral with the surrounding disk varies from 1.5 to 3.0. S1 appears as the most prominent arm. It covers an angle of ~ 240° and shows an enhancement to the SW (almost twice as luminous in surface brightness as the contiguous part of the arm). S2 covers a smaller angle (~ 160°) but also shows a "knot" (to the SE, factor 1.5 brighter in surface brightness than the contiguous part of the arm).

From our images, we resolve a narrow dip in the emission along the radial direction at a position angle of 340°. This feature is very clear on the ring but can be traced out to

$0.5''$ in both bands. A slight deficit can be observed on a larger scale (~ 90°) in the NW. A diffuse enhanced emission is also visible in Fig. 2.2 to the east side. This feature can be traced in both bands from the outer edge of S2 to $\sim 0.7''$, covering an angle of ~ 30°.

2.4.2 The brightness distribution: $r < 0.2''$

As shown in Fig. 2.3, the polarized flux decreases inward of $0.15'' - 0.18''$ in both bands. At $0.12''$ from the star, the surface brightness is 6% of a continuous flux distribution (as extrapolated from the power-law fit) in H band and 14% in K_s band, decreasing to 2% in the innermost region traced by our observations ($0.10''$). These depletion factors are by far larger than the 3σ error, as shown in the azimuthally-averaged radial profile of Fig. 2.3, and therefore significant.

At the outer edge of the cavity, a quasi-circular ring-like structure is present in both bands. The width of the ring ($\sim 0.09''$) is comparable with the angular resolution of the observations, suggesting that the structure is not resolved. The radial location of the brightest part of the ring varies with the azimuthal angle from $0.19''$ to $0.21''$. This amount of ellipticity is what is expected from the geometrical projection on the sky (considering $i \sim 10° - 20°$). Therefore, we do not infer any intrinsic eccentricity for the ring.

In the bottom right panel of Fig. 2.3 we show the azimuthal profile of the ring in K_s band, obtained averaging concentric annuli from $0.17''$ to $0.21''$. Besides the azimuthal dip ubiquitous along the far minor axis, we identify two features (bumps at PA ~ 220° and ~ 135°). The former is directly associated to S1, since it overlaps with the starting-point of the arm.

2.5 Discussion

Since the Q_ϕ parameter traces, by construction, the light which is scattered in a tangentially-symmetric way, the signal detected in those images are stellar radiation scattered by the circumstellar disk. The absence of detected emission from the U_ϕ images supports the idea that no significant deviations from centro-symmetric scattering are to be expected from face-on disks.

In this section, we interpret the results presented in Sect. 2.4. In particular, In Sect. 2.5.1 we interpret the features observed in the outer part of the disk and compare them with other works. In Sect. 2.5.2, we focus on the inner cavity and discuss a possible scenario for the origin of the observed features. Finally, in Sect. 2.5.3 we speculate on the mechanisms responsible for the inner cavity and the spiral arms and estimate mass and location of the companion potentially sculpting the inner disk.

2.5.1 Spirals and dust accumulation

SAO 206462 was detected in scattered light with HST/NICMOS at 1.1 and 1.6 μm by Grady et al. (2009) and, later, in polarized light with Subaru/HiCIAO in H band by Muto et al. (2012). The latter were the first to resolve the spiral structure. The outer extent inferred by our observations ($0.9''$) is in good agreement with their estimate. The azimuthally averaged radial profile fitting our observations (power-law with $\beta = -2.9$) is in the range of typically observed values for Herbig stars, both in scattered light (e.g. Grady et al., 2007) and polarized light (e.g. Quanz et al., 2011). The value is in agreement with what was inferred for SAO 206462 by Muto et al. (2012, r^{-3} as a representative average). The total polarized light intensity measured in the H band (11.7 mJy) is a factor 1.15 higher than the measurement by Muto et al. (2012) but the results agree within the error bars. Furthermore, a small part ($\sim$ 10%) of the total intensity is from the inner region ($< 0.2''$) that is masked in the images by Muto et al. (2012), reinforcing the agreement. Finally, the total polarized light intensity in K_s band (4.3 mJy) was never measured before.

The brightness deficit in the NW was also observed by Muto et al. (2012). The same deficit was observed in scattered light by Grady et al. (2009) at 1.1 μm. Curiously, they did not resolve it at 1.6 μm, whereas our H band image (of polarized light) does. Lyo et al. (2011) inferred from CO observations that the SW side is receding. Spirals are typically trailing and, thus, as remarked by Muto et al. (2012), the region of the deficit may represent the far side of the disk. In particular, the dip in polarized light at 340° is roughly coincident with the minor axis (326°). Given this, the narrow dip and the general deficit can be ascribed to depolarization. Since the degree of linear polarization is maximized at $\sim$ 90° scattering angle (e.g. Draine, 2003; Min et al., 2012), polarized images of inclined disks are indeed expected to show minima along the near and far side of the disk (see case of MWC480, Kusakabe et al., 2012). However, no deficit is observed on the near side. This might indicate that dust grains preferentially forward-scatter the radiation, thus compensating for the depolarization effect.

The spiral arms are by far the most tantalizing feature of the disk. Spiral arms have been observed in a few other protoplanetary disks. Among them, we point out AB Aur (Hashimoto et al., 2011), HD 100546 (Grady et al., 2001), HD 142527 (Avenhaus et al., 2014b; Casassus et al., 2012), MWC 758 (Benisty et al., 2015; Grady et al., 2013), HD 100453 (Wagner et al., 2015). Since only very recent techniques are capable of resolving these structures, it is difficult to infer how common spiral arms are among protoplanetary disks. Because PDI observations trace the stellar radiation which is scattered by a thin surface layer of the disk, the spiral arms detected with this technique can either constitute intrinsic changes of the disk grain properties or small local variations of the disk geometry, which modify the incidence angle of the photons. In particular, small ripples in the disk scale height may be sufficient to explain the light contrast shown by the spirals around SAO 206462 with the contiguous disk (a factor 1.5 to 3.0). This possibility is discussed in more detail in Sect. 4.4.3.

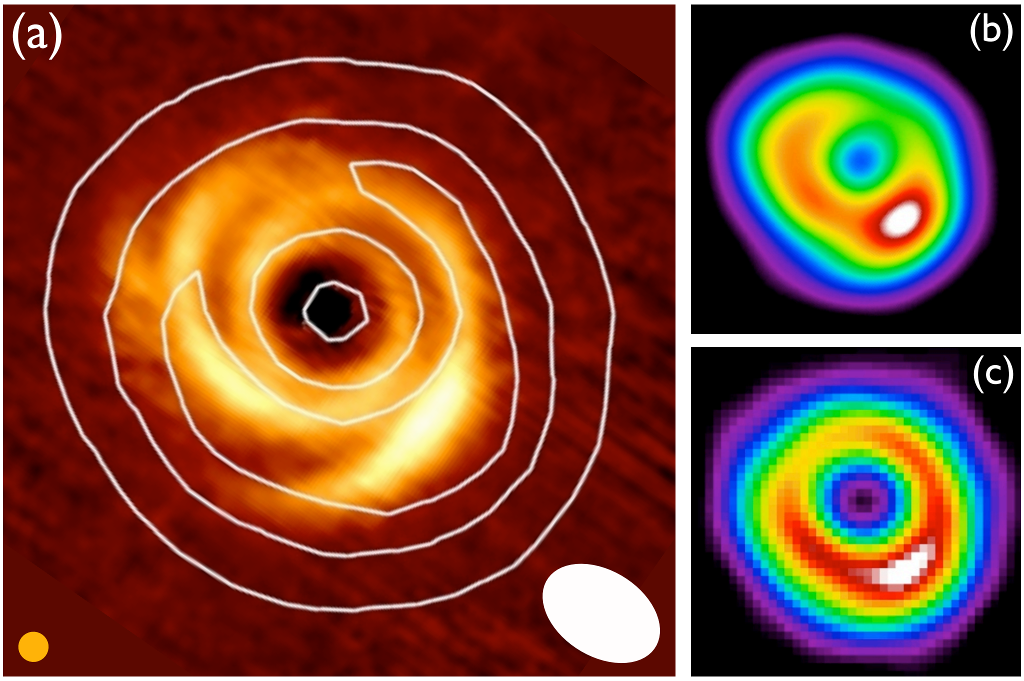

Fig. 2.4 — K_S band scattered light image of SAO 206462 from this work compared to the ALMA observations at 450 μm from Pérez et al. (2014). **(a)**: ALMA image (contours) superimposed on the NACO image. The angular resolution of our scattered light images (orange) and of the ALMA data (white) is shown at the lower corners. **(b)**: NACO image convolved with the ALMA angular resolution ($\sim 0.25''$). **(c)**: ALMA image.

In a scenario where spirals in scattered light are only surface wiggles, disk imaging at millimeter wavelengths might not resolve such structures. To date, no millimeter image of SAO206462 with enough angular resolution to resolve the spirals has been released. In any case, the horseshoe structure revealed from thermal images by Brown et al. (2009) and Lyo et al. (2011) has a possible connection with the polarized light. More recent ALMA images (Pérez et al., 2014) (with resolution as good as $0.25''$) make this analogy more clear (see Fig. 2.4). Pérez et al. (2014) claimed that the morphology of the ALMA images could be the result of a vortex-like asymmetry (see Sect. 1.2.2) combined with an unresolved spiral structure. This possibility is sustained by the similarity between the ALMA image and our NACO image convolved with the ALMA resolution (Fig. 2.4b-c).

2.5.2 Dust grains at the cavity edge

The inner region ($r < 0.2''$) of the disk was never resolved before in scattered light. We interpret the drop in surface brightness inside $0.15'' - 0.18''$ as a real depletion of small dust grains. In the following, we refer to the region showing this depletion as the cavity. This definition is meant to indicate a region showing an abrupt discontinuity in the dust radial profile but does not imply that this region is completely void of dust. The ring revealed at the outer edge of the cavity represents the most luminous region of the disk and we interpret it as the inner wall of the outer disk which is directly illuminated by the central star. Thus, we infer the outer edge of the cavity from the (unresolved) ring radial profile along the major axis. We find that the cavity extends from the instrumental inner working angle (~ 14 AU) to 28 ± 6 AU. This cavity edge is in good agreement with what was inferred by Maaskant et al. (2013) with Q-band (24.5 μm) imaging (30 AU).

Interestingly, the outer edge of the observed cavity considerably differs from that predicted by SED fitting (R = 45 AU, Brown et al., 2007) and that imaged at (sub-)millimeter (R = 39 AU to 50 AU, Andrews et al., 2011; Brown et al., 2009; Lyo et al., 2011; Pérez et al., 2014). Even though the angular resolution of (sub-)millimeter observations is (still) coarser than that of our PDI images, this discrepancy cannot be explained by observational effects. In fact, downgrading the resolution of our images acts to fill in the gap, thus raising the difference between the datasets. Discrepancies between thermal and polarized light were already noticed by Muto et al. (2012). However, they found no evidence of discontinuity at radii as small as 28 AU.

The size of the cavity of many transition disks has been inferred from sub-millimeter observations (see e.g. Andrews et al., 2011). However, the presence of small dust grains well inside millimeter-grains cavities has been inferred by means of PDI observations (e.g. SR21; UX Tau A, Follette et al., 2013; Tanii et al., 2012) and modeling of multi-wavelength observations (e.g. HH 30, Madlener et al., 2012). Since PDI and thermal images trace different components of the dust (μm-sized grains in the scattered light images, mm-sized grains in the thermal images), this discrepancy can provide important information on the dust distribution in the inner regions.

Rice et al. (2006) have shown that, at the outer edge of a disk gap cleared by a planet, a local pressure bump can act as a filter, allowing small ($\lesssim 10\ \mu$m-sized) particles to drift inward but holding back larger grains. In order for the SED to show the near- to mid-IR dip typical of transition disks, the region inside the cavity must contain optically thin dust. However, Zhu et al. (2012) argued that dust filtration alone cannot explain the observed spectral deficit (invoking additional processes such as dust growth). Dong et al. (2012) put the three observational evidence together (spectral deficit, cavity in sub-mm images, and continuous radial distribution of polarized light) and proposed a model with dust filtration and flat or inward-decreasing surface density profile inside the cavity (consistent with dust growth).

Nevertheless, our observations replace, for the particular case of SAO 206462, one element: the small dust grains are not continuously distributed down to the sublimation radius but show an abrupt discontinuity. Since the location of the observed discontinuity ($0.15''$) is comparable with the typical inner working angles of PDI ($0.1'' - 0.2''$), we argue that the case of SAO 206462 may not be unique. In fact, later works have shown a similar morphology in other transition disks, such as HD100546 (Wright et al., 2015), Sz91 (Tsukagoshi et al., 2014), and IRS48 (Follette et al., 2015).

The depletion of small dust grains inside the millimeter cavity represents a direct, qualitative explanation for the spectral deficit, without necessarily invoking simultaneous dust growth inside the cavity. However, the origin of such a depletion is uncertain. Dust filtration permits the presence of small grains inside the edge observed at millimeter wavelengths but cannot explain why these grains are held back at a different, inner location. A possible explanation invokes the gas distribution inside the cavity. Pinilla et al. (2012) have shown that the outer edge of the gaseous halo carved out by a planet may not coincide with the location of the pressure bump generated by the same planet. They show how the pile-up of the dust occurs, depending on the planet mass, at radii 1.4 to 2.0 times farther from the planet than the gap outer edge in the gas. Only particles larger than a certain minimum size (typically at sub- to millimeter scale at distances of $20-50$ AU) are perfectly trapped in the pressure maximum. We expect that the small (μm-size) particles at $R \sim 40$ AU are perfectly coupled to the gas and can, thus, be dragged along with it. To show this, we calculate the Stokes number St, defined as:

$$\mathrm{St}(a,R) = \frac{\rho_{\mathrm{S}}(R)\cdot a}{\Sigma_{\mathrm{g}}(R)}\cdot\frac{\pi}{2} \tag{2.5}$$

(Birnstiel et al., 2010) where a is the particle size, ρ_{S} the solid density of dust particles, and Σ_{g} the gas column density. We calculate St for μm-size particles located at $R = 40$ AU using a typical $\rho_{\mathrm{S}} = 1$ g/cm^3 and Σ_{g} as constrained for this disk by Andrews et al. (2011):

$$\Sigma_{\mathrm{g}}(R) = 22\left(\frac{R}{55\,\mathrm{AU}}\right)^{-1}\cdot\exp\left(-\frac{R}{55\,\mathrm{AU}}\right)\ \mathrm{g/cm^2} \tag{2.6}$$

We find that $\mathrm{St}(a = 1\ \mu\mathrm{m},\ R = 40\ \mathrm{AU}) \simeq 10^{-5}$. Since strong interplay with the gas is expected for particles with $\mathrm{St} \ll 1$, this result suggests that μm-size dust grains at the cavity edge of mm-size grains are very well coupled to the gas.

In a scenario where a planet is carving out the disk (see Sect. 2.5.3), the observed inner cavity of μm-size dust grains at 28 AU might coincide with the outer edge of the gaseous cavity, whereas the mm-size particles are piled-up at the pressure bump located at 39 AU. However, the inner region is not void of gas, as inferred from the presence of CO ro-vibrational lines as far as 25 AU (considering $d = 142$ pc, Carmona et al., 2014; Pontoppidan et al., 2008). This may not appear as a contradiction of the proposed scenario if we assume that the gas is carved out in a narrow ring (consistently with the presence of a single planet) because CO line profile fitting may not reveal such a fine structure. The observed depletion (one order of magnitude) of CO gas in the central region of the disk (Lyo et al., 2011; van der Marel et al., 2015) might also support a scenario where the gas is partially cleared. In fact, the tidal action of a planet is also expected to significantly deplete material in the region inside the location of the planet (Tatulli et al., 2011). Furthermore, the presence of gas and small dust grains inside the cavity is required to explain the inner dust belt and the substantial accretion rate of the source.

2.5.3 Disk interaction with unseen planets?

Spiral arms and large inner cavities are among the most intriguing features observed in protoplanetary disks. These two features (both shown by the dusty disk around SAO 206462) can provide insight into the dynamical processes occurring in the disk.

Inner cavity. One possible process responsible for the clearing of a large inner region of disks is the interaction with orbiting companion(s) (e.g. Rice et al., 2003). Dodson-Robinson & Salyk (2011) have shown with hydrodynamical simulations that a multiple planets system is required to open holes as large as the millimeter observations suggest. However, Pinilla et al. (2012) also considered modeling of dust evolution demonstrating that the gap carved out by a single planet can be much larger than expected by means of pure gas hydrodynamical simulations. Photoevaporation can also generate disk inner holes. Alexander & Armitage (2007) argued that UV photoevaporation can induce holes only in systems with accretion rates $\lesssim 10^{-10}$ $M_\odot$ yr^{-1}. Thus, the substantial accretion rate shown by SAO 206462 (a few 10^{-8} $M_\odot$/yr, Sitko et al., 2012) rules out this possibility. Dust grain growth has also been proposed to explain the observed cavities (Dullemond & Dominik, 2005). However, this process is expected to produce smooth radial profiles, inconsistent with our PDI observations. Furthermore, the growth of μm-size particles should give rise to a family of mm-size grains, which is not observed at (sub-)mm wavelengths (Brown et al., 2009; Lyo et al., 2011). Birnstiel et al. (2012) showed indeed that large cavities cannot be caused by grain growth alone. Finally, the role of magnetorotational instability (MRI) in disk clearing has been discussed by Chiang & Murray-Clay (2007). However, Dominik & Dullemond (2011) argued that the dust grains cannot be held back by radiation pressure alone. In addition, the presence of a thick dust belt close to the star (Fedele et al., 2008) rules out any mechanism operating with inside-outside modality (namely, the photoevaporation and the MRI instability).

Spirals. Disk−planet interaction can result in spiral density waves (e.g. Tanaka et al., 2002) and possibly generate both a disk gap and a spiral arm structure (Crida et al., 2006). Alternatively, gravitational instability has been proposed as mechanism of spiral wave excitation in disks (e.g. Durisen et al., 2007). Disks are considered gravitationally unstable at a certain radius r if the Toomre parameter $Q(r) \lesssim 1$. To speculate about the stability of the disk around SAO 206462, we use a global Q as calculated by Kamp et al. (2011):

$$Q = \sqrt{\frac{8k}{\mu m_{\mathrm{H}} G}} \sqrt{\frac{\sqrt{R_*} T_* M_*}{M_{\mathrm{disk}}^2 (2-\epsilon)^2}} R_{\mathrm{in}}^{1/4} \left(\left(\frac{R_{\mathrm{out}}}{R_{\mathrm{in}}} \right)^{(2-\epsilon)} - 1 \right) \left(\frac{R_{\mathrm{out}}}{R_{\mathrm{in}}} \right)^{(\epsilon-7/4)} \tag{2.7}$$

We use the stellar radius R_*, temperature T_*, and mass M_* assumed by Müller et al. (2011), a disk mass M_{disk} of 0.026 $M_\odot$ (Andrews et al., 2011), disk outer radius R_{out} of 220 AU (Lyo et al., 2011), and inner radius R_{in} from this dataset. We vary the column density power-law ϵ over a range of realistic values (0.5 to 1.5, Kamp et al., 2011). We find that Q always exceeds 25, meaning that the disk is (globally) highly stable. To enter the unstable regime, the disk would have to be more than twenty times more massive.

However, the degree of instability necessary to generate small wiggles on the disk surface (see Sect. 2.5.1) may be lower than what is usually assumed as an edge of the two regimes. Finally, formation of spiral arms is expected in disks around binary stars because of strong tidal forces (e.g. Boss, 2006). The physical separation between SAO 206462 and its visual companion HD135344A is at least 2900 AU. In the case of highly eccentric orbits ($e = 0.9$) and face-on orbital plane, the semi-minor axis of this potential binary system can be as small as $\sim$ 150 AU. Duchêne (2010) showed that binaries wider than 100 AU are indistinguishable from single stars in terms of their circumstellar disks and planetary systems. Nevertheless, we cannot rule out a marginal gravitational interaction between the two stars. This study is beyond the scope of the current work.

It turns out that the interaction with an orbiting companion is the only process capable of explaining both the inner disk clearing and the spiral arms structure. Any other known mechanism cannot account for at least one observational evidence. However, we cannot claim that a potential companion responsible for the inner clearing is also responsible for the spiral excitation. In fact, Muto et al. (2012) and Grady et al. (2013) estimated the location of the possible planet exciting spiral arms (of SAO 206462 and MWC 758, respectively) to be outside of the spirals themselves. Grady et al. (2013) argued that such a planet could not account for the cavity observed around MWC 758. A deeper discussion on the morphology of spirals excited by planets is given in Sect. 4.4.3.

In the intriguing prospect that a single object is responsible for the observed large inner hole, we constrain the location and the mass that such a companion should have. We use the results by Dodson-Robinson & Salyk (2011) and Pinilla et al. (2012) to determine a testable range of realistic locations for that object and, then, infer its mass.

The gap width in the disk is regulated by the tidal radius, or Hill radius, of the companion, defined as:

$$R_H = r_p \left(\frac{M_p}{3M_*} \right)^{1/3} \tag{2.8}$$

being r_p and M_p the planet location and mass and M_* the stellar mass. Dodson-Robinson & Salyk (2011) showed that tidal interactions with planets are very fast at scattering disk particles within $\sim 3\ \mathrm{R_H}$ ($\lesssim 10^4$ yr) while the scattering timescale for particles at $\sim 5\ \mathrm{R_H}$ approaches 1 Myr. These results argue against the single planet carving out the gap, because of the inability of reproducing the hole sizes observed at millimeter wavelengths. However, Pinilla et al. (2012) predicted that the accumulation of large dust grains can occur at radii 1.4 to 2.0 larger than the outer edge of the gaseous gap (i.e. ~ 7 to $\sim 10\ \mathrm{R_H}$).

Inspired by this statement, we use the speculated outer edge of the gas cavity (R = 28 AU, as inferred from our observations of the small dust grains), and impose it to be the outer edge of a gap with size (i.e. distance planet−edge) of $\kappa_{\mathrm{gas}} = 3$ to 5 times $\mathrm{R_H}$. Moreover, we use the observed cavity dimension for mm-size dust particles (R = 39 AU, from Brown et al., 2009) and impose it to be the outer edge of a gap of $\kappa_{\mathrm{dust}} = 7$ to 10 $\mathrm{R_H}$ (depending, in turn, on the mass planet, see Pinilla et al., 2012). By varying κ_{gas} and κ_{dust} over a discrete range of values, we find a family of solutions. A potential companion

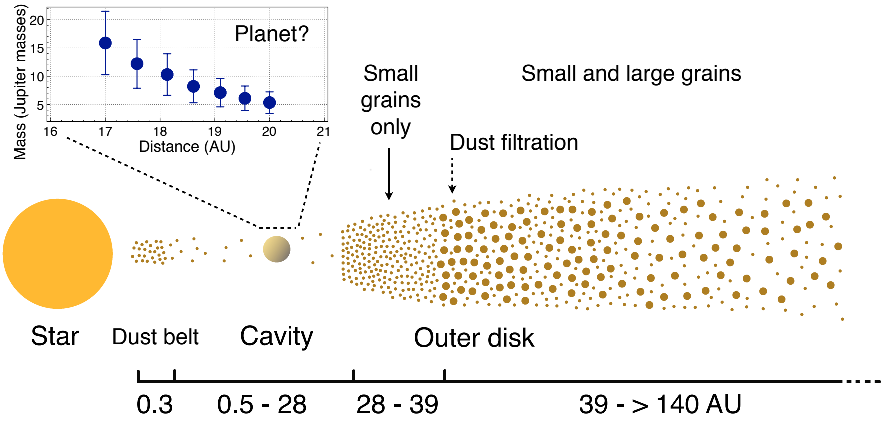

Fig. 2.5 — Illustrative sketch showing the dust radial distribution in the disk around SAO 206462, as proposed in this work according to data from this paper, Fedele et al. (2008), and Brown et al. (2009). Locations and masses of a potential single companion responsible for the observed inner cavity in the disk are drawn in the inset plot. Errors are obtained from the uncertainties in the location of the observed cavity edges (from this work and Brown et al., 2009).

responsible for the observed geometry should be located at a radius spanning from 17 to 20 AU with a mass between 5 and 15 M_J, being, thus, a giant planet (see inset plot in Fig. 2.5). These companion masses are not in contradiction with the upper mass limit inferred by Vicente et al. (2011) with VLT/NACO narrow-band imaging ($\sim$ 230 M_J at 14 AU).

In a scenario with a 5 to 15 M_J giant planet, the gravitational torque is much larger than the viscous torque and, thus, the radial location of the trapping is not significantly affected by the disk viscosity (considering typical α parameters of $10^{-4} - 10^{-2}$, Pinilla et al., 2012). Finally, we argue that the estimate of this section is valid only on the assumption that a single planet is capable of clearing the observed cavity. We did not explore the scenario of multiple planets. However, such a system seems in contradiction with the presence of diffuse gas inside the cavity (see Sect. 2.5.2).

2.6 Summary and conclusions

The F4 young star SAO 206462 (HD135344B) is known to host a transition disk that shows a narrow dust inner belt (Fedele et al., 2008), a large dust cavity at millimeter wavelengths ($\sim$ 39 AU, Brown et al., 2009), and a prominent spiral arms structure (Muto et al., 2012). No cavity was revealed at near-IR wavelengths down to $\sim$ 28 AU (Muto et al., 2012). This discrepancy was highlighted for a number of other objects (e.g. Follette et al., 2013; Tanii et al., 2012). To explain both this property and the observed spectral deficit at near-IR wavelengths, a scenario with dust filtration and grain growth inside the cavity was proposed (Dong et al., 2012).

In this work, we have presented PDI observations of SAO 206462 obtained with VLT/NACO and tracing the polarized light from the disk as down as $0.1''$. The main results from our PDI observations are summarized as follows:

- The disk is detected in polarized light out to ~ 130 AU in both H and K_s band. No particular difference is found between the two bands. The azimuthally-averaged polarized brightness profile is fitted by a power-law with $\beta = -2.9$. However, a broken power-law ($\beta = -1.9$ fitting the inner ~ 60 AU, $\beta = -6.0$ fitting outside) provides a better fit.
- The images reveal the double spiral arms resolved by Muto et al. (2012), a general dip along the axis at $\theta = 325°$ (due to depolarization), and a diffuse enhancement of unclear origin to the east side.
- We resolve an inner cavity (brightness down to 2% of a continuous distribution) surrounded by a non-resolved bright rim located at 28 ± 6 AU. The rim does not show signs of eccentricity but the azimuthal brightness profile reveals two small bumps, one of which is associated to a spiral arm.

The presence of an inner cavity for μm-size dust grains constitutes a qualitative explanation for the observed spectral deficit at near-IR wavelengths. Furthermore, a scenario with small particles continuously distributed in the inner disk and subject to intense growth is ruled out. However, the large difference between the cavity size of small ($R \sim 28$ AU) and large ($R \sim 39$ AU) dust grains draws attention to some tantalizing aspects. This cavity is likely to be produced by tidal interaction with one or more companions. In particular, any other known mechanism (photoevaporation, dust grain growth, and MRI) contradicts at least one observational piece of evidence (i.e. high accretion rate, inner dust belt, abrupt radial profile at the cavity edge).

The scenario with planet(s) carving out the cavity also provides an explanation for the observed diversity of small and large grain distribution. Pinilla et al. (2012) suggested that the pressure bump induced by an orbiting planet (and trapping large particles only) can be located at radii much larger than the outer edge of the gaseous cavity opened by the same planet. Inspired by this model, we propose a scenario where one giant planet is responsible for holding millimeter-size particles at 39 AU but permits μm-size grains, perfectly coupled to the gas, to move inward down to 28 AU, where the gas itself is retained by the planet. The presence of gas inside the cavity (Pontoppidan et al., 2008) seems to suggest that this is carved out in a narrow ring, rather than in the entire cavity. In any case, the suggested scenario implies a depletion of gas in the inner few tens of AU, in agreement with the observations by Lyo et al. (2011). In particular, we analytically calculate that all observations are consistent with a potential planet located at 17 – 20 AU with mass 5 – 15 M_J carving out the cavity. A multiple-planet system is not ruled out by our observations but appears as a contradiction to the presence of diffuse gas inside the cavity.

Pulvis et umbra sumus
(We are but dust and shadow)

HORACE, *"Carminvm IV", 13 BC*

3

Shadows, cavities, and snow-lines

HD163296, HD141569A, HD150193A with VLT/NACO

Based on a paper published in
Astronomy & Astrophysics, 568, A40 (2014)

A. Garufi[1], S.P. Quanz[1], H.M. Schmid[1], H. Avenhaus[1], E. Buenzli[2], S. Wolf[3]

Received 23 May 2014 / Accepted 24 June 2014

---

[1] Institute for Astronomy, ETH Zurich, Wolfgang-Pauli-Strasse 27, CH-8093 Zurich, Switzerland
[2] Max-Planck Institute for Astronomy, Königstuhl 17, D-69117, Heidelberg, Germany
[3] University of Kiel, Institute of Theoretical Physics and Astrophysics, Leibnizstrasse 15, 24098 Kiel, Germany

Abstract

We enlarge the sample of protoplanetary disks imaged in polarized light with high-resolution imaging by observing the Herbig Ae/Be stars HD163296, HD141569A, and HD150193A. We combine our data with previous datasets to understand the larger context of their morphology. We report a weak detection of the disk around HD163296 in the H and K_S band. The disk is resolved as a broken ring structure with a significant surface brightness drop inward of 0.6″. No sign of extended polarized emission is detected from the disk around HD141569A and HD150193A. We propose that the absence of scattered light in the inner 0.6″ around HD163296 and the non-detection of the disk around HD150193A may be due to similar geometric factors. Since these disks are known to be flat or only moderately flared, self-shadowing by the disk inner wall might play an important role. We show that the polarized brightness of a number of disks is indeed related to their flaring angle. Furthermore, we discuss the possible connection between the marginal detection in HD163296 and the snow-line in its disk. On the other hand, the non-detection of HD141569A is consistent with previous datasets that revealed a huge cavity in the dusty disk.

3.1 Introduction

As discussed in Sect. 1.3.3, scattered light images of inclined circumstellar disks are expected to show azimuthal asymmetries due to anisotropic scattering by the dust grains. These anisotropies depend on the grain properties. The scattering function for larger grains is indeed more forward-peaking (e.g., Mulders et al., 2013a). The amount of this is difficult to retrieve, however. On top of this effect, scatterers polarize the light by a fraction that depends on the nature of the scattering particles (e.g., composition, compactness) and on the scattering angle. In PDI images, these two effects are not easy to distinguish if complementary scattered light images are unavailable.

In addition to the dust grain properties, the global disk geometry can also considerably influence scattered light observations. Flared geometries have been invoked to explain the high far-IR excess in the spectral energy distribution (SED) of young stars. As commented in Sect. 1.3.1, Herbig Ae/Be disks are typically classified into flared (group I) and flat (group II) objects, based upon the shape of their IR excess (Meeus et al., 2001). The disk scale height can also affect the amount of light that is scattered by the disk surface.

The geometry of the inner few AU of disks can also play an important role for scattered light images. In fact, the inner wall can intercept a significant fraction of the stellar radiation and cast a shadow on the outer disk (e.g., Dullemond et al., 2001). The scale height of these walls is known to be variable, as suggested by the typically observed erratic near-IR magnitudes. An anticorrelation between the near-IR and the far-IR excess has been found in some objects (e.g., Espaillat et al., 2011), which supports this scenario.

In this chapter, we analyze the PDI observations of HD163296, HD141569A, and HD150193A obtained with VLT/NACO in 2012 and published by Garufi et al. (2014b). Furthermore, we anticipate some results from a recent NACO survey of Group II objects which are pertinent to the science case of this chapter. The final analysis of this 2015 dataset will be presented in a forthcoming paper (Garufi et al., in prep.).

HD163296 is an A1 star at d = 122 pc (van den Ancker et al., 1998) that appears to be physically unassociated with any known star-forming region (Finkenzeller & Mundt, 1984). This source hosts a large circumstellar disk ($R \simeq 500$ AU) that has been inferred to be quite evolved. The gaseous disk is known to be twice as large as the dusty disk as traced by (sub-)mm imaging (de Gregorio-Monsalvo et al., 2013; Isella et al., 2007). scattered light images (Grady et al., 2000) trace small dust grains roughly out to the outer edge of the gaseous disk. Taken together, these observations have been interpreted as a sign of grain growth and inward migration for larger dust grains. However, no sign of dust or gas inner clearing has been observed at radii $r > 25$ AU (de Gregorio-Monsalvo et al., 2013). Interferometric near-IR observations show that a significant fraction of emission is originating at the theoretical dust sublimation radius (Benisty et al., 2010a). This object is also one of the few for which the location of the CO snowline has been inferred (155 AU, Qi et al., 2011). Finally, multi-epoch coronagraphic images of the source reveal variable scattered light from the outer ($> 2.9''$) disk (Wisniewski et al., 2008), whereas the stellar V magnitude is rather stable (Herbst & Shevchenko, 1999). A possible explanation for this is a variable scale height of the disk inner wall that is also responsible for near-IR variability (Sitko et al., 2008).

The A0 star HD141569A (d = 99 pc, van den Ancker et al., 1998) is part of a physical triple system with two M-dwarf companions at $9''$ from the primary (Weinberger et al., 2000). Its large ($R \simeq 400$ AU) asymmetric circumstellar disk has been imaged in scattered light by Augereau et al. (1999), Weinberger et al. (1999), Mouillet et al. (2001), and Clampin et al. (2003), who resolved a prominent spiral structure that was ascribed to the gravitational interaction with the two companions. Mid-IR imaging by Marsh et al. (2002) revealed a depression in the optical depth in the inner 30 AU, consistent with the near-IR deficit in the SED (Sylvester & Skinner, 1996).

HD150193A is an A2 star at d = 150 pc (van den Ancker et al., 1997) that is physically associated with a K4 star (Bouvier & Corporon, 2001) at $1.1''$ (HD150193B). A spatially unresolved disk ($R < 250$ AU) around the primary star was detected by Mannings & Sargent (1997) at 2.6 mm. The disk was also imaged in scattered light at near-IR wavelengths by Fukagawa et al. (2003). They ascribed a clear asymmetry in the disk structure to the interaction with HD150193B, where no disk was detected. Near-IR polarimetric images (Hales et al., 2006) revealed an unresolved structure with high polarization and suggested that a large amount of polarizing material is in the line of sight toward the star (in agreement with Whittet et al., 1992).

This chapter is organized as follows. First, we describe in Sect. 3.2 the observing conditions and data reduction. Then, we present in Sect. 3.3 the results of our observations. Finally, from Sect. 3.4 to Sect. 3.7 we discuss the favored morphologies for all three sources. We conclude in Sect. 3.8.

3.2 Observations and data reduction

HD163296, HD141569A, and HD150193A were observed between 2012 July 23 and 25, in the same observing run as SAO 206462 (presented in Chapter 2). The observations were also carried out with VLT/NACO in PDI mode, with the Wollaston prism and the rotatable half-wave plate for beam exchange, and by using the NACO SL27 camera in *HighDynamic* mode and readout in *Double RdRstRd* mode. The targets were observed in H and K_S bands, as well as in the respective narrow-band filters (NB 1.64 and NB 2.17) to obtain unsaturated exposures for photometric calibration. Observing conditions were photometric with average seeing varying from $0.58''$ to $1.66''$ (see Table 3.1 for observing settings and conditions). Five new objects were observed with VLT/NACO in K_S band between 2015 July 22 and 24. These are HD142666, HD144432, HD144668, HD145263, and HD152404. Moreover, second-epoch observations of HD163296 were carried-out in the same run. The instrument setup of the 2015 dataset is similar to the 2012, except that the SL13 camera was used for NACO hardware constraints. The details of these observations will be presented in Garufi et al. (in prep.).

The data were reduced with the procedure described in Sect. 2.3. The technique used to correct for instrumental polarization and cross-talk effects (Witzel et al., 2010) could not be properly implemented here because of the low science signal contained in these data. Therefore, in our pipeline we set some parameters (like e.g., the relative efficiency between the Stokes Q and U) to the typical values found for other objects (see Table C1 of Avenhaus et al., 2014b). The photometric calibrations was also performed similarly to Sect. 2.3, i.e. by converting the pixel-by-pixel count rates of the narrow-band images into surface brightness using the 2MASS magnitudes (Cutri et al., 2003) and applying a scaling factor to the H and K_S images. Significant uncertainties may derive from the variable near-IR flux of these sources (Pogodin et al., 2012; Sitko et al., 2008).

The final result of our data reduction is the pair of Q_ϕ and U_ϕ parameters described in Sect. 2.3. For the scope of this work, the total intensity I images of the sources are useful. These were obtained by summing the contributions from ordinary and extraordinary beams of each image and then averaging them.

3.3 Results

In Fig. 3.1 we show the Q_ϕ images resulting from the data reduction. The I images are shown in the right column. These images differ significantly from each other, and numerous artifacts are visible. Only the disk around HD163296 is detected from the Q_ϕ images.

Tab. 3.1 — Summary of observations. The columns list the object name, filter name, detector integration time (DIT), number of integrations per retarder plate position (NDIT) multiplied by integrations per dither position (NINT), number of dither positions, total integration time (TIT) per filter, and average airmass and optical seeing. Note that TIT per filter is obtained from the sum of all (DIT × NDIT × NINT × dither positions) multiplied by the four retarder plate positions.

Star	Filter	DIT (s)	NDIT × NINT	Dithers	TIT (s)	<Seeing>
HD163296	*NB* 1.64	0.3454	15 × 3	3	186.5	1.05″
	H	0.3454	140 × 6	3	3481.6	1.02″
	NB 2.17	0.3454	15 × 1	3	62.2	0.81″
	K_s	0.3454	100 × 3	3	1243.4	0.97″
HD141549A	*NB* 1.64	0.7	15 × 1	3	486	1.40″
		1	10 × 1	3		
		2	10 × 1	3		
	H	0.5	90 × 5	3	5400	1.66″
		3	75 × 1	3		
HD150193A	*NB* 1.64	0.3454	20 × 3	3	248.7	0.62″
	H	0.3454	140 × 8	3	4642.2	0.58″
	NB 2.17	0.3454	20 × 2	3	165.8	1.43″
	K_s	0.5	95 × 2	6	2280	1.27″

Therefore, we dedicate Sect. 3.3.1 to this object alone, whereas the two non-detections are described in Sect. 3.3.2.

3.3.1 Images of HD163296

The *H* and K_S band PDI images of HD163296 are shown in the first row of Fig. 3.1. All images are contaminated by AO residuals, as seen in the intensity images. Features at these locations must be considered spurious. However, the Q_ϕ images of HD163296 show an extended ring structure at $\sim 0.6''$ from the star with no counterpart in the *I* images. This structure is much more evident in the K_S band, but it is revealed in the *H* -band image as well. Note, however, that there are eight AO spots in the *H* image compared with only four in K_S and they are generally brighter. This may affect any potential weak detections from the Q_ϕ images in the *H* band.

The ring feature can be clearly traced to the NW and SE. We also report a tentative detection to the SW (only in the K_S). The ring pattern is interrupted by the southern and

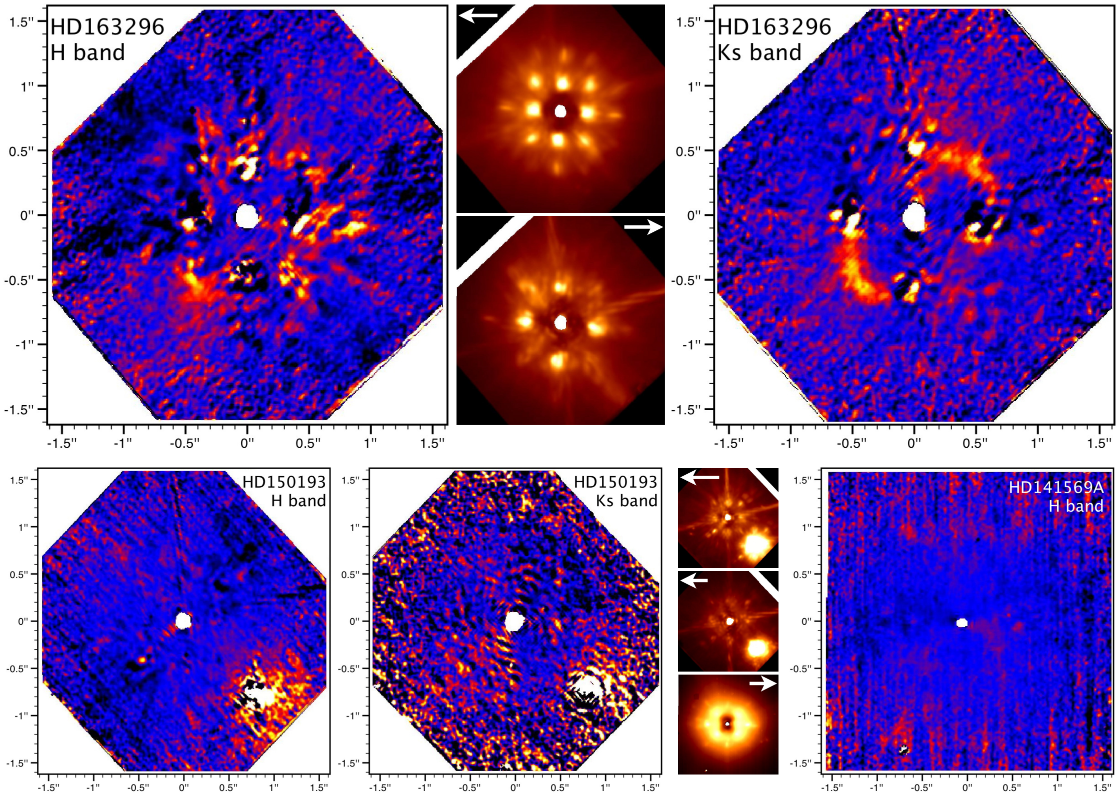

Fig. 3.1 — VLT/NACO imagery of HD163296 (top row), HD150193 (bottom left), and HD141569A (bottom right). The intensity images of each source are shown in the small panels. North is up, east is left. The white central area denotes the saturated pixels, which are not included in the analysis. All images are scaled by r^2 to compensate for stellar dilution. All Q_ϕ images are shown with the same linear scale, whereas the scale of the I images is arbitrary.

western AO spots. The radial width of this feature is always larger than the angular resolution of the observations ($> 0.09''$). This suggests that the structure is radially resolved. The brightest regions of the ring lie along the disk major axis (PA=137°, from submm images by de Gregorio-Monsalvo et al., 2013). Along this direction, emission above the 3σ-level is detected in the K_S band from $0.5''$ to $0.95''$ and from $0.4''$ to $1.0''$ (east and west side). In the H band the emission is revealed from $0.6''$ to $1.0''$ along both sides. The polarized surface brightness varies from 0.5 to 0.03 mJy/arcsec^2 in the K_S band and from 0.15 to 0.01 mJy/arcsec^2 in the H band. The inner edge of the ring structure does not appear to be sharp. In fact, the polarized-light distribution decreases smoothly from the peak luminosity to the noise level over $\sim 0.2''$. Along the SW minor axis, the tentative emission in the K_S band spans from $0.4''$ to $0.5''$. Given the radial profile along the major axis and assuming a circular disk, this translates into an inclination $i = 43^{\circ}{}^{+9^\circ}_{-14^\circ}$. This value is consistent with what was inferred by de Gregorio-Monsalvo et al. (2013) with submm imaging ($i = 45°$).

Since we detected emission along the East major axis from both bands, we calculated

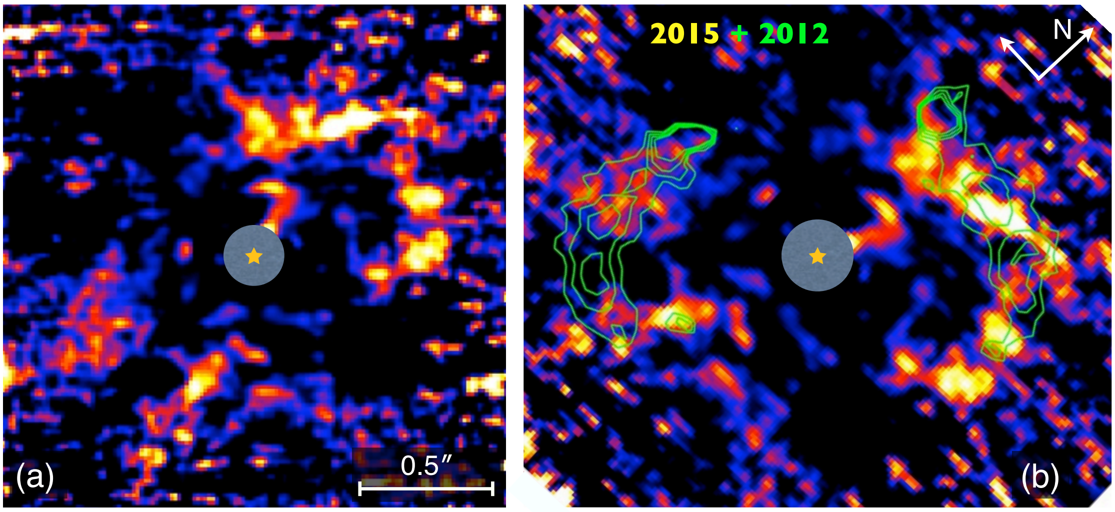

Fig. 3.2 — VLT/NACO image of HD163296 from the 2015 dataset. **(a)**: Q_ϕ image with North up and East left. **(b)**: the same rotated to match the disk major axis with the horizontal axis. The green contours are from the 2012 dataset shown in Fig. 3.1. The dark central area denotes the saturated pixels, which are not included in the analysis. Images are scaled by r^2.

the local $[H - K_\mathrm{S}]$ color and compared it with the stellar one. To do this, we considered an average emission from a three-pixel wide cut from 0.6″ to 0.7″ and used the 2MASS stellar color for the source (Cutri et al., 2003). The local disk $[H - K_\mathrm{S}]$ color is $1.92^{+1.29}_{-1.19}$, whereas the star shows a value of $0.75^{+0.08}_{-0.04}$. The disk emission is therefore likely to be redder than the stellar one (these magnitudes translate into a flux ratio of roughly three). However, the small overlap of the error bars (dominated by the photometric calibration uncertainty of ~ 40%) does not allow us to draw definitive conclusions.

The second-epoch Q_ϕ image of HD163296 in the K_S band is shown in Fig. 3.2. Despite the lower quality of this image compared to the 2012 dataset, the ring remains visible at the same radial location (see green contours in Fig. 3.2b).

3.3.2 Images of HD141569A and HD150193A

The final images of HD141569A and HD150193A do not reveal any extended emission in polarized light. As shown in the bottom row of Fig. 3.1, any feature in the Q_ϕ images corresponds to an artifact in the I images and is thus ascribable to an imperfect PSF subtraction.

In particular, the intensity images of HD150193A reveal the K4 companion at 1.11″ ± 0.03″. This separation is consistent within the error bars with what was obtained one decade before by Fukagawa et al. (2003, 1.10″ ± 0.03″). The Q_ϕ images are brighter around HD150193B because of the r^2 intensity scaling, but the signal-to-noise ratio does not diverge from a stochastic distribution.

3.4 Discussion on HD163296

As for all inclined disks, the distribution of the scattered light from HD163296 might be strongly affected by the disk geometry and the scattering properties. Therefore, the relation between these PDI maps and the actual dust distribution and disk geometry is not straightforward. In this section, we discuss the effects that may cause this "broken ring" structure.

3.4.1 Scattering phase function

The strongly azimuthally asymmetric structure revealed by our PDI images is the result of both the anisotropic scattering function (hereafter $f_{\rm scat}(\theta)$) and the scattering-angle dependence of the polarization fraction ($f_{\rm pol}(\theta)$). Since no scattered light image of this object has reached such small inner working angles and the disk-to-star contrast is not high enough for the disk to be detected from our intensity images, we cannot disentangle these two effects. However, scattered light images of the outer disk (Grady et al., 2000), spectroscopic observations of the jet (Ellerbroek et al., 2014), and the spatial morphology of the CO emission lines (Rosenfeld et al., 2013) all suggest that the NE region of the disk is the near side.

To constrain $f_{\rm scat}(\theta)$ and $f_{\rm pol}(\theta)$, we first obtained a rough estimate on the actual scattering angles, assuming that only the disk surface scatters light. The scattering angle θ for light from the major axis can be roughly estimated through $\theta = 90° - \beta$, with β being the disk opening angle. According to the gas vertical structure of this disk proposed by de Gregorio-Monsalvo et al. (2013) and Rosenfeld et al. (2013), β is $\sim 20°$ at 80 AU, and therefore $\theta \simeq 70°$. The scattering angle along the minor axis is given by $\theta = 90° \pm i - \beta$, where i is the disk inclination. The plus sign is for the far side, yielding $\theta \simeq 115°$, and the minus sign for the near side, yielding $\theta \simeq 25°$.

From the Q_ϕ images of Fig. 3.1 it is clear that the brightness distribution is maximized along the direction of the major axis. In particular, the polarized emission from the major axis ($\theta \simeq 70°$) is twice as high as that from the SW minor axis (the far side, $\theta \simeq 115°$, detected in the $K_{\rm S}$ band) and *at least* 1.5 times higher than that from the NE minor axis (the near side, $\theta \simeq 25°$, undetected, but constrained from the 3σ-sensitivity). The scattering function due to interstellar dust monotonically decreases with the angle, meaning that $f_{\rm scat}(25°) > f_{\rm scat}(70°) > f_{\rm scat}(115°)$. Therefore, the observed azimuthal distribution of polarized light translates into limits on the polarization fraction distribution:

$$\begin{aligned} f_{\rm pol}(70°) &\gtrsim 1.5 \cdot f_{\rm pol}(25°) \\ f_{\rm pol}(70°) &\lesssim 2.0 \cdot f_{\rm pol}(115°) \end{aligned} . \tag{3.1}$$

Given the typical $f_{\rm pol}(\theta)$ curves (e.g., Min et al., 2012; Murakawa, 2010), these constraints are satisfied by all dust grain sizes and types. In other words, flared and moderately inclined disks might show a polarized light distribution maximized along the major axis, similarly to HD163296, regardless of their grain properties.

The forward-scattering nature of dust may also suggest that the detection from the far side only is a contradiction. We note, however, that the images are noisier along the near side. Given our sensitivity, we can only claim that the near side is not much brighter than the far side (less than a factor 1.5). This is not necessarily suggestive of an isotropic scattering function, because the high polarizing efficiency at 115° can compensate for a lower $f_{\rm scat}$ at those angles (like in HD142527, Avenhaus et al., 2014b). To constrain the scattering asymmetry, an assumption on the $f_{\rm pol}(115°)/f_{\rm pol}(25°)$ ratio is thus needed. By looking at the typical $f_{\rm pol}(\theta)$ curves at $\lambda \simeq 2\,\mu$m (Murakawa, 2010; Perrin et al., 2009), this ratio varies with dust grain size and composition from 2.5 to 12. Assuming a conservative value of 12, the above claim yields

$$f_{\rm scat}(25°) \lesssim 18 \cdot f_{\rm scat}(115°). \tag{3.2}$$

This constrain in turn translates into a Henyey-Greenstein asymmetry parameter $g \lesssim 0.6$. The parameter thus obtained is only an approximation of the real g (Henyey & Greenstein, 1941), which can be obtained even though the knowledge of $f_{\rm scat}(\theta)$ is limited to a few values of θ. In near-IR, values lower than 0.6 are expected for sub-μm size particles (Pinte et al., 2008). However, particles can potentially be so forward-scattering that most of the radiation is scattered by $\theta < 25°$. In that case, the approximated g significantly diverge from the real asymmetry parameter (e.g., Mulders et al., 2013a).

Finally, the red color inferred in Sect. 3.3.1 can also provide insight into the grain size. An enhanced flux in the $K_{\rm S}$ band with respect to the H band (roughly three times higher than the stellar ratio) can be either explained with a dust albedo much higher at wavelengths $\gg 2.2\,\mu$m (as for larger μm-sized particles) or with a high difference between the polarizing efficiency for H and $K_{\rm S}$ band (as for sub-μm sized particles, see Fig. 1 of Murakawa, 2010). In particular, the latter hypothesis is consistent with what is suggested by the brightness asymmetry.

Summarizing, the maximization of the polarized flux along the major axis is not surprising and might be expected for all flared and inclined disks. On the other hand, the non-detection of the disk near side and the overall red color of the disk may suggest very small particles on the disk surface. However, deeper observations with a smaller photometric uncertainty are needed to draw significant conclusions on the dust population.

3.4.2 Disk morphology

Along the major axis, the Q_ϕ images depict the disk of HD163296 as a ring structure. However, the observed inner and outer edge of the emission may not represent the intrinsic physical dust distribution. Schematically, any abrupt radial discontinuity in the scattered light distribution can be due to four factors: (*i*) an intrinsic change in the density of scattering particles (like e.g. a disk cavity), (*ii*) a different amount of incident photons (because of self-shadowing), (*iii*) a substantial alteration of disk surface geometry, and (*iv*) a dramatic change in the properties of scattering particles. Here we discuss what is the favored scenario to explain our images of HD163296.

The most obvious interpretation would be that the lack of detected signal from the inner ~ 70 AU is due to a disk cavity. At first glance, the morphology of the disk of HD163296 may resemble those of some transition disks observed in PDI (e.g., Hashimoto et al., 2012; Quanz et al., 2011). However, the brightness radial increase from pure noise to peak intensity is smooth, which is contrast with the sharp profiles that are typically observed at the (directly illuminated) disk inner edge of gapped disks (Garufi et al., 2013; Quanz et al., 2013b). More importantly, no other datasets point toward the presence of a cavity, either from SED (Isella et al., 2007) or from sub-mm imaging (de Gregorio-Monsalvo et al., 2013).

Alternatively, one may invoke a self-shadowing effect. If the innermost part of the disk is puffed up, it can cast a shadow on the outer regions. However, if the disk is flared, its surface will re-emerge from the shadow at a certain distance from the star (e.g., Dullemond et al., 2001). Therefore, self-shadowing is more likely to occur in flat (Group II) than in flared disks (Group I). This effect has been proposed to explain the diverse shapes of the far-IR SED typically observed in disks, but it can also be applied to PDI images to explain the detection of annular gaps (e.g., Quanz et al., 2013b). Interestingly, HD163296 is often referred to as a border-line object between a group I and II (e.g., Meijer et al., 2008). Thus, the disk geometry may be such that only a fraction of the outer disk surface is shaded. A variable self-shadowing has been proposed for this source by Wisniewski et al. (2008) to explain the variable scattered light intensity observed in the $> 2''$ outer disk. This scenario is supported by the variable scale height of the inner disk wall, as inferred from near-IR SED monitoring (Sitko et al., 2008). In this scenario, the appearance of scattered light images might change with time. However, our second-epoch image of this source (see Fig. 3.2) reveals no change in the location of both inner and outer ring radius. Furthermore, the shadowing scenario cannot reconcile the presence of an outer radius for the detectable scattered light. These two notions discredit the shadow explanation.

A third possibility is related to the dust properties, that can effectively modify their albedo and/or polarizing efficiency and, thus, provide a substantially different polarized intensity. Grain growth can cause a significant decrease in the optical depth and has therefore been suggested as a possible explanation for the large cavities of transition disks (e.g., Dullemond & Dominik, 2005). Typically, this theory fails to explain the observed sharp change in the radial surface brightness and the rapid creation of the large cavities observed at (sub-)mm wavelengths (Birnstiel et al., 2012). However, the case of HD163296 does not require an explanation of these two features, since no cavity is observed at sub-mm wavelengths (de Gregorio-Monsalvo et al., 2013) and the radial light drop at the inner edge is smooth. In particular, the growth of scattering grains acts to decrease the observed polarized flux by three means: by lowering the intrinsic dust albedo, by providing a more forward-peaking phase curve (and thus a deficit at scattering angles larger than 20°), and by flattening the polarizing efficiency curve. Therefore, small variations in the grain size may be sufficient to explain the estimated contrast drop and thus the observed disk morphology. However, also the grain growth scenario encounters difficulties in explaining the rapid decline of the brightness at ~ 120 AU.

Finally, a substantial change of the disk scale height may explain the ring structure. In fact, the amount of observable scattered light is strongly dependent on the radiation incident angle. To estimate the disk scale height enhancement necessary to cause the observed "jump" in polarized light, we used the disk-to-star contrast at a certain radius r defined as:

$$\phi_{\rm pol} = \frac{F_{\rm pol}}{F_*/4\pi r^2}, \tag{3.3}$$

with F_* being the stellar flux in $K_{\rm S}$ band and $F_{\rm pol}$ the polarized flux measured along the major axis of our images. Note that $\phi_{\rm pol}$ indicates the polarized fraction of the scattered light contrast. This is, in turn, a combination of both the dust properties and the disk geometry and can therefore substantially differ from the intrinsic dust albedo (particularly if the scattering function is highly anisotropic, Mulders et al., 2013a). We obtained a factor $\Delta\phi_{\rm pol} \gtrsim 6$ difference between $0.65''$ (the location of the peak intensity) and $0.3''$ (representative radius inside the non-detection region). Then, we considered the phase functions and polarization degree curves by Min et al. (2012) and focused on the $45° - 90°$ interval (reasonable scattering angles along the major axis). In this range of scattering angles, the trend of the two curves is opposite (the scattering function decreases, the polarization efficiency increases). Thus, the net effect is limited. In particular, a contrast increasing by a factor 6 can only be explained with a disk opening angle that increases by more than 20° over ~ 40 AU. If we parametrize the disk scale height H as:

$$H(r)/H_0 = (r/r_0)^{\beta} \tag{3.4}$$

this factor 6 translates into a disk flaring index $\beta \gtrsim 2.0$, which is considerably higher than the typical strong flaring values (~ 1.2, e.g. Woitke et al., 2010). Thus, a "normally" flared disk cannot explain these images and a particularly puffed-up geometry beyond ~ 50 AU is needed. Interestingly, Dominik et al. (2003) showed that the mid-IR spectrum of this source behaves as those of flat disks, whereas an uncommon bump at 100 μm cannot be fitted by a continuous flaring disk. A physical explanation for such a geometric bump is proposed in the next section.

3.4.3 CO snow-line

As discussed in Sect. 1.2.2, dramatic changes in the dust composition and density may occur at the ice-line of a certain species. So far, the determination of disk snow-lines have been challenging. HD163296 is one of the few objects for which the location of the CO snow-line has been inferred (Qi et al., 2011). More specifically, the location where the CO begins to freeze out can be traced with the inner edge of the expected ring emission of DCO+ (Mathews et al., 2013). In the top two panels of Fig. 3.3 we show a spatial analogy between the location of the ring in scattered light and the DCO+ emission map from HD163296 (ALMA Science verification data, Mathews et al., 2013). One would be tempted to relate the increased scattered light brightness with the impact of icy molecules on the albedo of dust particles (e.g., Inoue et al., 2008). However, a number of arguments discredit this possibility. First of all, our data trace the disk surface, whereas the DCO+ emission is thought to originate from a deeper region in the disk mid-plane, and one may therefore expect the location of the CO snow line to be not coincident and, in particular, to be located farther out when traced by PDI images. Secondly, the low angular resolution of the ALMA data ($0.65'' \times 0.44''$) may discourage us from drawing strong conclusions on the spatial coincidence of the two datasets. Furthermore, ice mantles on the grain surface may also act to decrease the polarizing efficiency of grains because of the multiple scattering therein.

A more realistic explanation invokes the dynamics of particles at the ice-line. As explained in Sect. 1.2.2, a pile-up of dust grains may occur at the ice-line because of the different velocities of particles inside and outside of this line. Guidi et al. (2016) present new ALMA images of HD163296 which show a continuum brightness enhancement at 850 μm centered at $\sim$ 110 AU (see bottom panel of Fig. 3.3). Interestingly, the spatial interval where scattered light is detected well matches the region of increasing brightness continuum from ALMA. Speculatively, this is compatible with the polarized light data tracing the inner side of a disk scale height bump, which is directly illuminated by the central star. In any case, the brightness distribution of both NACO and ALMA datasets can realistically be related to the disk ice-line, which is located at $\sim$ 90 AU (as from the latest estimate by Qi et al., 2015, see horizontal line in Fig. 3.3).

3.5 Discussion on HD141569A

The disk around HD141569A shows prominent and extended structures out to hundreds of AU in scattered light (e.g., Weinberger et al., 1999). Therefore, its non-detection in our dataset (typically tracing the inner $\sim$ 100 AU) provides important information about the disk structure. A disk inner edge of a few hundreds of AU was inferred around HD141569A by Sylvester & Skinner (1996) by means of SED fitting. Even though this technique is known to be highly degenerate, the deficit of near- to -mid-IR flux shown by the source is effectively suggestive of a large dust gap. In fact, *HST* scattered light images at 1.1 μm (Weinberger et al., 1999) and 1.6 μm (Augereau et al., 1999) revealed a dramatic decrease of flux inside 160 and 250 AU, respectively, probably indicating a region depleted of material. In the top panel of Fig. 3.4 we plot the best fit for the scattered light profile in *H* band along the southern major axis from Augereau et al. (1999) and compare it with the 3σ sensitivity of our PDI images. If the scattered light profile observed

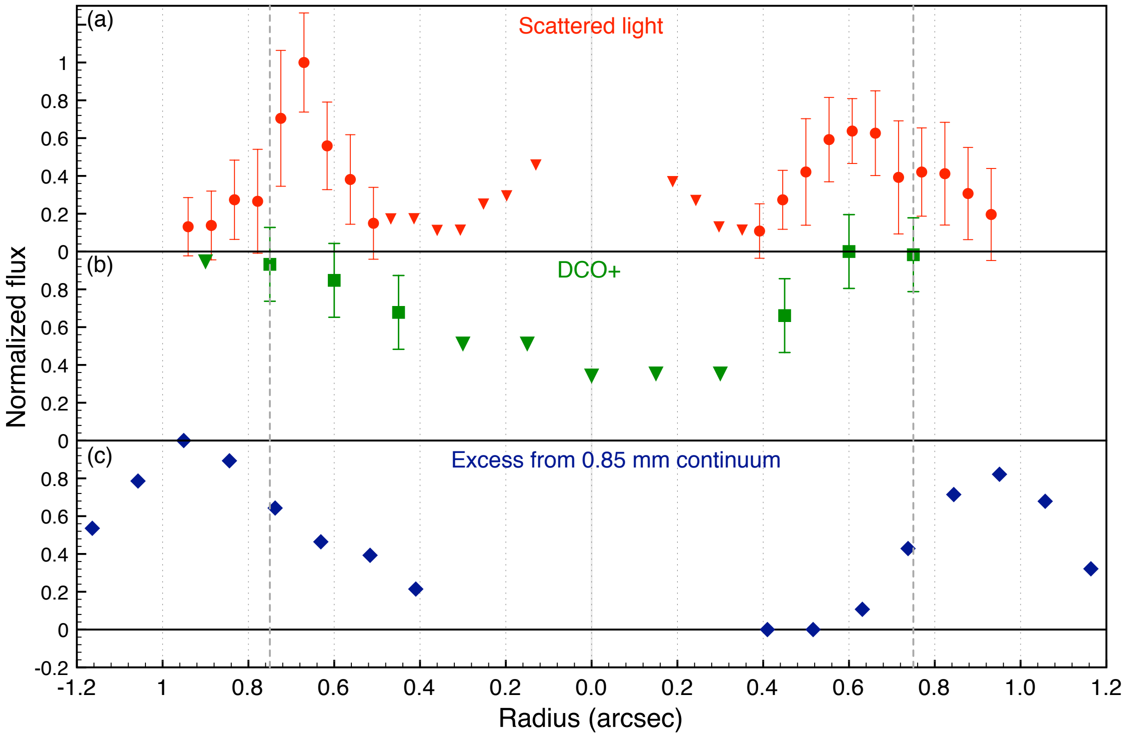

Fig. 3.3 — Scattered light distribution of HD163296 compared to ALMA data. **(a):** Contrast of the K_S band PDI images from 2012 calculated along the major axis from Eq. (3.3). **(b):** DCO+ intensity along the disk major axis from ALMA Science Verification data (Mathews et al., 2013). **(c):** ALMA 850 μm continuum along the major axis after the subtraction of a polynomial fit as described by Guidi et al. (2016). The horizontal line indicates the location of the CO snowline (Qi et al., 2015).

with *HST* does not dramatically increase inward of 1.5″, our PDI non-detection is still consistent with it (regardless of the polarization fraction). In the plot we also show the upper limit on the scattered light profile inside 1.5″ assuming a conservative polarization fraction of 10%.

Alternatively, we inspect whether the optical depth inferred at $r < 1''$ by Marsh et al. (2002) would be sufficient to provide a detectable polarized flux. These authors estimated the optical depth $\tau\,(1.1\,\mu\mathrm{m})$ normal to the disk mid plane, from their mid-IR observations. Interestingly, these values ideally reconnect to those obtained from scattered light farther out (Weinberger et al., 1999). Assuming that $\tau\,(1.1\,\mu\mathrm{m}) \simeq \tau\,(1.6\,\mu\mathrm{m})$, we consider that for optically thin dust, the optical depth is related to the observed polarized flux through

$$\tau \cdot (A_\mathrm{scat} \cdot f_\mathrm{pol}) = F_\mathrm{pol} \cdot 4\pi r^2 / F_*, \tag{3.5}$$

where A_scat is a quantity that depends on both the intrinsic dust albedo and the scattering function $f_\mathrm{scat}(\theta)$. By using our upper limit on F_pol and the 2MASS H band magnitude (Cutri et al., 2003) for F_*, we obtain that the condition for our non-detection is $A_\mathrm{scat} \cdot f_\mathrm{pol} \lesssim 0.025$. If we assume a conservative $f_\mathrm{pol} = 10\%$, A_scat must be lower than ~ 0.25, whereas this parameter can easily be as low as ~ 0.1 (e.g., Mulders et al., 2013a).

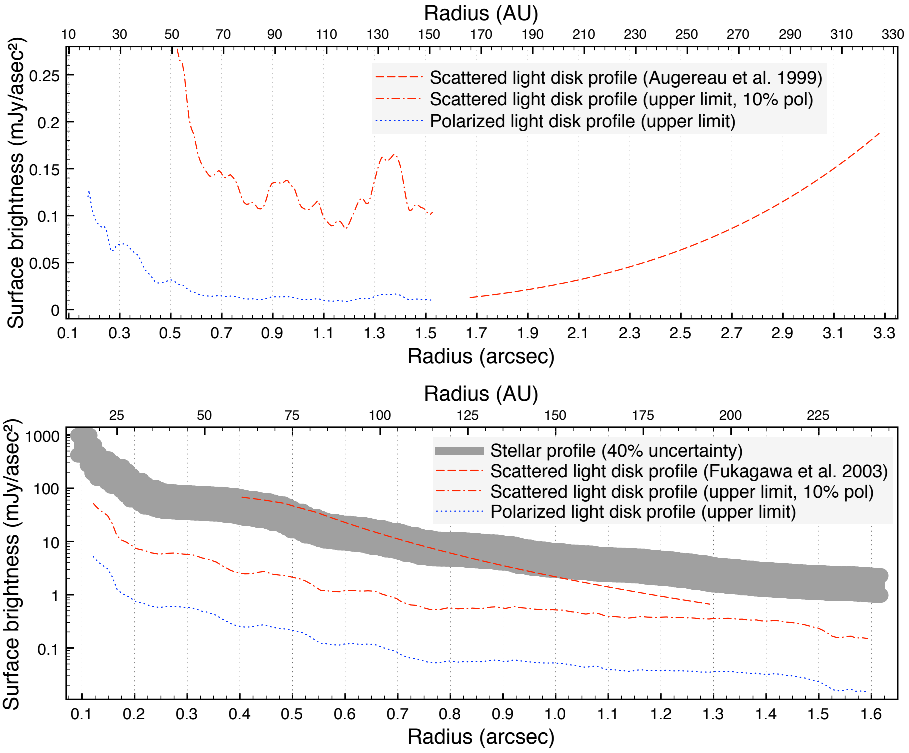

Fig. 3.4 — Surface brightness profile of HD141569A in the H band along the southern major axis (top panel) and of HD150193A in the H band along the northern major axis (bottom panel). The 3σ upper limit on the polarized-light profile is obtained from the Q_ϕ and U_ϕ images. The 3σ upper limit on the scattered light profile is obtained by assuming a conservative value for the polarization fraction of 10%. The gray area in the bottom panel denotes our measured stellar intensity profile, taking into account the 40% uncertainty from the photometric calibration. The scattered light disk profile by Fukagawa et al. (2003) is still consistent with being an unsubtracted stellar light.

The presence of dust in the inner 10−30 AU was also inferred by Moerchen et al. (2010) through mid-IR imaging. However, forsterite observations suggest that the dust grains in this region are large ($> 10\ \mu$m, Maaskant et al., 2015), and thus elusive in near-IR scattered light. Finally, Maaskant et al. (2014) showed that the ionization fraction of polycyclic aromatic hydrocarbons (PAHs) from this source is extremely high, suggesting that they are located in an optically thin environment.

Therefore, our non-detection of the disk at radii $0.1'' - 1''$ is consistent with earlier observations, and in particular with scattered light from the outer disk (Augereau et al., 1999; Weinberger et al., 1999) and with mid-IR observations in the inner regions (Marsh et al., 2002). Deeper observations may reveal scattered light from the inner disk.

3.6 Discussion on HD150193A

Evidence for the existence of a disk around HD150193A is provided, among others, by the infrared excess (Sylvester & Mannings, 2000) and by amorphous and crystalline silicate features (Meeus et al., 2001). Fukagawa et al. (2003) revealed a bright ~190-AU-large disk in *H* band scattered light using Subaru/CIAO. Since the coronagraphic mask was much smaller than our outer working angle, we compared their dataset with our results over a large range of radii ($0.4''$ to $1.3''$, see bottom panel of Fig. 3.4). To do that, we considered our 3σ sensitivity and used it as upper limit. The scattered-to-polarized brightness ratio varies with increasing distance from $\gtrsim 270$ to $\gtrsim 20$. This yields an upper limit for the polarization fraction of 0.4% at $r = 0.5''$ and 2.4% at $r = 1''$, which is much lower than any value observed or predicted so far for disks. We also set an upper limit on the scattered light profile by assuming a conservative polarization fraction of 10%. Moreover, in Fig. 3.4 we show that the stellar intensity profile from our dataset is only marginally higher than the scattered light images from Fukagawa et al. (2003). We estimate that our calibration is accurate to 40% and that any discrepancy by more than a factor of 2 is hard to explain. Fukagawa et al. (2010) noted that their observations may have been affected by the limited quality of the PSF and that further confirmation would be important. Hence, we are more inclined to believe that our upper limits are correct.

In addition, no sign of extended polarized emission was resolved by Hales et al. (2006) in the J band, even though the authors revealed a high degree of polarization, probably due to polarizing material in the line of sight. Dominik et al. (2003) argued that the SED of this source may be explained with a very small disk (with an outer radius as small as 8 AU). Such a compact disk would not be visible to our PDI images, which have an inner working angle of 15 AU.

Given the above points, the existence of an extended (hundreds of AU) disk is still to be confirmed. A variable self-shadowing scenario may in principle reconcile our dataset and that by Fukagawa et al. (2003). As discussed in Sect. 3.1, a variable inner wall scale height can provide a variable near-IR flux and a time-dependent shadowing effect on the outer disk. This mechanism is more likely to occur in Group II objects. Since HD150193A is a Group II object, this phenomenon may be the cause of our non-detection and may also explain the previous detection by Fukagawa et al. (2003).

If, at the moment of our observations, the disk inner wall was in a "high" state (to cast the speculated shadow), then our total intensity images might be in a high state as well. In fact, a significant fraction of the *H* -band emission from Herbig Ae/Be stars is thought to originate from the wall itself. Therefore, one may expect high *H* intensity when the shadow is cast, and vice versa. However, from the bottom panel of Fig. 3.4 it is clear that our intensity profile will be lower than that from Fukagawa et al. (2003) because it is comparable with their scattered light profile after PSF subtraction. This finding weakens the possible agreement of the two datasets.

3.7 Group I and II in scattered light

If the marginal- and the non-detections of HD163296 and HD150193A are due to the flat nature of these disks, one may expect all Group I disks observed in scattered light to be prominently detected. We investigated the existence of a correlation between the amount of (polarized) scattered light and the disk flaring angle. Unfortunately, a firm determination of the flaring angle from observational measurements is not possible. Historically, the excess at 60 μm with respect to the stellar flux was assumed to be a good discriminant of the disk geometry (e.g. Acke & van den Ancker, 2004). Recently, some authors proposed to use the flux ratio at 30 μm and 13.5 μm (Maaskant et al., 2015, 2013). Here we use this color as a first-order proxy of the disk geometry, even though we keep in mind that other dust and disk parameters may potentially affect it. By looking at the SED fitting by Woitke et al. (2015), it turned out that the only other parameter that can significantly modify the $F_{30}/F_{13.5}$ color is the disk inner radius.

In Fig. 3.5 we consider the [30/13.5] color (by means of the photometry by Acke et al., 2010) from a number of Group I (green) and Group II (purple) disks and compare it with the polarized-to-stellar light brightness contrast from Eq. (3.3). This contrast was obtained by averaging the values observed at different radii along the disk major axis from 0.2″ to 1.0″. All Group II objects have smaller [30/13.5] color than Group I. This supports the idea that this color is a good proxy of the flaring angle. A first-order relation between the disk geometry and the amount of scattered light is also clear from the plot, with all Group I objects being firmly detected and all Group II being only marginally or non-detected at all. This confirms the expectation that the disk scale height is the primary responsible for the amount of scattered light. However, any attempt to determine a clean trend from the plot should be discouraged because of the dependency of the $F_{30}/F_{13.5}$ color on the disk inner radius.

Figure 3.5 also shows which disks in the sample are known to have a large inner cavity (empty symbols), clearly revealing a one-to-one relation between the presence of a disk gap and the disk geometry. This notion has been used by Currie (2010) and Maaskant et al. (2013) to propose an alternative scenario for the evolution of protoplanetary disks. Instead of the classical I-to-II evolution described in Sect. 1.3.1, they suggest that Group I and II sources are diverse evolutionary path of a common ancestor, primordial flared disk. In Group I objects, the formation of giant planets sculpting the disk would precede the disk flattening. On the other hand, Group II objects would flatten without the concurrent formation of giant planets. The scattered light perspective on this scenario is also evolving. All Group I objects imaged in scattered light show prominent features which can be ascribed to the interaction with giant planets. The sample of Group II images is still too poor and the detections too faint to allow us to infer or rule-out whether the same features are present in flat disks. New generation instruments like VLT/SPHERE may be able to image Group II objects and thus clarify whether two distinct families of disks (and therefore evolutionary paths) exist.

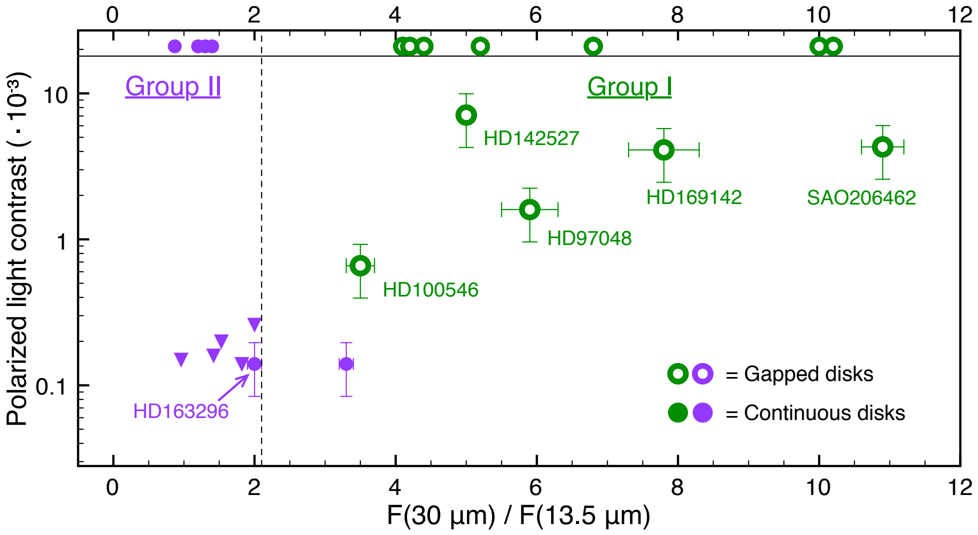

Fig. 3.5 — Polarized-to-stellar light contrast as from Eq. (3.3) for a sample of Herbig Ae/Be stars compared with the flux ratio at wavelengths of 30 μm and 13.5 μm. This ratio is indicative of the disk flaring angle. All group I objects (green) have been clearly detected in polarized light, whereas all Group II objects (purple) are either only marginally detected or non-detected. The vertical line sets the new Group I/II threshold proposed by Maaskant et al. (2013). Empty symbols indicate gapped disks, while full symbols indicate disks where no cavity has been revealed by any techniques. The upper space contains objects not yet observed in polarized light. Flux ratios are from Acke et al. (2010), contrasts from Garufi et al. (2013), Quanz et al. (2013b), Quanz et al. (2012), Avenhaus et al. (2014b), Quanz et al. (2011), Garufi et al. (2014b) and Garufi et al. (in prep.).

3.8 Summary and conclusions

We have discussed the H and K_S PDI observations of HD163296, HD141569A, and HD150193A. These objects were known to host very extended disk structures. However, our observations only revealed a faint or a totally absent contribution in polarized light. In particular, the disk around HD163296 is weakly detected in both bands. The brightness distribution is strongest along the major axis, and only a tentative detection is present along the minor axis. The radial profile smoothly decreases to the noise level inward of ~ 0.6″. The disk emission is likely to be redder than the stellar emission. On the other hand, HD141569A and HD150193A were not detected in any band.

The incongruity between these and previous observations inspire a discussion on the geometry of each object.

- HD163296: the peculiar azimuthal distribution of the polarized light from our images does not allow us to solidly constrain the morphology of dust grains. Asymmetries and colors may suggest that the disk surface is dominated by sub-μm size dust grains, but deeper photometrically reliable observations are needed to confirm this scenario. The radial profile is somewhat surprising, since the object is not known to be a transition disk. We argue that the favored explanation for the absence of scattered light inward of $0.5''$ is the disk flatness, and that a significant disk scale height enhancement (possibly due to the dynamics of particles at the CO snow-line) is the responsible for the ring structure observed at $0.7''$. This scenario is supported by our second-epoch image of the object and by both gas and dust ALMA observations.

- HD141569A: given our sensitivity, our non-detection of the disk from 10 to 100 AU is still consistent with scattered light images of the external disk, which show a significant flux deficit inward of $\sim$ 200 AU. The dust optical depth inferred from mid-IR imaging is also consistent with our non-detection. Slightly deeper observations may still detect a contribution from the inner 100 AU.
- HD150193A: this non-detection is not consistent with earlier scattered light images, which might be affected by inaccurate PSF subtraction. The disk may be smaller than our inner working angle or self-shadowed. The latter scenario, in particular, is supported by the flat nature of the disk. Deeper observations might not resolve any contribution from the disk.

We have also shown that the amount of scattered light primarily depends on the disk geometry. All Group I objects imaged so far with NACO in polarized light are prominently detected, whereas all Group II sources are only marginally or not detected at all. A one-to-one relation between the presence of a cavity and the disk geometry exists. VLT/SPHERE will allow us to investigate whether two distinct families of disks (and possibly of evolutionary paths) exist.

Finally, the time-dependence of the inner disk geometry motivates the importance of multi-epoch observations in scattered light. In particular, these could unravel the process of self-shadowing in Herbig Ae/Be disks. In this context, it is particularly important to monitor any potential correlation between the total near-IR intensity and the simultaneous scattered light brightness.

Guardate l'idrogeno tacere nel mare, guardate l'ossigeno al suo fianco dormire. Soltanto una legge che io riesco a capire ha potuto sposarli senza farli scoppiare. Soltanto una legge che io riesco a capire.

FABRIZIO DE ANDRÉ, *"Un chimico", 1971*

4

The SPHERE view of the planet-forming disk around HD100546

Based on a paper accepted by
Astronomy & Astrophysics

**A. Garufi, S.P. Quanz, H.M. Schmid, G.D. Mulders,
and the SPHERE Disk group ***

Received 10 December 2015 / Accepted 19 January 2016

** The complete list of authors can be found at the end of the chapter*

Abstract

We image with unprecedented spatial resolution and sensitivity disk features that could be potential signs of planet-disk interaction. Two companion candidates have been claimed in the disk around the young Herbig Ae/Be star HD100546. Thus, this object serves as an excellent target for our investigation of the natal environment of giant planets. We exploit the power of extreme adaptive optics operating in conjunction with the new high-contrast imager SPHERE to image HD100546 in scattered light. We obtain the first polarized light observations of this source in the visible (with resolution as fine as 2 AU) and new H and K band total intensity images that we analyze with the PYNPOINT package. The disk shows a complex azimuthal morphology, where multiple scattering of photons most likely plays an important role. High brightness contrasts and arm-like structures are ubiquitous in the disk. A double-wing structure (partly due to ADI processing) resembles a morphology newly observed in inclined disks. Given the cavity size in the visible (11 AU), the CO emission associated to the planet candidate *c* might arise from within the circumstellar disk. We find an extended emission in the K band at the expected location of *b*. The surrounding large-scale region is the brightest in scattered light. There is no sign of any disk gap associated to *b*.

4.1 Introduction

Our knowledge of the processes governing planet formation will be greatly enhanced by new generation instruments that recently started operations, like the SPHERE (Spectro-Polarimeter High contrast Exoplanet REsearch, Beuzit et al., 2008) instrument at the Very Large Telescope (VLT) and GPI (Gemini Planet Imager, Macintosh et al., 2014). The high-contrast and -resolution images enabled by these facilities will continue the recent plethora of observations of planet formation caught in the act. These consist of both the detection of planetary companions still embedded in disks (e.g., Biller et al., 2014; Kraus & Ireland, 2012; Reggiani et al., 2014; Sallum et al., 2015) and of their imprints on the natal environment (e.g., Garufi et al., 2013; Hashimoto et al., 2012, 2011; Quanz et al., 2013b). Imaging disk features (such as disk cavities, spirals, rings etc.) that can be due to the interaction with forming planets is fundamental to determine the framework (and the timeframe) of the planet formation. Excellent first examples of SPHERE's capability to image protoplanetary disks were provided by Thalmann et al. (2015) and Benisty et al. (2015).

The disk around HD100546 (B9V star at 97 ± 4 pc, Levenhagen & Leister, 2006; van Leeuwen et al., 2007) is one of the best laboratories to study the interaction with forming planets since it hosts two embedded companion candidates. The existence of HD100546b (hereafter planet *b*) at $r \simeq 50$ AU has been proposed by Quanz et al. (2013a), who detected a bright point source sitting on top of an extended emission in the L$'$ band. This detection was later confirmed by Currie et al. (2014). Quanz et al. (2015) obtained estimates on its temperature, emitting radius and luminosity, proposing the existence of a warm circumplanetary disk. More recently, Currie et al. (2015) reported the detection of emission in the H band at the location of *b*. On the other hand, the presence of HD100546c (planet *c*) has been claimed by Brittain et al. (2013) via spectroastrometric studies of the CO and OH ro-vibrational line emission. These authors ascribed the asymmetry of the OH line profiles to gas emission in an eccentric orbit at the disk wall and the annual CO line variability to a concentrated source of emission orbiting the star in proximity of the circumstellar disk wall at ∼ 15 AU. The latest fit to these variations gives an emitting area of ∼ 0.1 AU^2 at $r = 12.9$ AU (when at orbital phase $\phi = 6°$ from the major axis, Brittain et al., 2014). They noted that this emitting area is only slightly larger than the expected size of a circumplanetary disk around a 5 M_J planet at this orbital separation. Fedele et al. (2015) showed that the asymmetric profile of the OH lines can be explained by a misalignment of the spectrograph slit with no need to invoke an eccentric gas disk.

An extensive literature on this remarkable protoplanetary disk exists. The large, roughly 45°-inclined disk was firstly resolved in scattered light by Pantin et al. (2000). Peculiar disk structures (as the inner cavity, dark lanes and spiral arms) have been resolved in scattered light by Augereau et al. (2001), Grady et al. (2005), Ardila et al. (2007), Quanz et al. (2011), Boccaletti et al. (2013), and Avenhaus et al. (2014a). A quasi-coplanar inner disk at (sub-)AU scale has been studied by Benisty et al. (2010b) and Tatulli et al. (2011) with near-IR interferometry. A rounded disk wall at 11 AU has been claimed by Panić et al. (2014) through mid-IR interferometry. The disk was also resolved with mid-IR imaging (Liu et al., 2003) and at millimeter wavelengths by both ALMA and ATCA. The ALMA images (at moderate angular resolution) suggest that the large dust grains are mainly located in form of a ring between the radial locations of planet *c* and *b* (Pineda et al., 2014; Walsh et al., 2014). Pinilla et al. (2015) modeled these observations and found that if two planets at 10 and 70 AU are responsible for confining the dust in the observed ring, then the outer planet should be at least 2.5 Myr younger than the inner planet. Finally, ATCA observations at 7 mm (with resolution as good as 0.15″) constrained the disk cavity size to be ∼25 AU (Wright et al., 2015). Those observations also reveal a horseshoe-shaped concentration of grains at the disk inner edge.

We present the first SPHERE images of HD100546 in scattered light. The observations reported in this paper consist of high-contrast polarized light images in the visible as well as total intensity images in the near-IR obtained with the SPHERE sub-instruments ZIMPOL and IRDIS respectively. The ZIMPOL observations are the first polarized light images of HD100546 in the visible and are among the highest-resolution direct imaging data (∼ 0.02″) of a protoplanetary disk ever obtained. This paper is organized as follows. In Sect. 4.2 we describe observing conditions and data reduction, in Sect. 4.3 we present the results from both the ZIMPOL and IRDIS images, and in Sect. 4.4 and 4.5 we discuss our findings and provide our main conclusions.

4.2 Observations and data reduction

HD100546 was observed in the context of the Guaranteed Time Observations of the new high-contrast imager SPHERE (Beuzit et al., 2008), operating at the VLT in conjunction with the extreme adaptive optics (AO) system SAXO (Fusco et al., 2006). This paper presents the observations performed with the sub-instruments ZIMPOL (Zurich IMaging POLarimeter, Thalmann et al., 2008) and IRDIS (Infra-Red Dual-beam Imager and Spectrograph, Dohlen et al., 2008). Further IFS (Integral Field Spectrograph, Claudi et al., 2008) observations were taken along with the IRDIS observations (and will be presented by Sissa et al. in prep.). The observing conditions and the reduction of the ZIMPOL and IRDIS data are described in Sect. 4.2.1 and Sect. 4.2.2, respectively. We also retrieved archival VLT/NACO and Gemini/NICI datasets of HD100546, which are described in Sect. 4.2.3.

4.2.1 SPHERE/ZIMPOL

The ZIMPOL observations were performed on 2015, April 23 (night 1) and May 7 (night 3) in the R′ band (λ_c = 626 nm) in Differential Polarization Imaging (DPI). In this mode, ZIMPOL allows polarimetric diffraction-limited observations with very high polarimetric sensitivity. A fast polarization modulator (kHz) provides quasi-simultaneous observations of opposite polarization states, which are registered on the same "even" detector rows during two consecutive modulation cycles. The charges from the first polarization cycle are shifted to the "odd", covered rows and the information about the second state are then collected in the even rows. Furthermore, a half-wave plate (HWP) controls the polarization orientation and permits the observations of a full polarization cycle, consisting of the Stokes parameters $+Q$, $-Q$, $+U$, $-U$ (see e.g., Tinbergen, 2005).

All our observations were performed in DPI field stabilized mode. We alternated the object orientation by 60° and dithered its position by 14 pixels on the detector to evaluate any possible instrument artifacts. During night 1, HD100546 was mostly observed in FastPolarimetry mode, which provides the highest polarimetric precision with short exposure time (DIT=1.2 sec). Atmospheric conditions were initially challenging due to the transient presence of thin clouds but converged to good conditions later on (with optical seeing varying from 0.9″ to 2.4″). During the last observing block of night 1 and during all observations of night 3, we operated in SlowPolarimetry (DIT=20 sec) and employed a 155 mas-diameter classical Lyot coronagraph. The weather conditions during night 3 were significantly affected by a strong wind, which resulted in a largely variable seeing (from 0.9″ to 2.2″). A summary of the ZIMPOL observations is given in Table 4.1.

The DPI data reduction follows the technique illustrated by Avenhaus et al. (2014b). This includes the equalization of each pair of quasi-simultaneous polarization states to compensate for possible instrumental polarization. This technique assumes the star to be unpolarized. The astrometric calibration was performed following Ginski et al. (in prep.),

Tab. 4.1 — Summary of observations. Columns are: night number (see text), observing mode (and waveband), detector integration time (sec) multiplied by number of integrations, number of polarimetric cycles (for ZIMPOL only), and total integration time (sec). Numbers in brackets (for NDIT and P.C.) denote the amount of data used in the final reduction (see text), and the reported t_{exp} reflects this selection.

#	Mode (band)	DIT×NDIT	P.C.	t_{exp}
1	ZIMPOL/FastPol (R′) ZIMPOL/SlowPol (R′)	1.2×10 12×6	24 (15) 3 (-)	720 -
2	IRDIFS_EXT (K1K2)	16×256 (235)		3760
3	ZIMPOL/SlowPol (R′)	20×6	12 (7)	3360
4	IRDIFS (H2H3)	16×256 (135)		2160

i.e. by adopting a plate scale of 3.601 ± 0.005 mas/pixel and a detector orientation of $-1.61° \pm 0.11°$. The final product of our reduction is the pair of polar Stokes parameters (Q_ϕ, U_ϕ)[1]. Q_ϕ contains the polarized light component tangential to the star on the image plane. U_ϕ provides polarization vectors 45° inclined to the tangential component. For face-on systems only, Q_ϕ is equivalent to $P = \sqrt{(Q^2 + U^2)}$ but it is unbiased (since the signal is not artificially increased by the squares), whereas U_ϕ is not expected to contain any signal. In Sect. 4.4.2 we discuss the validity of this statement for inclined disks. Since the PSF in many exposures was degraded by the high atmospheric turbulence, the final images were produced by stacking a visual selection of best frames (see Table 4.1). This operation significantly decreased the effective exposure time but also clearly improved the contrast of the final images.

4.2.2 SPHERE/IRDIS

The IRDIS observations were taken in parallel with IFS. This possibility is enabled in IRDIFS mode by dichroic beam splitters and represents the SPHERE nominal infrared mode (with IFS operating at Y-J wavelengths and IRDIS in the H band). Observations in this mode, with IRDIS working in DBI mode (Dual-band imaging mode, Vigan et al., 2010) with the H2 and H3 filters (λ_c = 1589 nm and 1667 nm), were taken on 2015, May 28 (night 4). Furthermore, observations in IRDIFS_EXT mode (providing IFS coverage up to the H band and IRDIS working in the K1 and K2, λ_C = 2102 nm and 2255 nm) were taken on 2015, May 3 (night 2). Both runs were carried-out in pupil stabilized mode, allowing us to perform Angular Differential Imaging (ADI, Marois et al., 2006). An apodized pupil Lyot coronagraph with 185 mas-diameter was employed during both runs. During both night 2 and 4, the atmospheric conditions were good, with an average

---

[1] which was sometimes referred to as $(P_\perp, P_\parallel)$, (Q_T, U_T), or (Q_r, U_r).

seeing of 0.8″. The individual frame integration times were 16 seconds and in total 256 frames were obtained in both H and K bands.

The basic data reduction (e.g., bad pixel cleaning, flat fielding, image alignment) was performed using the SPHERE Data Reduction and Handling (DRH) pipeline (Pavlov et al., 2008). From astrometric reference measurements during the same observing run, we derived a pixel scale of 12.210 ± 0.029 mas/pixel and a true North orientation of $-1.784° \pm 0.129°$ (Maire et al., 2015). Visual frame selection was carried-out for both the H and K band data to sort out frames with poor AO correction leading to 121 frames in the H band and 21 frames in the K band that we disregarded from further analysis. The final selection of frames provides a field rotation of 26.8° in the H band and of 23.3° in the K band. A summary of the IRDIS observations is given in Table 4.1.

To subtract the stellar contribution and reveal the circumstellar material, we used the PYNPOINT package (Amara & Quanz, 2012; Amara et al., 2015). PYNPOINT uses Principal Component Analysis (PCA) to model the stellar contribution in each frame using a basis set of principal components (PCs) that was created from all existing frames. This was done for each filter independently. After stellar subtraction, all frames were rotated to a common sky orientation and mean combined. We varied the number of PCs and the inner/outer radius over which the fit is performed to estimate the impact of these parameters. For the final analysis we eventually settled on simply mean subtracted images (the main PC) as fitting a higher number of PCs led to more flux subtraction and did not reveal any significant additional structure. On the other hand, changing the inner and outer radius of the input images helped to identify features at different spatial scales. In this paper, we present the results obtained with inner/outer diameters equivalent to 0.14″ / 1.0″ (small scale), 0.5″ / 1.5″ (medium scale), 1.25″ / 5.0″ (large scale).

4.2.3 Literature data

We also make extensive use of archival data available for HD100546. We retrieved H (λ_c = 1630 nm) and K_S (λ_c = 2124 nm) band polarized light images of the source taken with VLT/NACO in April 2006 and in March 2013 (presented by Avenhaus et al., 2014a; Quanz et al., 2011). We also recover NACO ADI L′ (λ_c = 3770 nm) and M′ (λ_c = 4755 nm) band data taken in April 2013 and published by Quanz et al. (2015). Finally, we make use of Gemini/NICI K_S band images of HD100546 taken in March 2010 and reduced with the algorithm LOCI (Lafrenière et al., 2007) by Boccaletti et al. (2013).

4.3 Results

The ZIMPOL Q_ϕ and U_ϕ images resulting from our data reduction are described in Sect. 4.3.1 and 4.3.2, respectively. The IRDIS images are illustrated in Sect. 4.3.3. A compari-

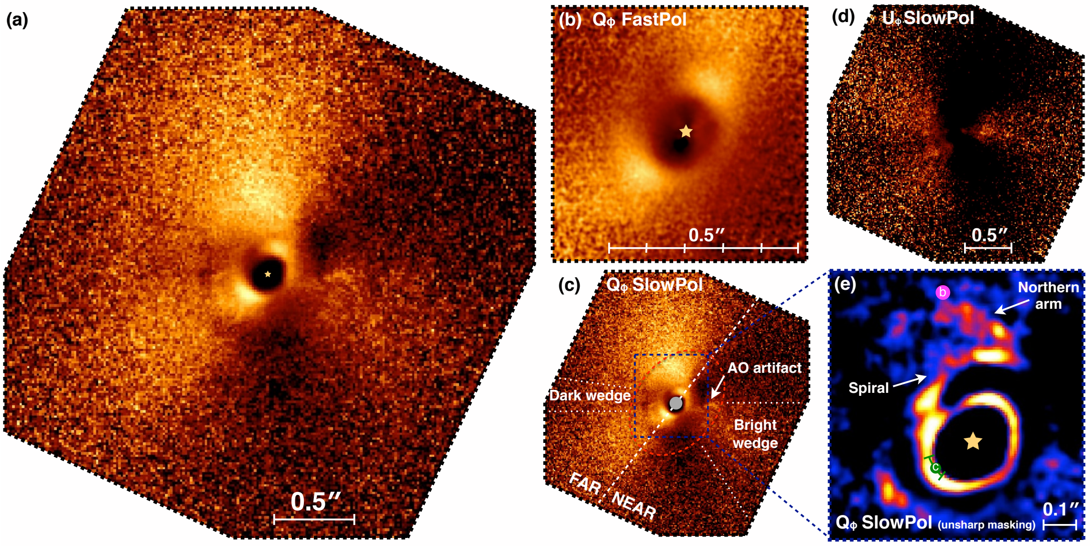

Fig. 4.1 — SPHERE/ZIMPOL polarized light imagery of HD100546. (**a**): Q_ϕ images in coronagraphic SlowPol mode. (**b**): Q_ϕ images in FastPol mode. (**c**): same as (a) with labels, where the white dashed line indicates the disk major axis and the inner grey spot the coronagraph size. (**d**): U_ϕ images in SlowPol mode, with color stretch twice as hard as in (a). (**e**): Unsharp masking of the Q_ϕ image (see Sect. 4.3.1). The predicted locations of *b* (Quanz et al., 2015) and of *c* in May 2015 with relative azimuthal uncertainty (Brittain S., private comm.) are shown in purple and green. All images except (e) are scaled by the squared distance from the star and are shown with linear stretch. North is up, East is left.

son between this dataset and the VLT/NACO as well as the Gemini/NICI images is shown in Sect. 4.3.4.

4.3.1 ZIMPOL Q_ϕ images

Figure 4.1a and 4.1b shows the clear detection of the disk around HD100546 in the Q_ϕ images obtained on night 3 and 1 respectively. The images show a globally complex structure. A signal is detected down to radii as small as 0.08″-0.11″ (depending on the azimuthal angle), which is a factor $\sim$ 4 larger than the inner working angle of the non-coronagraphic data. Along the major axis, two bright quasi-symmetric lobes lie outward of the detection inner edge. Farther out, polarized light with an azimuthally complex distribution is detected at radii as large as 0.6″-1.6″. Radial and azimuthal brightness profiles from the Q_ϕ images are shown in Fig. 4.2. These profiles are obtained by averaging the counts contained in a resolution element (i.e. 3×3 pixels). Errors are extracted from the Q_ϕ images as the standard deviation of the same box divided by the square root of the number of pixels therein. In this section, we analyze the brightness distribution of the Q_ϕ images. As from previous interpretations (e.g. Quanz et al., 2011), we will refer to the region close to the star with no detectable signal as the disk cavity (Sect. 4.3.1) and to the signal at larger radii as the outer disk (Sect. 4.3.1).

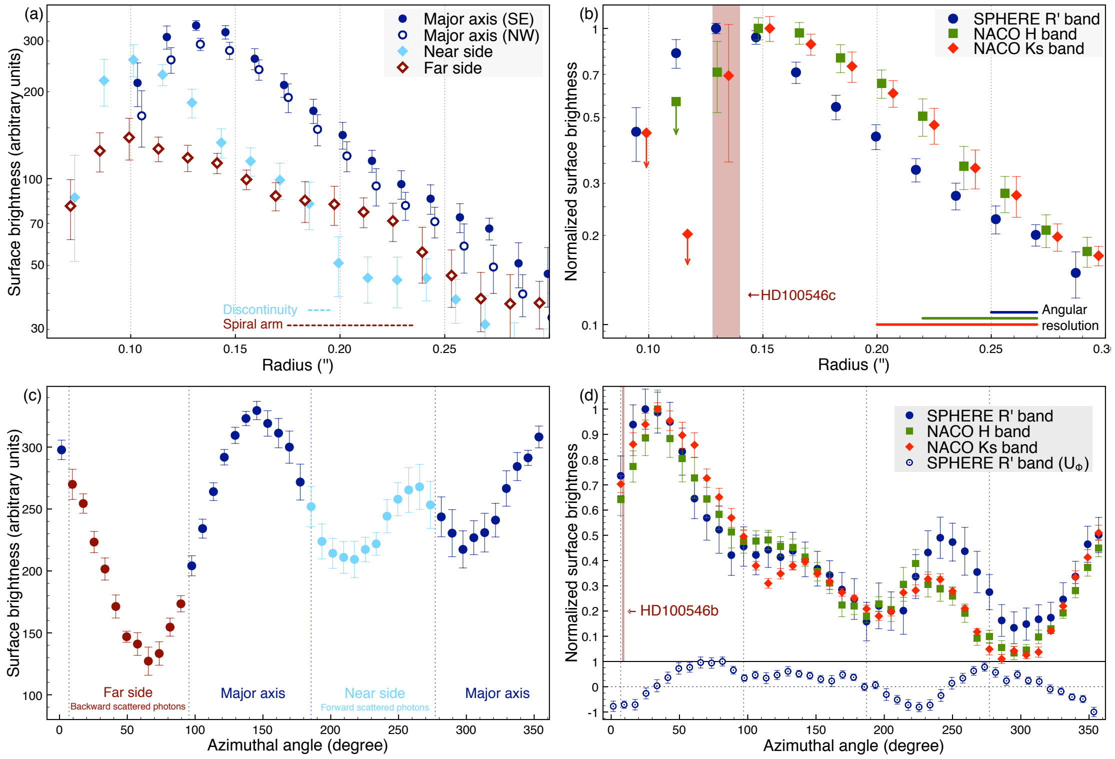

Fig. 4.2 — ZIMPOL polarized light brightness profiles. **(a)**: Radial profile in the inner 0.3″. The location of the abrupt decrement along the near side axis and the spiral arm bump along the far side axis are highlighted by the horizontal dashed lines. **(b)**: Radial profile along the SE axis compared to the same from the NACO dataset. Each profile is normalized to the respective peak intensity. The predicted radial location of HD100546c is indicated by the vertical brown area. The angular resolution of the three datasets is shown by the horizontal lines. **(c)**: Projected azimuthal profile of the inner rim (at $r = 0.15''$ for $i = 42°$). Angles from North to East. The emission from the four different quadrants is shown with different colors. **(d)**: Projected azimuthal profile at the predicted radial location of HD100546b (see red ellipse in Fig. 4.1c) compared with the same from the NACO dataset. Each profile is normalized to the respective peak intensity. The azimuthal location of *b* is indicated by the vertical brown region. The vertical dashed lines define the four quadrants as in (c). In the lower space, the same normalized brightness distribution from the SPHERE U_ϕ image is shown (note the different y-axis scale therein). All errors are given at 3σ level as described in Sect. 4.3.1.

Disk cavity

The cavity is elongated along the NW-SE direction, with the major axis lying at ∼ 140° East of North. Along this direction, the inner rim reaches its maximum emission on both sides at 0.13″ but the brightness of the NW side is ∼ 15% lower (see Fig. 4.2a). Along the SW side (i.e. the disk near side, Avenhaus et al., 2014a), the signal is on average 30% lower and the intensity peaks at 0.10″. This spatial difference is consistent with a circular cavity which is 40° – 50° inclined. Along the NE side (the far side), the emission is significantly weaker (a median factor 2.3 lower) but the signal also peaks at 0.10″. However, from Fig. 4.2a it is clear that the radial profiles along the near and the far sides are different. Along the near side, the slope is similar to the major axis, except for an abrupt decrease at 0.19″. On the other hand, the slope along the far side is much more shallow. Furthermore, a brightness *bump* is visible from 0.17″ to 0.25″. This bump can be also appreciated in Fig. 4.1e as a spiral arm (see Sect. 4.3.1).

In Fig. 4.2b, we show the ZIMPOL radial profile of the inner 0.3″ along the major axis and compare it with the NACO H and K_S band profiles. A small radial offset seems to exist between the two datasets. To evaluate this possible discrepancy, we adopted the technique described by Thalmann et al. (2015). Shortly, we integrated the flux contained in 3-pixel large concentric elliptic annuli, which are obtained from the projection of circular rings ($i = 42°$ and P.A. = 145°, Pineda et al., 2014). We searched for the largest increase in the integrated flux over two contiguous annuli and considered it as the location of the disk inner edge. In parallel, we also generated a disk toy model with surface brightness proportional to r^{-2} outside of a defined radius and only Poisson noise (quantitatively mimicking the image noise) inward. Then, we convolved the synthetic image with a two-dimensional Gaussian with the Full Width Half Maximum (FWHM) of our observations and changed the disk inner edge over a discrete range of values to qualitatively reproduce the signal distribution observed along the major axis.[2] Both techniques led to a inner radius of 0.11″ ± 0.01″. For consistency, we applied the same techniques to the NACO datasets and found 0.13″ ± 0.02″ for both H and K_S bands. Even though the error bars from these estimates overlap, the small offset from the radial profiles derived from the two datasets might be real rather than due to the different angular resolution of the observations.

We also extracted the brightness distribution along the inner rim (Fig. 4.2c) by averaging the contribution from a 5 pixel-wide ellipse at 0.15″, obtained by projecting a circular ring by $i = 42°$. We centered the ellipse slightly outside of the intensity peak (0.13″) to include only regions with detectable signal. The location of the main peak well matches the major axis. On the contrary, the peak to the NW is ∼ 30° offset toward North (consistently with the NACO dataset, Avenhaus et al., 2014a). The same amount of offset is found between the intensity peak on the near side and the location of the minor axis.

Outer disk

The azimuthal brightness distribution at large radii is highly asymmetric. The NE half of the image (the far side) is significantly brighter than the SW half (the near side). The distribution on the far side seems to be also discontinuous. As highlighted in Fig. 4.1c, a dark wedge to East separates two wide bright regions (centered at 10° and 120°). On

---

[2] The elliptic annuli technique may yield different results by changing the adopted inclination and position angle. However, we did not find any relevant difference over a reasonable range of values. The results from the toy model are valid under the assumption that the disk inner edge is sharp, which is not necessarily true (see Mulders et al., 2013b; Panić et al., 2014). However, for the purpose of comparison of the two datasets this uncertainty is not an issue.

the near side, a bright wedge (spanning 220°-280°) stands out. A sharp bright blob is also visible to West (marked as AO artifact in Fig. 4.1c). This is most probably an instrument artifact as it does not appear in differently sky-oriented frames while it is seen in the total intensity images at the radial location of the main AO ring (corresponding to the AO correction radius at $\approx 20\ \lambda/\mathrm{D}$, inside of which the AO system provides almost perfect corrections).

In Fig. 4.2d we show the normalized azimuthal profile from both NACO and SPHERE images, obtained at $r = 0.47''$ (i.e. the predicted radial location of *b*, Quanz et al., 2015) similar to Fig. 4.2c. Interestingly, the intensity peak from the three wavebands lie at the same azimuthal position, which is $\sim 15°$ farther East of North of HD100546b. The normalized distributions from the three wavebands are consistent within the error bars almost everywhere. The only exception is the SW bright wedge from the SPHERE image, which is roughly 40% brighter than the same structures from the NACO datasets. The azimuthal width of this wedge is similar to what we found along the rim (Fig. 4.2c) but it is $\sim 20°$ displaced.

Disk structures

No significant sub-structures can easily be spotted from the outer disk. Only a spiral arm to the NW at $r \sim 0.2''$ can be seen from Fig. 4.1a and Fig. 4.2a. To reveal any additional elusive features in the disk, we applied an unsharp masking technique to our images. This technique consists in adding a blurred, negative version of the original image to sharpen its details. It has been applied to protoplanetary disks images by e.g., Ardila et al. (2007) and Quanz et al. (2011). The resulting image must be interpreted with caution as, although sharper, it is most certainly not a more accurate representation of the real disk structure.

An unsharp masked version of the SPHERE Q_ϕ image was obtained by subtracting the smoothed version (by $\sim 10 \times$ FWHM) from the original image. Since the noise in the science image is high, we firstly subtracted the variance over a FWHM from the original image. This operation had the effect of decreasing the signal of the inner regions so as to avoid over-subtraction from the smoothed image, and resulted in a much sharper image of the inner $0.5''$. Finally, the resulting image has been smoothed by one FWHM. The morphology of the final image strongly depends on the choice of the mentioned parameters. However, some features are visible for a broad range of parameters. As shown in Fig. 4.1e, these are the inner rim, the spiral to NE, and an arm-like structure to North. The reality of this last feature, although not necessarily compelling by itself, will lend credence from the comparison with other datasets (see Sect. 4.3.3 and 4.3.4).

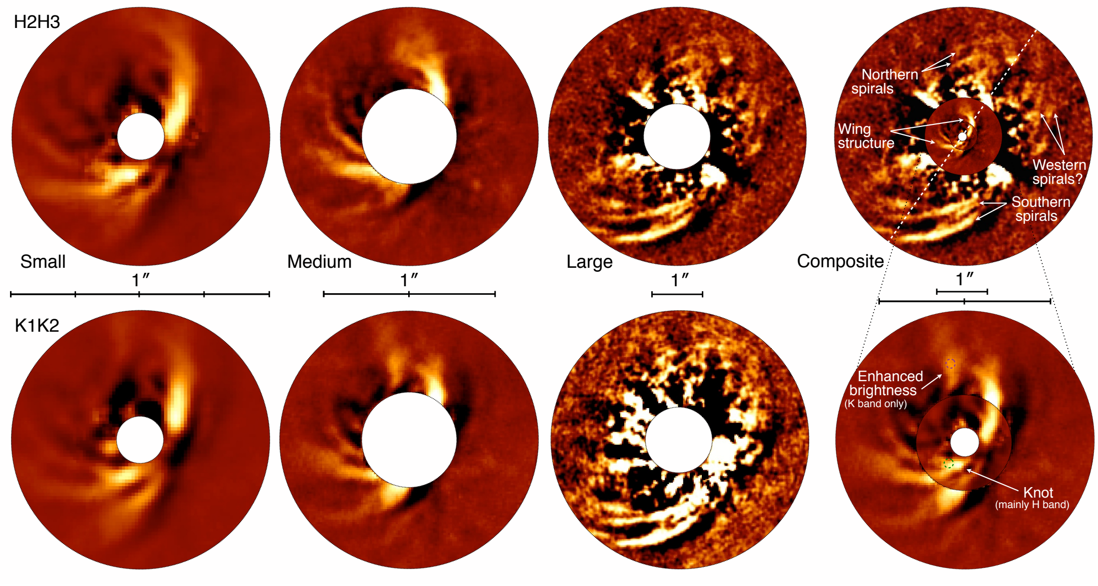

Fig. 4.3 — SPHERE/IRDIS imagery of HD100546. Images in the top row are in the H2H3 band, in the bottom row in the K1K2 band. The first three columns are the images resulting from reductions with increasing inner and outer software masks (see Sect. 4.2.2). Images from the third column have been binned by 2 × 2 pixels. The color stretch scales by 20 from first to second column, and by 100 from second to third, while it is arbitrary between the wavebands. The fourth column is a composite image (H band the top one, H/K the small/large bottom one). The dashed line indicates the disk major axis, while the circles point to planet *b* from Quanz et al. (2015) and putative *c* from Currie et al. (2015). North is up, East is left.

4.3.2 ZIMPOL U_ϕ images

The U_ϕ image resulting from our data reduction is shown in Fig. 4.1d. This image seems to contain a significant signal pattern. The intensity and the morphology of this signal is not likely to be due to an imperfect data reduction as the equalization of polarization states (minimizing instrumental polarization, see Sect. 4.2.1) cannot eliminate such a signal and the crosstalk effect between Stokes parameters (see Avenhaus et al., 2014b) is a minor effect in SPHERE. Furthermore, the spatial distribution of this signal is consistent through instruments and wavebands (see the U_ϕ NACO images by Avenhaus et al., 2014a), with a positive signal being diffusely detected to the East and to the West, and with a negative signal to the NW and SW. Both the bright and the dark wedge highlighted in Fig. 4.1c seem to have a counterpart in the SPHERE U_ϕ image. However, a ∼ 20° offset exists in the azimuthal location of the bright wedge from the Q_ϕ and U_ϕ images (it can also be seen in Fig. 4.2d).

More quantitatively, the signal in the SPHERE U_ϕ image varies from ∼ 20% of the Q_ϕ image at 0.2″ to ∼ 35% at 0.8″. These estimates are obtained by summing up the absolute values of all counts contained in the respective circular annulus. Similar values are found by comparing the peak-to-peak signal at those radii. We will discuss these findings in Sect. 4.4.2.

4.3.3 IRDIS images

The IRDIS images resulting from the reduction described in Sect. 4.2.2 are shown in Fig. 4.3. We found no significant differences between the H2 and the H3 bands as well as between the K1 and the K2 bands. Thus, we only show their combinations (i.e. H2H3 and K1K2 - or H and K for simplicity). The overall brightness morphology in the H and K images looks very similar but some minor, though important, differences exist. Different structures are revealed from the reductions with small, medium, and large scales (see Sect. 4.2.2).

Small scale. The main features in the small scale images (first column in Fig. 4.3) are two bright arms with wide pitch angles (the wings), which are roughly symmetric around the disk minor axis. Signal is detected almost down to the software mask radius at $r \sim 0.10''$. A bright knot is visible along the SE arm at $r \sim 0.14''$ (P.A.=155°) from both wavebands (but it is brighter in H). There is evidence of at least two additional arms to SE with comparable pitch angle. One of these (spanning P.A. $90^\circ - 110^\circ$) seems to originate from the bright knot of the SE arm. Interestingly, the spiral arm at $0.2''$ from the DPI data (see Fig. 4.1e) is not detected, whereas the faint northern arm matches the location of the Northern wing.

Medium scale. All arms revealed in the small scale images are also visible at medium scale (second column in Fig. 4.3). A diffuse enhanced brightness is detected in the K band at P.A. $\sim 10^\circ$. On top of this extended emission, a more localized emission spans radii from $0.43''$ to $0.47''$. Interestingly, the region of extended emission roughly lies at the end of the northern arm. We do not detect such an enhanced emission in the H band.

Large scale. Many bright arms are also detected in the large scale images (third column in Fig. 4.3). The two clearest detections lie to South in both images (the Southern spirals spanning angles $140^\circ - 200^\circ$). Two additional smaller arms can be seen at P.A. = 140°, close to the easternmost part of the main arms. Moreover, we detect in both bands two similar features to North (the Northern spirals which run in parallel from 40° to -20°) and also tentatively two arms which are specular to the Southern spirals around the minor axis (the Western spirals). Any other structure close to the software mask should not be considered significant, as that region is dominated by subtraction residuals and none of those features is persistent across different frames and reductions.

4.3.4 Comparison with near-IR images

Having collected throughout the years a rich set of data from 0.6 μm to 4.8 μm, both in polarized light and total intensity, we can obtain insight into both the disk geometry and the properties of scattered light by comparing this image collection. Figure 4.4 is a selection of these comparisons that we discuss in this section.

Figure 4.4a shows the brightness distribution in the H band, highlighting the differ-

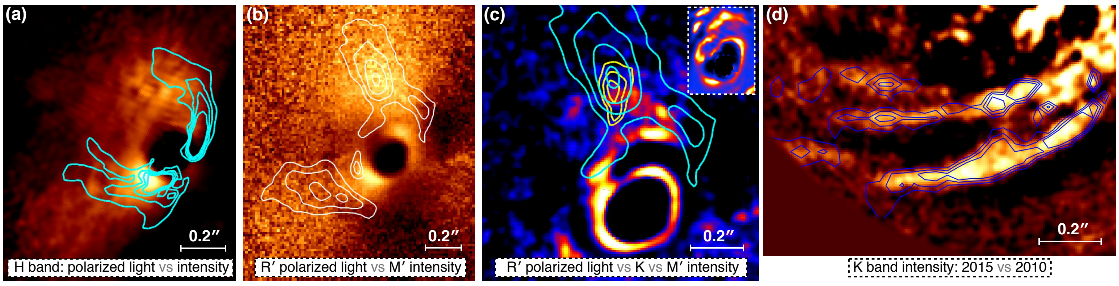

Fig. 4.4 — Multi-wavelength and -epoch images of HD100546. (**a**): NACO polarized light H band (colors) and IRDIS H band (contours). (**b**): ZIMPOL polarized light R′ band (colors) and NACO M′ band (contours). (**c**): ZIMPOL polarized light R′ band after unsharp masking (colors), IRDIS K band (yellow contours), and NACO M′ band (cyan contours). The inset image is the NACO polarized light K_S band image from 2006 after unsharp masking. (**d**): IRDIS K band from May 2015 (colors) and NICI K band from March 2010 (contours).

ences between the polarized light (from NACO, in color) and the total intensity distribution (from IRDIS, contours). It is clear that our IRDIS images can trace the signal as far down as the inner rim in polarized light, but that this is slightly azimuthally offset toward the near side. It is also evident how different the two brightness distributions are at large radii, with the polarized light being more distributed over the angles. Nonetheless, neither of the datasets reveal any significant emission from the SW side, and the locations of the bright/dark boundaries are very well matched.

In Fig. 4.4b, the shortest (R′) and the longest (M′) available wavebands are compared. The two bright large-scale wedges observed in the visible (colors) are also evident from the IR NACO data (contours). Particularly good is the match between the bright/dark edge to East. Also worth mentioning is the tentative detection of the spiral at 0.2″ (Fig. 4.1e) from the M′ dataset.

In Fig. 4.4c, we show the spatial connection between the northern arm spotted from the ZIMPOL image after unsharp masking (colors) and the diffuse emission from the M′ band (cyan contours) surrounding planet *b* (Quanz et al., 2015). The same emission from the IRDIS K band is shown (yellow contours). The arm seems to head to the location of *b* and a blurred counterpart of this arm may be seen in the M′ band. A minor radial offset between the emission in the K and M′ band seems to exist but requires further investigation. The inset image to the top right is the K_S band NACO from 2006 (Quanz et al., 2011) after applying unsharp masking similarly to the ZIMPOL image. It is clear that the location of the spiral is, to first order, the same.

Fig. 4.4d is a multi-epoch image of the outer disk region to South. The spiral arms detected by IRDIS in May 2015 are shown in colors while the same features imaged by Boccaletti et al. (2013) in March 2010 are shown in contours. No spatial shift is appreciable from the image.

4.4 Discussion

The interpretation of scattered light images is not straightforward. In fact, many physical and geometrical factors may equally contribute to the final appearance of such images. First of all, dust particles scatter photons anisotropically. This scattering angle distribution (referred to as the phase function) depends on the incident radiation as well as on the dust size and shape (see e.g., Min et al., 2012). In addition, scattered photons are polarized also depending on the scattering angle (hereafter the polarizing efficiency). In protoplanetary disks, the scattering angles experienced by the observed photons cannot be precisely determined because of our limited knowledge of the exact disk geometry. Secondly, the amount of radiation incident on the disk may be strongly affected by the geometry of the system at smaller radii (like e.g., warps or belts in proximity of the star). Moreover, multiple scattering on the disk surface may also have an impact on the scattered light distribution. Finally, instrumental contributions or data processing can also significantly alter the final images.

All this might suggest caution in interpreting the observed features, as very often these may have twofold (or multiple) explanations. In this section we discuss our findings in the context of different possible scenarios, focussing on the inner disk (Sect. 4.4.1), on the global disk morphology (Sect. 4.4.2), on the disk features (Sect. 4.4.3), and on the environment around planet *b* (Sect. 4.4.4).

4.4.1 Cavity and inner rim

Our results on the disk cavity (from Sect. 4.3.1) support the previous findings in DPI (Avenhaus et al., 2014a; Quanz et al., 2011), that are that the disk around HD100546 is truncated at roughly 15 AU and that this cavity is consistent with being intrinsically circular. Our data show no sign of offset along the major axis between the center of the cavity and the star, contrarily to what was found by Grady et al. (2005) with spectral observations (~ 5 AU). Along the minor axis, it is harder to claim or rule out any offset because the scattered light distribution from the back side of inclined disks inherently differs from that of the near side.

Mulders et al. (2013b) showed with mid-IR interferometry that the disk wall is rounded off over a large radial range and that this creates a broad surface brightness profile (10 to 25 AU) peaking at ~12 AU. Our radial profile of Fig. 4.2a may support this scenario. In fact, the brightness distribution along the major axis is constantly decreasing between the peak at 13 AU and 30 AU. This trend differs from those of e.g. SAO206462 (Garufi et al., 2013) and HD169142 (Quanz et al., 2013b), where an abrupt decline of the brightness profile is seen outward of the intensity peak. However, the exact slope of the brightness distribution at such small radii should not be trusted, because of the PSF smearing effects described by Avenhaus et al. (2014a).

The radial brightness distribution on the near side is very similar to what is seen along the major axis, except for an abrupt discontinuity (almost 50%) at a de-projected radius of 25 AU. This may indicate both a shadowed region or a change in the dust distribution at the disk surface. On the other hand, the profile on the far side is completely different. The shallow slope (clear from Fig. 4.2a) may suggest that from $0.1''$ to $0.2''$ our observations (partly) trace the disk wall, which is presumably seen at a $\sim 45^\circ$ angle from face-on. Such an exquisite data quality may inspire a later, robust modeling of the inner disk geometry to investigate this scenario.

Another intriguing result is the possible discrepancy between the location of the disk inner edge in the visible (11 AU) and in the near-IR (13 AU). This incongruity, though marginal, may be the result of a gradual increase of optical depth at the inner rim with disk opacity κ_λ varying with the wavelength. To explore this scenario, we calculated the spectral index β of $\kappa_\lambda \propto \lambda^\beta$ necessary to explain this discrepancy. We imposed the observed 11 AU and 13 AU edges as the z_1 yielding $\tau(z) \equiv \int_{z_0}^{z_1} \kappa_\lambda dz = 1$ in the visible and near-IR respectively, for a range of realistic values of z_0. This exercise resulted in β values spanning from -0.5 to -1.3, which is consistent with the expectations from (sub-)μm sized particles (e.g., Backman & Paresce, 1993). We note that the disk inner edge inferred from the visible dataset matches the location of the bright ring of emission (11 ± 1 AU) claimed through mid-IR interferometry by Panić et al. (2014).

Interferometric ATCA images of HD100546 (Wright et al., 2015) suggest that the cavity size at millimeter wavelengths is roughly 25 AU, which is more than twice as large as our estimate in the visible. Such a large discrepancy is a probable indication of the different behavior of μm- and mm-sized dust grains in gapped disks. In fact, many authors have shown that a pressure bump at the disk inner edge may act as a filter, allowing grains smaller than a certain size to drift inward but efficiently trapping larger grains (e.g., Brauer et al., 2008; Dong et al., 2012; Rice et al., 2006). Pinilla et al. (2012) have shown that two distinct cavity sizes are expected from the interaction of a disk with a planet, one for the gas (closer to the companion) and one for the millimeter particles farther out. This morphology has been observed in a number of disks by comparing scattered light images (tracing μm-sized grains which are well coupled to the gas) and millimeter interferometric images (e.g., Follette et al., 2015; Garufi et al., 2013; Tsukagoshi et al., 2014). More specifically, de Juan Ovelar et al. (2013) simulated visible and millimeter images of disks with a cavity carved by planets with different masses and orbital radii. Their results provide a fitting function to relate at different radii the visible/millimeter cavity size ratio with the planet mass. In the case of HD100546, this ratio is observed to be $\sim$0.5. Extending their results to $r < 10$ AU, one finds that a companion responsible for this dust differentiation should be more massive than 15 $M_{\rm jup}$. Adopting an analytic solution to this difference as in Garufi et al. (2013) (after the model by Pinilla et al., 2012) leads to an even higher lower limit ($\sim$ 40 $M_{\rm jup}$). Similar values were estimated by Mulders et al. (2013b) from the aforementioned shape of the disk wall and by Pinilla et al. (2015) by modeling ALMA observations. The scenario where multiple planets contribute to sculpt the disk and to differentiate the dust grains, though a valid explanation, has not been extensively studied because of the degeneracies introduced.

Given these considerations, the potential companion *c* associated with the compact CO emission by Brittain et al. (2013) is unlikely to be the (unique) cause of the observed cavity. From Fig. 4.2b, it is clear that such an object would lie within the μm-sized particles halo, disfavoring a scenario where these particles are retained at 11 AU because of the interaction with this object. Furthermore, the size of this CO emission would be associated with a planet with a relatively low mass ($\sim$ 5 $M_{\rm jup}$, Brittain et al., 2014), which is not consistent with the large cavity size nor with the observed μm-mm dust differentiation in the framework of the current models. An intriguing possibility is that this object is actually a consequence of the observed cavity, since the accumulation of material is favored by the pressure bump at the disk inner edge (e.g., Pinilla et al., 2012).

One would be tempted to relate the location of *c* in May 2015 (see Fig. 4.1e) with both the increased brightness of the SE side of the rim and the possible starting point of the main spiral. However, these associations may be fortuitous as both features were morphologically similar in the NACO dataset from April 2006 (Avenhaus et al., 2014a, see also Sect. 4.4.3), when the companion candidate was orbiting at angles close to North (Brittain et al., 2013). Recent H band images of HD100546 suggest the putative detection of *c* at angles of 150° (Currie et al., 2015). The location of this detection roughly matches the bright knot of the SE arm from the IRDIS images at the convergence of another arm (see bottom right panel of Fig. 4.3). However, the morphological similarity with the NW arm (both in brightness and symmetry around the minor axis) and the absence of such a knot in the K band images may suggest that the signal detected at those locations is pure disk emission. This discourages us from further analyzing and interpreting this feature. All in all, our dataset does not firmly reveal the presence of planet *c* nor of any disk feature which may be connected to the interaction with the planet candidate.

4.4.2 Disk morphology and scattering properties

The complex azimuthal distribution of the scattered light from HD100546, from both ZIMPOL and IRDIS, can only partially be explained by the scattering phase function. In this section, we discuss what other factors may contribute to the observations.

Q_ϕ vs U_ϕ images. The presence of some diffuse features of the Q_ϕ image (like the bright and dark wedges) also in the U_ϕ images (see Fig. 4.1d) may cast doubt on their intrinsic existence. In fact, the U_ϕ parameter has largely been used to determine the noise level of polarimetric observations (e.g., Avenhaus et al., 2014a; Garufi et al., 2013), since by construction it was not thought to contain any scattering information. However, the amount (20% to 35% of the Q_ϕ images) and the consistency (between different wavebands and instruments) of the U_ϕ image of HD100546 brought this view into question. Bastien & Menard (1988) showed that in optically thick, inclined disks the effect of multiple scattering may lead to significant deviations from purely azimuthal linear polarization.

Recently, Canovas et al. (2015) have produced synthetic U_ϕ images of disks with different inclinations and masses, showing that these images contain a strong signal in disks with $i > 40°$. The morphology of the synthetic images resemble that of HD100546, with the near side of the disk showing an alternation of strongly negative and positive signal. All this may suggest that multiple scattering in the disk of HD100546 may act to *transfer* a fraction of the polarized signal from the Q_ϕ to the U_ϕ image and therefore that the presence of features in both images does not necessarily discredit their intrinsic existence.

Inner rim. From Fig. 4.1a and Fig. 4.2c, it is clear that the polarized emission at the inner rim is maximized along the major axis. An analogous morphology is observed in other inclined disks (e.g., Garufi et al., 2014b; Hashimoto et al., 2012). This is not surprising because the polarizing efficiency of scatterers is typically maximized for scattering angles around 90° (e.g., Murakawa, 2010). It is also clear from Fig. 4.4a that the (non-polarized) emission from IRDIS is maximized at angles somewhat closer to the minor axis. This indicates that dust grains at the inner rim preferentially scatter in a forward direction. However, the net amount of this trend must be small compared to the polarizing efficiency, so as to maximize the polarized light (which is a combination of phase function and polarizing efficiency) along the major axis.

Polarized light from the (bright) far side. At larger radii ($> 0.3''$), the polarized emission is predominantly distributed on the disk far side. This morphology can be explained by the disk geometry. In fact, for inclined and flared disks (like HD100546) the scattering angles experienced by photons from the back side are closer to 90°. However, the high brightness contrast between the near and the far side and the darkness of the near side also in the IRDIS (non-polarized) images may both suggest backward-scattering particles at the disk surface (see also work by Avenhaus et al., 2014a). Specifically, two brighter regions are clear (at angles around 10° and 120°) and these are also visible in the M′ band (see Fig. 4.4b). These regions are offset from the major axis by a different angles respectively (52° to North and 28° to SE). This may indicate a larger disk flaring angle to North, since higher disk scale heights *move* the 90°-scatters toward the far minor axis[3]. This scenario is consistent with the different brightness of the two regions (with the North being twice as bright) and would also explain why the offset with the major axis increases with the radius ($\sim 10°$ at the rim and up to 50° for higher disk scale heights). On the other hand, the dark wedge to East (see Fig. 4.1c) is too localized to be described by a change in the disk scale height. A possible explanation for this deficit is a shadow. Shadows in protoplanetary disks have been predicted (e.g. Dullemond et al., 2001) and observed (e.g. Avenhaus et al., 2014b). The compact inner dust belt (e.g., Benisty et al., 2010b; Mulders et al., 2013b) may be responsible for such a shadow, similar to HD142527 (Marino et al., 2015). An alternative cause could be the spiral at 20 AU (see Fig. 4.1e), whose inner (brighter) portion is azimuthally consistent with the dark wedge. In this scenario, the dark wedge should rotate with the spiral (see Sect. 4.4.3).

---

[3] One can relate the scattering angle θ to the disk geometry through $\theta = 90° + \sin(\mathrm{P.A.}) \cdot i - \beta$ with i disk inclination, P.A. position angle from the major axis, and β disk opening angle.

Polarized light from the (dark) near side. The dark region to the SW is also challenging to interpret. This discussion must be related to the interpretation of the bright wedge therein (see Fig. 4.1c) which is 40% brighter than in the NACO dataset (Fig. 4.2d). Avenhaus et al. (2014a) suggested that the dark region is the result of a particularly backward-peaked scattering phase function (where photons from this region are scattered by angles as small as 50° − 70°). In this scenario, the bright wedge could represent the low tail of a forward-scattering peak, which is typically estimated to be in the range 0° − 30° (e.g., Min et al., 2016). These scattering angles are typically not observed in moderately inclined disks. However, a combination of high flaring angle and broad peak of the phase function may enable this in HD100546. Alternatively, this darkness may also be due to a large-scale shadow. Wright et al. (2015) revealed from millimeter observations a horseshoe structure lying at the SW disk inner edge and claimed that such an accumulation of particles may shadow the outer disk. However, our data trace the dark region down to 20 AU whereas the inner edge of the millimeter emission by Wright et al. (2015) is measured to be 25 AU. Furthermore, the presence of the bright wedge (highlighted in Fig. 4.1c) is difficult to reconcile with this scenario. It could be a region of penumbra due to asymmetries in the millimeter horseshoe, but the presence of this bright wedge stretching down to the disk inner rim (see Fig. 4.2c) disfavors this view. Nonetheless, these arguments do not rule-out a shadow cast by the aforementioned inner dust belt. A good vehicle to solve this ambiguity is inferring whether the different intensity between the SPHERE (visible) and the NACO (near-IR) datasets is due to the different epochs (which would favor the shadow scenario) or to the different wavebands (which would suggest a small dependency of the phase function on wavelength). Therefore, new near-IR observations (with e.g., SPHERE/IRDIS in DPI mode) will probably clarify the nature of the dark region.

Structures in the ADI images. The brightness distribution from the IRDIS images significantly differs from that of polarized light. From the small and medium scale images of Fig. 4.3, it appears as a double-wing structure rising from the major axis and arching toward the far side (similarly to the GPI images by Currie et al., 2015). Contrarily to the polarized light, the region between the two wings (to NE) is dark. To explore to what extent this morphology can be generated by the ADI processing, we produced synthetic images of HD100546 in the H band from the model by Mulders et al. (2013a) with Henyey-Greenstein asymmetry parameter g (Henyey & Greenstein, 1941) spanning the range from 0.5 to -0.2. Then, we convolved these images with the angular resolution of the IRDIS observations, replicated and rotated them to reproduce the field rotation of our observations (see Sect. 4.2.2) and gave them as input to PYNPOINT, which was run with the same setup described in Sect. 4.2.2 (with the small scale boundaries). Some illustrative outputs of this exercise are shown in Fig. 4.5. It turned out that the ADI processing transforms a continuous brightness distribution into a double-wing structure, with the wings always rising from the major axis and the azimuthal distance between them being strongly dependent on g. None of the test models could reproduce the observed morphology. Speculatively, this supports the idea of a strong backward-peaking phase function. However, a deeper discussion is beyond the scope of the current paper. Broadly speaking, this double-

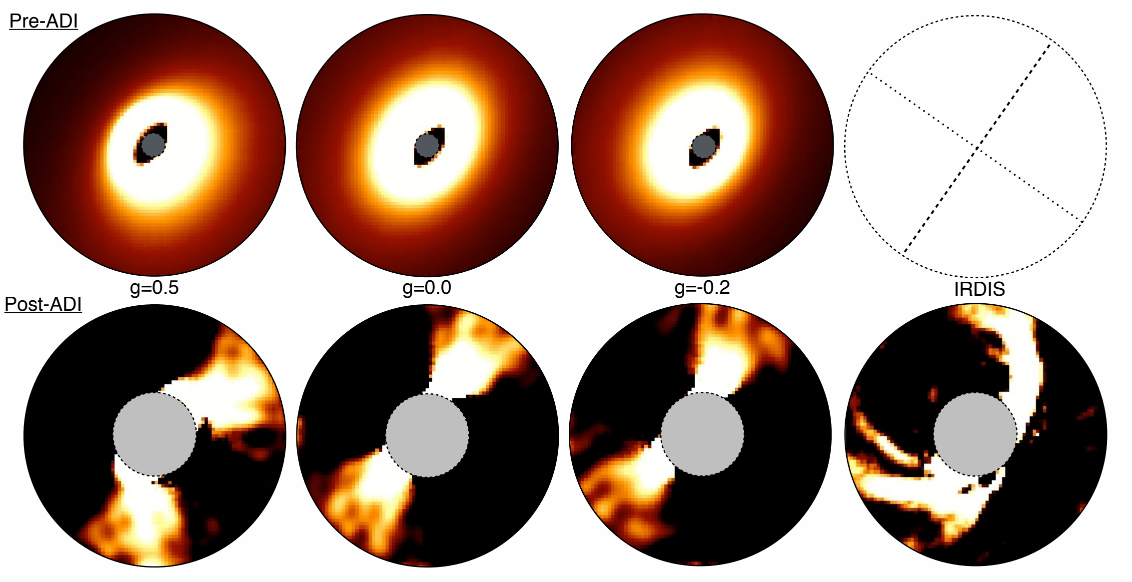

Fig. 4.5 — Impact of ADI processing on the scattered light distribution from an inclined disk. Top row: synthetic scattered light images in the H band obtained from the HD100546 model by Mulders et al. (2013a). Bottom row: the same after the ADI analysis performed by PYNPOINT. The different columns are models with different asymmetry parameters g with the last one being the IRDIS observations. The flux scales are arbitrary.

wing structure is a new form of feature (see also AK Sco, Janson et al., 2016) that may be recurrent among the observations of inclined disks carried-out with the new generation AO systems. Our exploration has shown that such a peculiar structure may still be interpreted in the context of a disk with an azimuthally continuous brightness distribution.

4.4.3 Disk structures

Almost all protoplanetary disks imaged so far with high resolution show peculiar features. Spirals (e.g., Benisty et al., 2015; Garufi et al., 2013; Muto et al., 2012) and annular gaps (e.g. Debes et al., 2013; Quanz et al., 2013b; Rapson et al., 2015) are, among these structures, the most intriguing. However, none of these disks seem to show both types of structures. The disk around HD100546 only shows spiral arms. Nonetheless, the absence of annular gaps is not less important in the context of planet-disk interaction and is discussed in Sect. 4.4.4.

The inner spiral arm at $\sim 0.2''$ (see Fig. 4.1e and Avenhaus et al., 2014a) is evident in polarized light but is not in the ADI images. This non-detection is most likely due to the ADI processing, which tends to cancel out any disk feature with high azimuthal symmetry and to over-subtract flux along the disk minor axis (see Fig. 4.5). The aperture of this spiral significantly differs from that of all others. In fact, if we define the aperture a as from $r = a\theta$ (with r distance from the star in arcseconds and θ azimuthal angle in radians[4]), this spiral is fitted by $a \sim 0.2$ whereas the other features farther out show a as high as $0.5 - 0.6$. The most interesting finding about this spiral is the absence of rotation on a nine-years timescale (see comparison with NACO data in Fig. 4.4c). This is surely not consistent with a Keplerian motion around the star. In fact, a spiral at a de-projected separation of 30 AU from a 2.4 $M_\odot$ star (van den Ancker et al., 1997), has an orbital period of roughly 100 years, which yields an expected rotation of about 30° in nine years.

The outer Southern spirals from IRDIS also show no apparent motion with respect to the detection by Boccaletti et al. (2013) (see Fig. 4.4d). Given the 5.2 years between the two epochs and a de-projected radius of 120 AU, the Keplerian motion of these spirals projected onto the disk plane is $\sim 1.5°$, which translates into $0.04''$ at those radii. It is difficult to determine the exact precision of our comparison because of the ADI processing. However, a visual inspection of the relative position of the spirals yields no sign of such a shift, as the edges of these features (whose width is on average $0.06''$) match very well between the two datasets.

The explanation for the absence of rotation is not obvious. If we focus on the inner spiral only (where the deviation from Keplerian motion is safe), one could try to relate its motion to that of a perturber object at larger radii. In fact, if this feature is excited by a massive object orbiting farther out (see discussion below), the spiral will be locked to the Keplerian motion of such an object. By conservatively assuming that the spiral has moved by less than 10° in nine years, this scenario would point toward a perturber object at more than 70 AU. Alternatively, the observed feature may only resemble a spiral arm and instead be a geometrical property of the disk (such as the top of the inner wall) whose appearance in scattered light is, therefore, not supposed to change with time. Analogously, one may be tempted to explain the Southern spirals with the geometrical properties of the disk. If one gives credence to the Western spirals of Fig. 4.3, the global arm-pattern visible from the near side resembles the wing-structure observed at small radii, with multiple arms symmetric around the minor axis which arch toward the far side. In this scenario, the Northern spirals would be morphologically different from the Southern/Western spirals and possibly be in Keplerian rotation. Such an idea can be tested after 2020.

The interpretation of the multiple arms from the IRDIS small/medium scale (left/middle panels in Fig. 4.3) is also not straightforward. The perfect symmetry around the minor axis suggests that this pattern is connected to the dust scattering properties and to the ADI processing from an inclined disk. As discussed in Sect. 4.4.2, the morphology of the wing structure can be explained by the ADI processing. It is also nonetheless clear from Fig. 4.5 that sharp features as the multiple arms observed from IRDIS cannot be generated from the pipeline. Moreover, the spatial consistency between different PYNPOINT runs, different instruments and observing modes reinforce that these features are real, even though their morphology differs from the *nominal* spiral arms frequently observed from face-on disks (e.g., Garufi et al., 2013; Wagner et al., 2015). Second epoch observations of these

---

[4] To obtain a, we de-projected the disk following Pineda et al. (2014, i = 42° and P.A. = 145°) and considered a disk opening angle of 10°.

inner features (as early as in 2018) and additional high-contrast ADI images as well as complementary RDI (Reference star Differential Imaging, Mawet et al., 2012) images of inclined disks will help unravel the nature of these arms.

A lively debate on the nature of the increasingly observed spirals in protoplanetary disks is ongoing. First of all, it has not been solved yet whether the detection of these features in scattered light reflects an intrinsic change in the dust distribution/properties down to the disk mid-plane (as proposed for SAO206462 by Pérez et al., 2014; Quanz, 2015). Many authors instead favor a scenario where these are due to a change in the pressure scale height (e.g., Juhász et al., 2015; Pohl et al., 2015). Disentangling the spiral morphology is also fundamental to determine their causes. The effects of the gravitational instability (Durisen et al., 2007) on the disk morphology has been studied with hydrodynamical simulations by e.g., Dong et al. (2015a), which successfully reproduce the appearance of SAO206462 and MWC758. However, gravitational instability has been disfavored in many specific cases because of the insufficiently massive nature of these disks (e.g., Boccaletti et al., 2013; Garufi et al., 2013), even though the gas mass in these disks is not firmly constrained. Recently, planet-disk interactions have been investigated quantitatively (e.g. Dong et al., 2015b; Juhász et al., 2015; Pohl et al., 2015). Despite the good agreement with the observed brightness contrast of spirals, this hypothesis has difficulties in reproducing the observed aperture of spirals (unless planets at very large radii or very high disk scale heights are invoked). Thus, the current framework does not allow us to firmly ascribe the spiral structure of HD100546 to any scenario.

4.4.4 Disk interaction with planet b

Independent multi-epoch and -filter observations of HD100546 in thermal IR have revealed the existence of a point source at $r \sim 0.46''$, sitting on top of an extended component (Currie et al., 2015, 2014; Quanz et al., 2015, 2013a). The current interpretation of the point source is thermal emission from a young planet (possibly surrounded by a circumplanetary disk) which is released from an effective area with $R \sim 7\ \mathrm{R_{jup}}$ and effective temperature $T_{\mathrm{eff}} \approx 930$ K (Quanz et al., 2015). This claim implied the rejection of a scattered light nature for this emission. The absence of a localized brightness enhancement from our ZIMPOL data in correspondence of the planet supports the validity of this rejection. Nonetheless, the large-scale emission around the point source is spatially consistent with our diffuse polarized emission to North (see Fig. 4.4b), suggesting that our observed diffuse emission is (mostly) scattered light. A similar feature is detected by Quanz et al. (2015) and Currie et al. (2014) to the SE and it also matches the diffuse enhancement from ZIMPOL.

Our ADI K band image reveals an extended emission at the location of the *b* planet (see mid-bottom panel of Fig. 4.3). This emission has no equivalent in the H band, and such a discrepancy is the only significant difference between the two wavebands. This dissimilarity can be either explained by the different optical depth of incident light or by the different extinction experienced through the disk by a local emission. The former explanation implies that the emission is purely scattered light and that a change in the disk morphology occurs between the depths where photons with H and K wavelengths are scattered. However, these two surfaces are probably too close to allow such a change. Moreover, the lack of a similar discrepancy between the H and K_S band NACO images by Avenhaus et al. (2014a) casts further doubt on the hypothesis. The latter explanation lies on the assumption that a local source of heat is present at a certain disk depth. This thermal emission would be subject to a higher extinction at shorter wavelength and would thus explain the observed difference. The recovery of this emission might still be possible in the H band, as shown by Currie et al. (2015). In any case, it remains to be understood whether the K band detection is actually related to any process of planet formation. A more in depth analysis of this emission, complemented by the simultaneous IFS data, will be presented by Sissa et al. (in prep.).

From the entire dataset analyzed in this paper, any disk interaction with planet *b* remains fairly elusive. First of all, there is no hint of any disk gap at the planet location. Based on the local noise of our images, we can rule out with 3σ confidence any brightness discontinuity more pronounced than 16%. We also integrated the flux from the back side contained in an ellipse passing through *b* (obtained consistently with the disk geometry) but we could not infer any discontinuity. The absence of any brightness discontinuity does not necessarily imply the absence of gaps in the distribution of μm-sized particles, since the high inclination of the source may not enable the observer to see through a narrow hole. From the angular resolution of the ZIMPOL data ($\sim$ 2 AU), some naive geometrical considerations, and the assumption of a 5 AU disk scale height at 50 AU (Montesinos et al., 2015), one obtains that our images could still detect a gap in the small dust grain distribution larger than $\sim$ 7 AU. Furthermore, the observation of a significant portion of the disk wall at the outer gap edge may result in a significantly different flux distribution (as shown for the inner rim in Fig. 4.2a). The absence of an observed discontinuity is difficult to reconcile with the large gaseous gap expected to be sculpted by a giant planet in a few tens orbits timeframe (e.g., Crida et al., 2006; Masset, 2008), unless the planet is very young ($\sim 10^{4-5}$ years, given its orbital period). de Juan Ovelar et al. (2013) showed that small polarized light brightness discontinuities in the R band are expected from interactions with $> 1\,M_{\rm jup}$ mass planets. An additional possibility to keep in mind is that the polarized signal deriving from the disk surface is blended with the contribution from halo particles. Speculatively, this contribution may be significant in highly inclined systems as suggested by the notion that sharp, prominent features like spirals and annular gaps are hardly observed in polarized light from inclined disks (see e.g., Follette et al., 2015; Hashimoto et al., 2012; Takami et al., 2013; Thalmann et al., 2015).

The only disk properties that can be ascribed to the interaction with *b* are the polarized light peak at comparable azimuthal angles (see Fig. 4.2d) and the Northern arm highlighted in Fig. 4.1e and Fig. 4.3. As discussed in Sect. 4.4.2, the large-scale enhancement of scattered light to the North is a possible imprint of a diffusely higher disk scale height. This may be in turn due to the hot environment produced by an enhanced disk accretion rate in correspondence of a luminous giant planet (as shown by the hydrodynamical simulations customized to HD100546 by Montesinos et al., 2015). Finally, the spatial connection between the northern arm detected in both ZIMPOL and IRDIS and the planet *b* is tantalizing. As discussed in Sect. 4.4.3, spiral arms are a natural outcome of the planet-disk interaction. However, this arm appears wrapped in the opposite direction of the other spirals and, as commented in Sect. 4.4.3, it is not clear yet to what extent this and other arm-like features in our datasets can be due to a combination of dust scattering properties and disk geometry.

4.5 Summary and conclusions

We present the first SPHERE observations of HD100546 in scattered light, obtained with the scientific sub-systems ZIMPOL (polarized R′ band) and IRDIS (H and K band). Complementary data from previous works enabled us to draw a comprehensive picture of the disk emission from 0.6 μm to 4.8 μm.

The ZIMPOL images in the visible resemble previous images in the near-IR, with the presence of an ellipsoidal cavity, of two bright lobes at the disk inner rim and of a tremendous brightness contrast between the disk near (dark) and far side (bright). The main findings from the analysis of these images are:

- The cavity size in the visible is 11 ± 1 AU. This is consistent with the estimate from mid-IR interferometry by Panić et al. (2014). This finding implies that the CO emission associated to the planet candidate *c* (Brittain et al., 2013) is located *within* the disk. The marginal difference with the cavity size in the near-IR (13 AU) can be ascribed to the different disk opacity at those wavelengths. The large discrepancy with the cavity size at millimeter wavelengths (25 AU, Wright et al., 2015) is qualitatively consistent with the dust differentiation expected from the interaction with a (yet unseen) giant planet in the disk cavity. The amount of such a discrepancy requires a $\gtrsim 15\ M_{\rm Jup}$ mass companion.

- A luminous wedge stands out from the dark side and this is much brighter than seen in previous near-IR images. The cause of this difference may also clarify the nature of the global darkness. If it is a time-related difference, then the wedge might be a penumbra in a globally shadowed region. If it is a wavelength-related difference, then we may be tracing the forward peak of an otherwise backward peaking scattering phase function. We favor the latter scenario and entrust the answer to upcoming near-IR images and custom models.

- The spiral arm at $r \sim 30$ AU revealed by Avenhaus et al. (2014a) does not show any proper motion in a nine-years timescale, inconsistent with being in Keplerian motion. This could either mean that the spiral is locked with the orbital motion of a companion at $\gtrsim$ 70 AU or that it is an azimuthally symmetric feature misinterpreted as a spiral.

- The effect of multiple scattering might be important. This is suggested by the morphology of the U_ϕ images, quantitatively resembling the expectations for an optically thick, significantly inclined disk when this phenomenon is taking into account (Canovas et al., 2015).

The near-IR IRDIS images, analyzed in ADI with PYNPOINT, show a complex multiple-arm structure at all spatial scales. In the H band, a bright knot along one of these arms roughly matches the location of the putative detection of planet *c* by Currie et al. (2015). This knot is not present in the K band. Moreover, an extended emission in the K band is detected at the location of the *b* planet (Quanz et al., 2013a). Our conclusions on the analysis of these images are:

- The double-wing structure symmetric around the minor axis can be generated from a continuous disk by the ADI processing. However, the multiple-arm morphology is consistent through different reductions and instruments and is therefore real. It is yet unclear whether these features are all spiral arms at the disk surface or marginal anisotropies accentuated by the scattering properties from an inclined disk. Their temporal evolution will provide fruitful insight into their nature.
- The extended brightness associated to HD100546b is most likely a thermal emission originating deep in the disk. The non-detection in the H band (and from all polarized light datasets) is in fact difficult to reconcile with the scattered light scenario. An in-depth analysis of this detection will be described by Sissa et al. (in prep.).

The direct comparison between the ZIMPOL and the IRDIS images with previous works also provide some insight into the disk geometry and the scattering properties. The difference between the total and the polarized light in the H band can be mainly ascribed to the ADI processing. However, the different brightness distribution at the disk inner edge may indicate that particles at the inner rim are more prone to forward-scatter photons, contrarily to what is seen at larger radii. Furthermore, the overall similarity of the polarized light at 0.6 μm and the total intensity at 4.8 μm supports the idea that the latter emission is also (mainly) scattered light.

All things considered, the imprints of the (probable) giant planets around HD100546 on the disk morphology remain elusive. We found no strong evidence of any disk feature which might be due to the interaction with HD100546c. Some of them (i.e. an arm apparently originating along the major axis, the enhanced polarization of a lobe at the inner rim, and a spiral arm at 30 AU) are, most likely, fortuitous. On the other hand, the maximized polarized brightness on a large scale around HD100546b may be speculatively connected to the expected enhanced disk accretion rate in proximity of the planet. Furthermore, the spatial connection between an arm-like structure and the localized thermal emission in the K band may also reveal some yet unclear planet-disk interplay. The absence of a detectable gap in correspondence of planet *b* also raises unanswered questions on the processes of planet formation. A narrow ($\lesssim$ 7 AU) or a shallow (providing a $\lesssim$ 16% flux decrease) gap, as well as a very young nature for *b* may reconcile with our observations.

These data are a showcase of the capability of the new generation high-contrast imager SPHERE. However, a lot remains to be understood about the enigmatic planet-forming disk of HD100546. The future confirmation (or rejection) of planet candidates and the recovery of disk features similar to those shown here from other suspected planet-forming disks (with SPHERE, ALMA, or GPI) will also help unravel the mysterious geometry of the disk around HD100546 and the mechanisms governing planet formation.

List of authors

A. Garufi[1], S.P. Quanz[1], H.M. Schmid[1], G.D. Mulders[2,3], H. Avenhaus[4], A. Boccaletti[5], C. Ginski[6], M. Langlois[7], T. Stolker[8], J.-C. Augereau[9,10], M. Benisty[9,10], B. Lopez[11], C. Dominik[8], R. Gratton[12], T. Henning[13], M. Janson[13,14], F. Ménard[9,15], M.R. Meyer[1], C. Pinte[9,15], E. Sissa[12], A. Vigan[16,17], A. Zurlo[4,18], E. Buenzli[1], M. Bonnefoy[9,10], W. Brandner[13], G. Chauvin[9,10], A. Cheetham[19], M. Cudel[9,10], S. Desidera[12], M. Feldt[13], R. Galicher[5], M. Kasper[9,10,20], A.-M. Lagrange[9,10], J. Lannier[9,10], A.L. Maire[12,13], D. Mesa[12], D. Mouillet[9,10], S. Peretti[19], C. Perrot[5], G. Salter[16], F. Wildi[19]

---

[1] Institute for Astronomy, ETH Zurich, Wolfgang-Pauli-Strasse 27, CH-8093 Zurich, Switzerland

[2] Lunar and Planetary Laboratory, The University of Arizona, Tucson, AZ 85721, USA

[3] Earths in Other Solar Systems Team, NASA Nexus for Exoplanet System Science

[4] Departamento de Astronomía, Universidad de Chile, Casilla 36-D, Santiago, Chile

[5] LESIA, Observatoire de Paris-Meudon, CNRS, Université Pierre et Marie Curie, Université Paris Didierot, 5 Place Jules Janssen, F-92195 Meudon, France

[6] Sterrewacht Leiden, P.O. Box 9513, Niels Bohrweg 2, 2300RA Leiden, The Netherlands

[7] CNRS/CRAL/Observatoire de Lyon/Université de Lyon 1/Ecole Normale Supérieure de Lyon, Lyon, France

[8] Astronomical Institute Anton Pannekoek, University of Amsterdam, PO Box 94249, 1090 GE Amsterdam, The Netherlands

[9] Univ. Grenoble Alpes, Institut de Planétologie et d'Astrophysique de Grenoble (IPAG, UMR 5274), F-38000 Grenoble, France

[10] CNRS, Institut de Planétologie et d'Astrophysique de Grenoble (IPAG, UMR 5274), F-38000 Grenoble, France

[11] Laboratoire Lagrange, Université Côte d'Azur, Observatoire de la Côte d'Azur, CNRS, Nice Cedex 4, France

[12] INAF - Osservatorio Astronomico di Padova, Vicolo dell'Osservatorio 5, 35122 Padova, Italy

[13] Max Planck Institute for Astronomy, Königstuhl 17, 69117 Heidelberg, Germany

[14] Department of Astronomy, Stockholm University, AlbaNova University Center, 106 91 Stockholm, Sweden

[15] UMI-FCA, CNRS/INSU France, and Departamento de Astronomía, Universidad de Chile, Casilla 36-D Santiago, Chile

[16] Aix Marseille Université, CNRS, LAM - Laboratoire d'Astrophysique de Marseille, UMR 7326, 13388, Marseille, France

[17] European Southern Observatory, Alonso de Cordova 3107, Casilla 19001 Vitacura, Santiago 19, Chile

[18] Núcleo de Astronomía, Facultad de Ingeniería, Universidad Diego Portales, Av. Ejercito 441, Santiago, Chile

[19] Geneva Observatory, University of Geneva, Ch. des Maillettes 51, 1290, Versoix, Switzerland

[20] European Southern Observatory, Karl-Schwarzschild-Strasse 2, D-85748 Garching, Germany

Rather than love, than money, than fame, give me truth.

Henry David Thoreau, *“Walden”, 1854*

5

Conclusions & Outlook

In this thesis, I analyzed optical and near-IR scattered light images of the protoplanetary disk around a number of young massive stars. As for many research works, drawing conclusions is challenging because of the rapidly evolving view on the subject. It is almost impossible to put an end to any lines of research, as typically these have already projected themselves into upcoming research efforts and ideas for the future. These considerations are particularly true for the (observational) field of the planet formation, where the simultaneous *kick-off* of the new-generation instruments VLT/SPHERE, GPI, and ALMA is revolutionizing our view. A non plus ultra example of this change is the surprising results on HL Tau by the ALMA Partnership et al. (2015).

For the above reasons, the conclusions and the future prospects of my research are encapsulated together in the following 10 points.

1. In the last years, Polarimetric Differential Imaging (PDI) turned out to be the best technique to image peculiar features of the few inner tens of AU of protoplanetary disks. Figuratively, this leadership is challenged by ALMA.

   Broadly speaking, the comparison of scattered light and (sub-)mm images with comparable resolution of the most known transition disks will provide new insight into the morphology of small and large dust grains at different disk regions.

2. We showed that the innermost location of μm-sized dust grains may differ from that of mm-sized grains (Chapter 2 and Chapter 4). Thus, the absence of a cavity in scattered light where suggested by mm imaging does not imply a continuous distribution of small grains, as was initially thought. This finding constitutes a qualitative explanation for the observed spectral deficit at near-IR wavelengths, and turned out to be a recurrent morphology of transition disks.

   This result urges the importance of scattered light observations with the smallest possible inner working angle. With VLT/SPHERE we have access to separations as small as 2 – 3 AU. This and the improved sensitivity and spatial resolution of ALMA will help us understand the interplay between gas, small, and large particles within the prominent cavity of transition disks.

3. Among all possible origins for the disk cavity in SAO 206462, only the interaction with orbiting companion(s) does not contradict any observational evidence. The same considerations apply to many other transition disks, where the presence of inner dust belt/accreting gas and the sharpness of the disk inner edge rule out photoevaporation, MRI, and dust grain growth. The planet/disk interaction can also explain the different distribution of small and large dust grains at the disk inner edge, even though no observational confirmation of this has been found yet. We speculated that a 5 to 15 $M_{\rm jup}$ mass planet may be responsible for the discrepancy observed in SAO 206462.

   The search for orbiting companions is complementary to disk imaging for the study of planet/disk interaction. The high-contrast achieved by SPHERE and GPI will either lead to new detections or put improved upper limits to the brightness of giant planets in the disk cavities. A numerical approach to study the effect of multiple (smaller) planets on the disk sculpting and dust differentiation will also help us unravel the origins of transition disks.

4. Spiral arms are imaged in many disks, besides the exquisite case of SAO 206462. It is still debated whether mm imaging with resolution comparable to the near-IR will resolve the same structures. Disentangling whether spirals are intrinsic change in the dust density or only wiggles at the disk surface is fundamental to infer their origin. In Chapter 2 we showed that the disk morphology in SAO 206462 is consistent with lower-resolution images at sub-mm wavelengths. As for the cause of the spirals, we inferred that gravitational instability is unlikely because of the relatively low disk mass. Current simulations of planet-disk interactions show that massive planets at large separations are needed to reproduce the observed morphology of spirals.

   ALMA images with AU-scale resolution of both dust and gas are the key to understand the nature of spirals. An improved estimate of the disk masses is necessary to investigate the scenario of gravitational instability.

5. The polarized light distribution from disks inclined by 30° – 60° might always peak along the major axis. In fact, in the range of scattering angles observed from mildly inclined disks the polarization phase curve changes more dramatically than the scattering phase function. Inclined disks observed in PDI typically show this brightness distribution. Two examples are HD163296 (Chapter 3) and HD100546 (Chapter 4). Also worth being mentioned that peculiar features like spirals and gaps in inclined disks are not commonly observed.

   Disentangling the effect of scattering phase function and polarization phase curve is a key-problem for the PDI community. To break this degeneracy, observations of the total scattered light are necessary. However, reference star subtraction is challenging because of the PSF variability, and angular differential imaging may significantly re-process the intrinsic brightness distribution (as shown in Chapter 4). A major effort in this direction will be made on newly acquired SPHERE data of RY Tau, which will also aim at understanding whether the effect of halo particles in inclined disks may (partly) prevent us from imaging the disk surface. This would explain the elusiveness of structures in inclined disks.

6. The disk scale height is the primary responsible for the amount of observed scattered light. Focusing on a dozen of objects, we showed that all Group I (flared disks) are prominently detected in PDI, whereas all Group II (flat disks) are either only marginally- or non-detected (see Chapter 3). It was also clear from the same sample that all Group I objects have a detected cavity whereas no Group II objects have revealed any sign of gaps with any technique. This is an intriguing dichotomy which may bring the standard view of the disk evolution into question.

   The upper limit on the brightness of some Group II objects from recent VLT/NACO observations will help us plan the SPHERE observations of these elusive objects. We aim to optimize these observations according to two possible scenarios: these objects are faint because of self-shadowing or they are smaller in radial extent than the Group I. The possible detection of Group II objects with SPHERE may also clarify whether Group I and II are two families of disks deriving from different evolutionary paths or they are different stages of the disk lifetime. The NACO data will contribute to solving this ambiguity, prior to the SPHERE data.

7. There is a plausible connection between the ring-like structure observed in the disk of HD163296 (shown in Chapter 3) and the location of the CO snow-line. This hypothesis requires further exploration but it is supported by new ALMA images of the sub-mm continuum. In any case, a local disk scale height enhancement in an otherwise flat disk is the most realistic explanation for the peculiar morphology of this disk in scattered light.

   With ALMA the location of the CO snowline will be determined for several other objects. This will allow us to possibly relate the ice-line with some disk features (like e.g. the annular rings of TW Hya or V4046 Sgr) observed in scattered light. This possible connection is fundamental to understand the physics at the ice-line in the context of the formation of large solids.

8. New forms of disk features are detected by SPHERE and GPI in scattered light, like a double-wing structure arching toward the far side or a bright wedge lying along the minor axis close to the observer. These features are shown in Chapter 4 and are most likely going to be recurrent. Our present view is that the ADI processing and multiple scattering (by e.g. halo particles) may be responsible for such structures.

   The increasing number of objects observed by SPHERE and GPI will determine how recurrent these new forms of features are. We aim to study numerically the effect of both multiple scattering on PDI images and PSF-subtraction processing on ADI images.

9. Despite the many peculiar structures observed in protoplanetary disks, any imprints of (forming) planets on the natal disk remain elusive. This is only partly due to the limited number of known embedded planets (those confirmed can be counted on one hand up to today). Even though the disk of HD100546 hosts two planet candidates, no disk feature can be clearly ascribed to the interaction with them (Chapter 4).

   Broadly speaking, new detections of forming planets and an increased sample of disks observed by new-generation instruments will most probably help us ascribe some of the prominent disk structures (spirals, dips, cavities, rings etc.) to processes connected to on-going planet formation.

10. On a more personal level, the field of planet formation will become increasingly interesting, with the community of disk imaging playing as the actor in a leading role. In the near future, ALMA, GPI, and SPHERE will supposedly bring to light surprising results on protoplanetary/debris disks. Theorists are going to be challenged by these images. On our side (as observers), we will have to gain an immediate understanding of the newly taken data, so as to plan to following observations accordingly. The succession of observing cycles is indeed looking to be very intense! On a longer timescale, other instruments like the James Webb Space Telescope, Gaia, and the European Extremely Large Telescope will keep contribute to the golden era of exoplanetary sciences.

Bibliography

Acke, B., Bouwman, J., Juhász, A., et al. 2010, ApJ, 718, 558

Acke, B. & van den Ancker, M. E. 2004, A&A, 426, 151

Alexander, R. D. & Armitage, P. J. 2007, MNRAS, 375, 500

ALMA Partnership, Brogan, C. L., Pérez, L. M., et al. 2015, ApJ, 808, L3

Amara, A. & Quanz, S. P. 2012, MNRAS, 427, 948

Amara, A., Quanz, S. P., & Akeret, J. 2015, Astronomy and Computing, 10, 107

Andrews, S. M. 2015, ‘PASP, 127, 961

Andrews, S. M., Wilner, D. J., Espaillat, C., et al. 2011, ApJ, 732, 42

Andrews, S. M., Wilner, D. J., Hughes, A. M., Qi, C., & Dullemond, C. P. 2009, ApJ, 700, 1502

Ardila, D. R., Golimowski, D. A., Krist, J. E., et al. 2007, ApJ, 665, 512

Armitage, P. J. 2015, ArXiv e-prints

Augereau, J. C., Lagrange, A. M., Mouillet, D., & Ménard, F. 1999, A&A, 350, L51

Augereau, J. C., Lagrange, A. M., Mouillet, D., & Ménard, F. 2001, A&A, 365, 78

Avenhaus, H., Quanz, S. P., Meyer, M. R., et al. 2014a, ApJ, 790, 56

Avenhaus, H., Quanz, S. P., Schmid, H. M., et al. 2014b, ApJ, 781, 87

Backman, D. E. & Paresce, F. 1993, in Protostars and Planets III, ed. E. H. Levy & J. I. Lunine, 1253–1304

Balbus, S. A. & Hawley, J. F. 1991, ApJ, 376, 214

Bastien, P. & Menard, F. 1988, ApJ, 326, 334

Benisty, M., Juhasz, A., Boccaletti, A., et al. 2015, A&A, 578, L6

Benisty, M., Natta, A., Isella, A., et al. 2010a, A&A, 511, A74

Benisty, M., Tatulli, E., Ménard, F., & Swain, M. R. 2010b, A&A, 511, A75

Beuzit, J.-L., Feldt, M., Dohlen, K., et al. 2008, in Society of Photo-Optical Instrumentation Engineers (SPIE) Conference Series, Vol. 7014, Society of Photo-Optical Instrumentation Engineers (SPIE) Conference Series, 18

Biller, B. A., Males, J., Rodigas, T., et al. 2014, ApJ, 792, L22

Birnstiel, T., Andrews, S. M., & Ercolano, B. 2012, A&A, 544, A79

Birnstiel, T., Dullemond, C. P., & Brauer, F. 2010, A&A, 513, A79

Boccaletti, A., Pantin, E., Lagrange, A.-M., et al. 2013, A&A, 560, A20

Boss, A. P. 2006, ApJ, 641, 1148

Bouvier, J. & Corporon, P. 2001, in IAU Symposium, Vol. 200, The Formation of Binary Stars, ed. H. Zinnecker & R. Mathieu, 155

Brauer, F., Henning, T., & Dullemond, C. P. 2008, A&A, 487, L1

Brittain, S. D., Carr, J. S., Najita, J. R., Quanz, S. P., & Meyer, M. R. 2014, ApJ, 791, 136

Brittain, S. D., Najita, J. R., Carr, J. S., et al. 2013, ApJ, 767, 159

Brown, J. M., Blake, G. A., Dullemond, C. P., et al. 2007, ApJ, 664, L107

Brown, J. M., Blake, G. A., Qi, C., et al. 2009, ApJ, 704, 496

Cameron, A. G. W. 1962, Icarus, 1, 13

Canovas, H., Ménard, F., de Boer, J., et al. 2015, A&A, 582, L7

Carmona, A., Pinte, C., Thi, W. F., et al. 2014, A&A, 567, A51

Casassus, S., Perez M., S., Jordán, A., et al. 2012, ApJ, 754, L31

Chiang, E. & Murray-Clay, R. 2007, Nature Physics, 3, 604

Clampin, M., Krist, J. E., Ardila, D. R., et al. 2003, AJ, 126, 385

Claudi, R. U., Turatto, M., Gratton, R. G., et al. 2008, in Society of Photo-Optical Instrumentation Engineers (SPIE) Conference Series, Vol. 7014, Society of Photo-Optical Instrumentation Engineers (SPIE) Conference Series, 3

Crida, A., Morbidelli, A., & Masset, F. 2006, Icarus, 181, 587

Currie, T. 2010, ArXiv e-prints

Currie, T., Cloutier, R., Brittain, S., et al. 2015, ApJ, 814, L27

Currie, T., Muto, T., Kudo, T., et al. 2014, ApJ, 796, L30

Cutri, R. M., Skrutskie, M. F., van Dyk, S., et al. 2003

de Gregorio-Monsalvo, I., Ménard, F., Dent, W., et al. 2013, A&A, 557, A133

de Juan Ovelar, M., Min, M., Dominik, C., et al. 2013, A&A, 560, A111

Debes, J. H., Jang-Condell, H., Weinberger, A. J., Roberge, A., & Schneider, G. 2013, ApJ, 771, 45

Dent, W. R. F., Greaves, J. S., & Coulson, I. M. 2005, MNRAS, 359, 663

Dodson-Robinson, S. E. & Salyk, C. 2011, ApJ, 738, 131

Dohlen, K., Langlois, M., Saisse, M., et al. 2008, in Society of Photo-Optical Instrumentation Engineers (SPIE) Conference Series, Vol. 7014, Society of Photo-Optical Instrumentation Engineers (SPIE) Conference Series, 3

Dominik, C. & Dullemond, C. P. 2011, A&A, 531, A101

Dominik, C., Dullemond, C. P., Waters, L. B. F. M., & Walch, S. 2003, A&A, 398, 607

Dong, R., Hall, C., Rice, K., & Chiang, E. 2015a, ApJ, 812, L32

Dong, R., Rafikov, R., Zhu, Z., et al. 2012, ApJ, 750, 161

Dong, R., Zhu, Z., Rafikov, R. R., & Stone, J. M. 2015b, ApJ, 809, L5

Doucet, C., Pantin, E., Lagage, P. O., & Dullemond, C. P. 2006, A&A, 460, 117

Draine, B. T. 2003, ApJ, 598, 1017

Duchêne, G. 2010, ApJ, 709, L114

Dullemond, C. P. & Dominik, C. 2004, in Astronomical Society of the Pacific Conference Series, Vol. 321, Extrasolar Planets: Today and Tomorrow, ed. J. Beaulieu, A. Lecavelier Des Etangs, & C. Terquem, 361

Dullemond, C. P. & Dominik, C. 2005, A&A, 434, 971

Dullemond, C. P., Dominik, C., & Natta, A. 2001, ApJ, 560, 957

Dullemond, C. P. & Monnier, J. D. 2010, ARA&A, 48, 205

Dunkin, S. K., Barlow, M. J., & Ryan, S. G. 1997, MNRAS, 290, 165

Durisen, R. H., Boss, A. P., Mayer, L., et al. 2007, Protostars and Planets V, 607

Ellerbroek, L. E., Podio, L., Dougados, C., et al. 2014, A&A, 563, A87

Espaillat, C., Furlan, E., D'Alessio, P., et al. 2011, ApJ, 728, 49

Espaillat, C., Muzerolle, J., Najita, J., et al. 2014, Protostars and Planets VI, 497

Fedele, D., Bruderer, S., van den Ancker, M. E., & Pascucci, I. 2015, ApJ, 800, 23

Fedele, D., van den Ancker, M. E., Acke, B., et al. 2008, A&A, 491, 809

Finkenzeller, U. & Mundt, R. 1984, A&AS, 55, 109

Follette, K. B., Grady, C. A., Swearingen, J. R., et al. 2015, ApJ, 798, 132

Follette, K. B., Tamura, M., Hashimoto, J., et al. 2013, ApJ, 767, 10

Fukagawa, M., Tamura, M., Itoh, Y., Hayashi, S. S., & Oasa, Y. 2003, ApJ, 590, L49

Fukagawa, M., Tamura, M., Itoh, Y., et al. 2010, PASJ, 62, 347

Fusco, T., Petit, C., Rousset, G., et al. 2006, in Society of Photo-Optical Instrumentation Engineers (SPIE) Conference Series, Vol. 6272, Society of Photo-Optical Instrumentation Engineers (SPIE) Conference Series, 0

Garufi, A., Podio, L., Kamp, I., et al. 2014a, A&A, 567, A141

Garufi, A., Quanz, S. P., Avenhaus, H., et al. 2013, A&A, 560, A105

Garufi, A., Quanz, S. P., Schmid, H. M., et al. 2014b, A&A, 568, A40

Grady, C. A., Devine, D., Woodgate, B., et al. 2000, ApJ, 544, 895

Grady, C. A., Muto, T., Hashimoto, J., et al. 2013, ApJ, 762, 48

Grady, C. A., Polomski, E. F., Henning, T., et al. 2001, AJ, 122, 3396

Grady, C. A., Schneider, G., Hamaguchi, K., et al. 2007, ApJ, 665, 1391

Grady, C. A., Schneider, G., Sitko, M. L., et al. 2009, ApJ, 699, 1822

Grady, C. A., Woodgate, B., Heap, S. R., et al. 2005, ApJ, 620, 470

Guidi, G., Tazzari, M., Testi, L., et al. 2016, ArXiv e-prints

Hales, A. S., Gledhill, T. M., Barlow, M. J., & Lowe, K. T. E. 2006, MNRAS, 365, 1348

Hashimoto, J., Dong, R., Kudo, T., et al. 2012, ApJ, 758, L19

Hashimoto, J., Tamura, M., Muto, T., et al. 2011, ApJ, 729, L17

Helled, R., Bodenheimer, P., Podolak, M., et al. 2014, Protostars and Planets VI, 643

Henyey, L. G. & Greenstein, J. L. 1941, ApJ, 93, 70

Herbst, W. & Shevchenko, V. S. 1999, AJ, 118, 1043

Høg, E., Fabricius, C., Makarov, V. V., et al. 2000, A&A, 355, L27

Hog, E., Kuzmin, A., Bastian, U., et al. 1998, A&A, 335, L65

Hollenbach, D. 1994, NASA STI/Recon Technical Report N, 1

Inoue, A. K., Honda, M., Nakamoto, T., & Oka, A. 2008, PASJ, 60, 557

Isella, A., Testi, L., Natta, A., et al. 2007, A&A, 469, 213

Janson, M., Thalmann, C., Boccaletti, A., et al. 2016, ApJ, 816, L1

Juhász, A., Benisty, M., Pohl, A., et al. 2015, MNRAS, 451, 1147

Kamp, I., Woitke, P., Pinte, C., et al. 2011, A&A, 532, A85

Klahr, H. H. & Henning, T. 1997, Icarus, 128, 213

Kraus, A. L. & Ireland, M. J. 2012, ApJ, 745, 5

Kuiper, G. P. 1951, Proceedings of the National Academy of Science, 37, 383

Kusakabe, N., Grady, C. A., Sitko, M. L., et al. 2012, ApJ, 753, 153

Lafrenière, D., Marois, C., Doyon, R., Nadeau, D., & Artigau, É. 2007, ApJ, 660, 770

Lambrechts, M. & Johansen, A. 2012, A&A, 544, A32

Lenzen, R., Hartung, M., Brandner, W., et al. 2003, in Society of Photo-Optical Instrumentation Engineers (SPIE) Conference Series, Vol. 4841, Society of Photo-Optical Instrumentation Engineers (SPIE) Conference Series, ed. M. Iye & A. F. M. Moorwood, 944–952

Levenhagen, R. S. & Leister, N. V. 2006, MNRAS, 371, 252

Lissauer, J. J. & Stewart, G. R. 1993, in Astronomical Society of the Pacific Conference Series, Vol. 36, Planets Around Pulsars, ed. J. A. Phillips, S. E. Thorsett, & S. R. Kulkarni, 217–233

Liu, W. M., Hinz, P. M., Meyer, M. R., et al. 2003, ApJ, 598, L111

Lovelace, R. V. E., Li, H., Colgate, S. A., & Nelson, A. F. 1999, ApJ, 513, 805

Lyo, A.-R., Ohashi, N., Qi, C., Wilner, D. J., & Su, Y.-N. 2011, AJ, 142, 151

Maaskant, K. M., de Vries, B. L., Min, M., et al. 2015, A&A, 574, A140

Maaskant, K. M., Honda, M., Waters, L. B. F. M., et al. 2013, A&A, 555, A64

Maaskant, K. M., Min, M., Waters, L. B. F. M., & Tielens, A. G. G. M. 2014, A&A, 563, A78

Macintosh, B., Graham, J. R., Ingraham, P., et al. 2014, Proceedings of the National Academy of Science, 111, 12661

Madlener, D., Wolf, S., Dutrey, A., & Guilloteau, S. 2012, A&A, 543, A81

Maire, A.-L., Bonnefoy, M., Ginski, C., et al. 2015, ArXiv e-prints

Mannings, V. & Sargent, A. I. 1997, ApJ, 490, 792

Mariñas, N., Telesco, C. M., Fisher, R. S., & Packham, C. 2011, ApJ, 737, 57

Marino, S., Perez, S., & Casassus, S. 2015, ApJ, 798, L44

Marois, C., Lafrenière, D., Doyon, R., Macintosh, B., & Nadeau, D. 2006, ApJ, 641, 556

Marsh, K. A., Silverstone, M. D., Becklin, E. E., et al. 2002, ApJ, 573, 425

Mason, B. D., Wycoff, G. L., Hartkopf, W. I., Douglass, G. G., & Worley, C. E. 2001, AJ, 122, 3466

Masset, F. S. 2008, in EAS Publications Series, Vol. 29, EAS Publications Series, ed. M.-J. Goupil & J.-P. Zahn, 165–244

Mathews, G. S., Klaassen, P. D., Juhász, A., et al. 2013, A&A, 557, A132

Mawet, D., Pueyo, L., Lawson, P., et al. 2012, in Society of Photo-Optical Instrumentation Engineers (SPIE) Conference Series, Vol. 8442, Society of Photo-Optical Instrumentation Engineers (SPIE) Conference Series, 4

Mayama, S., Hashimoto, J., Muto, T., et al. 2012, ApJ, 760, L26

Meeus, G., Waters, L. B. F. M., Bouwman, J., et al. 2001, A&A, 365, 476

Meijer, J., Dominik, C., de Koter, A., et al. 2008, A&A, 492, 451

Mie, G. 1908, Ann Phys., 25, 37

Min, M. 2009, in Astronomical Society of the Pacific Conference Series, Vol. 414, Cosmic Dust - Near and Far, ed. T. Henning, E. Grün, & J. Steinacker, 356

Min, M. 2015, in European Physical Journal Web of Conferences, Vol. 102, European Physical Journal Web of Conferences, 00016

Min, M., Canovas, H., Mulders, G. D., & Keller, C. U. 2012, A&A, 537, A75

Min, M., Rab, C., Woitke, P., Dominik, C., & Ménard, F. 2016, A&A, 585, A13

Moerchen, M. M., Telesco, C. M., & Packham, C. 2010, ApJ, 723, 1418

Montesinos, M., Cuadra, J., Perez, S., Baruteau, C., & Casassus, S. 2015, ApJ, 806, 253

Mouillet, D., Lagrange, A. M., Augereau, J. C., & Ménard, F. 2001, A&A, 372, L61

Mulders, G. D., Min, M., Dominik, C., Debes, J. H., & Schneider, G. 2013a, A&A, 549, A112

Mulders, G. D., Paardekooper, S.-J., Panić, O., et al. 2013b, A&A, 557, A68

Müller, A., van den Ancker, M. E., Launhardt, R., et al. 2011, A&A, 530, A85

Murakawa, K. 2010, A&A, 518, A63

Muto, T., Grady, C. A., Hashimoto, J., et al. 2012, ApJ, 748, L22

Muzerolle, J., Calvet, N., Hartmann, L., & D'Alessio, P. 2003, ApJ, 597, L149

Natta, A., Testi, L., Calvet, N., et al. 2007, Protostars and Planets V, 767

Panić, O., Ratzka, T., Mulders, G. D., et al. 2014, A&A, 562, A101

Pantin, E., Waelkens, C., & Lagage, P. O. 2000, A&A, 361, L9

Pavlov, A., Feldt, M., & Henning, T. 2008, in Astronomical Society of the Pacific Conference Series, Vol. 394, Astronomical Data Analysis Software and Systems XVII, ed. R. W. Argyle, P. S. Bunclark, & J. R. Lewis, 581

Pérez, L. M., Isella, A., Carpenter, J. M., & Chandler, C. J. 2014, ApJ, 783, L13

Perrin, M. D., Schneider, G., Duchene, G., et al. 2009, ApJ, 707, L132

Pineda, J. E., Quanz, S. P., Meru, F., et al. 2014, ApJ, 788, L34

Pinilla, P., Benisty, M., & Birnstiel, T. 2012, A&A, 545, A81

Pinilla, P., Birnstiel, T., & Walsh, C. 2015, A&A, 580, A105

Pinte, C., Padgett, D. L., Ménard, F., et al. 2008, A&A, 489, 633

Pogodin, M. A., Hubrig, S., Yudin, R. V., et al. 2012, Astronomische Nachrichten, 333, 594

Pohl, A., Pinilla, P., Benisty, M., et al. 2015, MNRAS, 453, 1768

Pontoppidan, K. M., Blake, G. A., van Dishoeck, E. F., et al. 2008, ApJ, 684, 1323

Qi, C., D'Alessio, P., Öberg, K. I., et al. 2011, ApJ, 740, 84

Qi, C., Öberg, K. I., Andrews, S. M., et al. 2015, ApJ, 813, 128

Quanz, S. P. 2015, Ap&SS, 357, 148

Quanz, S. P., Amara, A., Meyer, M. R., et al. 2015, ApJ, 807, 64

Quanz, S. P., Amara, A., Meyer, M. R., et al. 2013a, ApJ, 766, L1

Quanz, S. P., Avenhaus, H., Buenzli, E., et al. 2013b, ApJ, 766, L2

Quanz, S. P., Birkmann, S. M., Apai, D., Wolf, S., & Henning, T. 2012, A&A, 538, A92

Quanz, S. P., Schmid, H. M., Geissler, K., et al. 2011, ApJ, 738, 23

Rapson, V. A., Kastner, J. H., Andrews, S. M., et al. 2015, ApJ, 803, L10

Raymond, S. N., Kokubo, E., Morbidelli, A., Morishima, R., & Walsh, K. J. 2014, Protostars and Planets VI, 595

Reggiani, M., Quanz, S. P., Meyer, M. R., et al. 2014, ApJ, 792, L23

Rice, W. K. M., Armitage, P. J., Wood, K., & Lodato, G. 2006, MNRAS, 373, 1619

Rice, W. K. M., Wood, K., Armitage, P. J., Whitney, B. A., & Bjorkman, J. E. 2003, MNRAS, 342, 79

Rosenfeld, K. A., Andrews, S. M., Hughes, A. M., Wilner, D. J., & Qi, C. 2013, ApJ, 774, 16

Rousset, G., Lacombe, F., Puget, P., et al. 2003, in Society of Photo-Optical Instrumentation Engineers (SPIE) Conference Series, Vol. 4839, Society of Photo-Optical Instrumentation Engineers (SPIE) Conference Series, ed. P. L. Wizinowich & D. Bonaccini, 140–149

Safronov, V. S. & Zvjagina, E. V. 1969, Icarus, 10, 109

Sallum, S., Follette, K. B., Eisner, J. A., et al. 2015, Nature, 527, 342

Shu, F. H., Adams, F. C., & Lizano, S. 1987, ARA&A, 25, 23

Sitko, M. L., Carpenter, W. J., Kimes, R. L., et al. 2008, ApJ, 678, 1070

Sitko, M. L., Day, A. N., Kimes, R. L., et al. 2012, ApJ, 745, 29

Strom, K. M., Strom, S. E., Edwards, S., Cabrit, S., & Skrutskie, M. F. 1989, AJ, 97, 1451

Sylvester, R. J. & Mannings, V. 2000, MNRAS, 313, 73

Sylvester, R. J. & Skinner, C. J. 1996, MNRAS, 283, 457

Takami, M., Karr, J. L., Hashimoto, J., et al. 2013, ApJ, 772, 145

Tanaka, H., Takeuchi, T., & Ward, W. R. 2002, ApJ, 565, 1257

Tanii, R., Itoh, Y., Kudo, T., et al. 2012, PASJ, 64, 124

Tatulli, E., Benisty, M., Ménard, F., et al. 2011, A&A, 531, A1

Testi, L., Birnstiel, T., Ricci, L., et al. 2014, Protostars and Planets VI, 339

Thalmann, C., Mulders, G. D., Janson, M., et al. 2015, ApJ, 808, L41

Thalmann, C., Schmid, H. M., Boccaletti, A., et al. 2008, in Society of Photo-Optical Instrumentation Engineers (SPIE) Conference Series, Vol. 7014, Society of Photo-Optical Instrumentation Engineers (SPIE) Conference Series, 3

Tinbergen, J. 2005, Astronomical Polarimetry

Tsukagoshi, T., Momose, M., Hashimoto, J., et al. 2014, ApJ, 783, 90

van Boekel, R., Dullemond, C. P., & Dominik, C. 2005, A&A, 441, 563

van den Ancker, M. E., de Winter, D., & Tjin A Djie, H. R. E. 1998, A&A, 330, 145

van den Ancker, M. E., The, P. S., Tjin A Djie, H. R. E., et al. 1997, A&A, 324, L33

van der Marel, N., van Dishoeck, E. F., Bruderer, S., Pérez, L., & Isella, A. 2015, A&A, 579, A106

van der Plas, G., van den Ancker, M. E., Fedele, D., et al. 2008, A&A, 485, 487

van Leeuwen, F., Feast, M. W., Whitelock, P. A., & Laney, C. D. 2007, MNRAS, 379, 723

Vicente, S., Merín, B., Hartung, M., et al. 2011, A&A, 533, A135

Vigan, A., Moutou, C., Langlois, M., et al. 2010, MNRAS, 407, 71

Wagner, K., Apai, D., Kasper, M., & Robberto, M. 2015, ApJ, 813, L2

Walsh, C., Juhász, A., Pinilla, P., et al. 2014, ApJ, 791, L6

Weidenschilling, S. J. 1977, MNRAS, 180, 57

Weidenschilling, S. J. 1980, Icarus, 44, 172

Weinberger, A. J., Becklin, E. E., Schneider, G., et al. 1999, ApJ, 525, L53

Weinberger, A. J., Rich, R. M., Becklin, E. E., Zuckerman, B., & Matthews, K. 2000, ApJ, 544, 937

Whipple, F. L. 1972, in From Plasma to Planet, ed. A. Elvius, 211

Whittet, D. C. B., Martin, P. G., Hough, J. H., et al. 1992, ApJ, 386, 562

Williams, J. P. & Cieza, L. A. 2011, ARA&A, 49, 67

Windmark, F., Birnstiel, T., Güttler, C., et al. 2012, A&A, 540, A73

Wisniewski, J. P., Clampin, M., Grady, C. A., et al. 2008, ApJ, 682, 548

Witzel, G., Eckart, A., Lenzen, R., & Straubmeier, C. 2010, The Messenger, 142, 5

Woitke, P., Min, M., Pinte, C., et al. 2015, ArXiv e-prints

Woitke, P., Pinte, C., Tilling, I., et al. 2010, MNRAS, 405, L26

Wright, C. M., Maddison, S. T., Wilner, D. J., et al. 2015, MNRAS, 453, 414

Zhu, Z., Nelson, R. P., Dong, R., Espaillat, C., & Hartmann, L. 2012, ApJ, 755, 6